

# **MICRO-SCALE COMPUTATIONAL ANALYSIS OF FUSED FILAMENT FABRICATED MATERIALS**

**EXPERIMENTALLY-VALIDATED FINITE ELEMENT ANALYSES OF  
REPRESENTATIVE VOLUME ELEMENTS**



# **MICRO-SCALE COMPUTATIONAL ANALYSIS OF FUSED FILAMENT FABRICATED MATERIALS**

**EXPERIMENTALLY-VALIDATED FINITE ELEMENT ANALYSES OF  
REPRESENTATIVE VOLUME ELEMENTS**

## **Master of Science Thesis**

For obtaining the degree of Master of Science in Materials Science & Engineering at  
Delft University of Technology

by

**Frederic CREUSEN**

Faculty of Mechanical, Maritime & Materials Engineering · Delft University of  
Technology.

The undersigned hereby certify that they have read and recommend to the Faculty of Mechanical, Maritime and Materials Engineering for acceptance a thesis entitled "**Micromechanical Analysis of Fused Filament Fabricated products, a Representative Volume Element approach**" by **Frederic Creusen** in partial fulfillment of the requirements for the degree of Master of Science.

Dated: 06-12-2019

Committee:

Dr. M.H.F. Sluiter, Technische Universiteit Delft

Dr. M.A. Bessa, Technische Universiteit Delft

Dr. V. Popovich, Technische Universiteit Delft

J. Berens MSc TNO

Cover:

Micrograph of the mesostructure of a Fused Filament Fabricated ABS sample combined with a contour plot of the von mises stress of the respective Representative Volume Element.



Copyright © 2019 by Frederic Creusen

An electronic version of this dissertation is available at  
<http://repository.tudelft.nl/>.

# ABSTRACT

This work aims at predicting the elasto-plastic and fracture behavior of ABS polymers obtained by Fused Filament Fabrication (FFF). The strategy adopted is to characterize the microstructure of Representative Volume Elements (RVEs) of the material, as well as the mechanical properties of the polymeric filament used in the FFF process and then conduct Finite Element Analyses (FEA) to predict the nonlinear behavior of the RVEs. The predictions are then experimentally validated. The research presented herein significantly contributes to the ambitious goal of establishing the process-structure-property relationships for polymeric parts fabricated by FFF, opening avenues to conduct data-driven analysis and design of additively manufactured products.

I shortened the abstract to be more straight to the point. Some of the info I removed can be moved to the Introduction if you want.

The FEA results are compared and validated with empirical tensile tests of FFF ABS products obtained using two different methods, the ISO 527 and the ASTM D3039 standard. The stress strain curves from the ASTM D3039 test procedure show significant overlap with the results from the optimized RVE analysis. The UTS of the 1 and 2 directions are predicted with a deviation of 5%. The difference in the 3 direction is explained through the sub-optimal healing between the subsequent layers. This accounts for roughly 10% of the drop in UTS in comparison with bulk ABS. This implies that porosity is the dominant phenomenon affecting the tensile behaviour of FFF parts.

This model has the potential to determine the mechanical properties of fully healed FFF products accurately with different layer orientations and line/width ratios. Subsequent work should consider the use of cohesive elements when sub-optimal healing between filament roads occurs.



# CONTENTS

<b>Abstract</b>	<b>v</b>
<b>1 Introduction</b>	<b>1</b>
<b>2 Literature review</b>	<b>3</b>
2.1 Fused Filament Fabrication . . . . .	3
2.1.1 History . . . . .	3
2.1.2 Process & hardware . . . . .	4
2.1.3 Process parameters . . . . .	11
2.2 Materials . . . . .	19
2.2.1 Materials for FFF . . . . .	20
2.2.2 ABS properties . . . . .	21
2.2.3 Elasticity . . . . .	25
2.2.4 Plasticity, damage and failure . . . . .	26
2.2.5 Application of ABS for FFF . . . . .	37
2.2.6 Standard parameters for ABS . . . . .	38
2.2.7 Standardization . . . . .	38
2.3 FFF properties . . . . .	40
2.3.1 Experimental mechanical characterization . . . . .	40
2.3.2 Mesostructure . . . . .	42
2.4 Composite theory . . . . .	44
2.4.1 Elastic modelling . . . . .	44
2.5 Summary . . . . .	48
<b>3 Hypothesis and research questions</b>	<b>51</b>
3.1 Knowledge gap in the current state of the art . . . . .	51
3.2 Hypothesis . . . . .	52
3.3 Research questions . . . . .	52
3.4 Research methodology . . . . .	53
<b>4 Digital reconstruction of mesostructure: creating the RVE geometry</b>	<b>55</b>
4.1 Methods and procedures . . . . .	55
4.1.1 Cross sectional Analysis . . . . .	56
4.1.2 Production strategy . . . . .	57
4.2 Microscopy . . . . .	58
4.3 Results . . . . .	58
4.3.1 Optical micrographs mesostructure regular analysis . . . . .	59
4.3.2 Optical micrographs mesostructure colored analysis . . . . .	60
4.3.3 Digital micrographs mesostructure colored analysis . . . . .	60
4.4 Discussion . . . . .	61

4.5 Conclusion . . . . .	65
<b>5 Experimental testing</b>	<b>67</b>
5.1 Methods and procedures . . . . .	67
5.1.1 ISO 527 . . . . .	68
5.1.2 ASTM D 3039 . . . . .	69
5.1.3 Ultimaker ABS Filament . . . . .	69
5.2 Results . . . . .	69
5.2.1 ISO 527 . . . . .	69
5.2.2 ASTM D 3039 . . . . .	71
5.2.3 Ultimaker ABS Filament . . . . .	73
5.3 Discussion . . . . .	74
5.4 Conclusion . . . . .	76
<b>6 Elastic modelling</b>	<b>77</b>
6.1 Methods and procedures . . . . .	77
6.1.1 RVE homogenization model . . . . .	77
6.1.2 Mesh . . . . .	78
6.1.3 Voigt model . . . . .	79
6.2 Results . . . . .	79
6.3 Discussion . . . . .	80
6.4 Conclusion . . . . .	81
<b>7 Non-linear modelling</b>	<b>83</b>
7.1 Methods and procedures . . . . .	83
7.1.1 Finite Element Method . . . . .	83
7.1.2 Convergence study . . . . .	86
7.1.3 Stress Intensity approach . . . . .	88
7.2 Results . . . . .	89
7.2.1 Convergence study mesh . . . . .	89
7.2.2 Convergence study RVE's . . . . .	89
7.2.3 Simulations compared with empirical results . . . . .	90
7.2.4 Simulations with altering aspect ratio . . . . .	90
7.2.5 Contour plots . . . . .	92
7.2.6 Comparison fracture stress . . . . .	93
7.2.7 Cracktip plasticity . . . . .	94
7.3 Discussion . . . . .	95
7.4 Conclusion . . . . .	97
<b>8 Conclusion and recommendations</b>	<b>99</b>
8.1 Conclusion . . . . .	99
8.1.1 Identification of process parameters influencing the mechanical properties (research question 1) . . . . .	99
8.1.2 Mesostructure (research question 2) . . . . .	100
8.1.3 Experimental testing (research question 3) . . . . .	100
8.1.4 Dominant phenomenon of the decrease in mechanical properties (research question 4) . . . . .	101

8.1.5 Constitutive modelling of thermoplastic amorphous polymers (research question 5) . . . . .	101
8.1.6 Additional theory for the prediction of mechanical behaviour of FFF parts (research question 6) . . . . .	102
8.2 Recommendations . . . . .	102
<b>References</b>	<b>103</b>



# 1

## INTRODUCTION

The Ministry of Defence (MoD) is trying to keep the equipment of its forces at full capability through intensive maintenance at home bases and in remote areas. The systems in use (vehicles, weapon systems, auxiliary systems etc.) can have different sets of complexity and date from different era's. At home bases, maintenance can rely on off-the-shelf parts when time-to-failure can be reasonably estimated, but predicting the lifetime of multiple components is challenging and creates a logistical issue. Additionally, these parts can be expensive due to their infrequent production or because the systems became outdated and production has stopped. The above described situation is even more crucial and complicated in foreign operation bases or on remote operating platforms such as ships. A rare part is difficult to come by in a remote area and can be extremely time consuming and expensive to obtain.

Additive manufacturing (3D printing or rapid manufacturing) can help reducing the above mentioned issues. Among the myriad of 3D printing processes currently available, polymer fused filament fabrication (FFF) dominates the market due to its simplicity and low cost [1]. Polymer based parts are a huge part of our current society, in consumer products as well as in engineering systems. The relevance of 3D printing polymer parts for Defence applications has been studied thoroughly [2–4], where the benefits for the MoD have been clarified: smaller logistic chains, possibility to produce cheaper alternatives with respect to conventional manufactures, fast innovation and iterations of products, production of complex geometries, in-house development of (classified) systems, the production of parts for obsolete systems due to unavailable producers, and finally the production of parts in remote areas.

multiple citations should be included in the same "cite" command, not separately.

references

check if this reference is adequate

These arguments are the inducements for the MoD to start exploring 3D printing. At the beginning of the 2010's different departments inside the MoD started to acquire simple systems to produce and experiment with early prototypes and non-critical parts. This lead to the acquisition of more complex FFF and additional machines to produce func-

tional parts. Despite these being of low quality and for non-critical parts, 3D printing seemed to fill in a need for small complex parts that normally took too long to order or to make. Also, due to the short lead time a large wave of iterations and innovations came from these small 3D printing groups. Currently, 3D printers are being implemented in different departments at home bases and abroad, first pilots at operation bases and on ships have been successful and are being implemented as permanent tools for fast production of non-critical parts. At this point, considering the success of the FFF implemented systems, the MoD wants to expand its knowledge and production capacity towards more critical parts. The logical choices being investing in metal additive manufacturing systems or optimizing the results of the FFF system. Despite that the FFF process has been optimized to a large degree, the results are still not comparable to conventional produced polymers. Often the mechanical properties of FFF printed polymer parts are as low as 50% of the properties obtained from injection moulded parts, for example. This significantly obstructs the MoD from implementing FFF products in functional appliances. The first step towards the wider use of FFF parts in the logistical chain would be to identify and predict its mechanical behaviour and quality.

To be able to produce and predict the properties of FFF printed polymers more knowledge needs to be acquired before the MoD can implement FFF for critical polymer parts. TNO (Nederlandse Organisatie voor Toegepast Natuurwetenschappelijk Onderzoek) is one of the advisers and research organizations that advises the MoD on related subjects. One of the key factors in increasing the mechanical properties of FFF printed parts is understanding the physical phenomena of the process and the materials science of the produced parts, which is the subject of this thesis. The goal of this thesis is to identify the mechanical behaviour, and to predict it through the modification of known models and simulation tools.

Please use the  
“ref” com-  
mand for  
referring to  
Chapters be-  
cause then  
the reader  
can click on  
the numbers  
and go there  
directly.

This dissertation follows the subsequent structure. In the first part, an extensive literature study of the FFF principles and the available research will be discussed. Based on the literature the knowledge gap is identified and the research questions are formulated. The second part of the thesis consists of four chapters, each of which include the methodologies, results, discussions and conclusions. Chapter 4 discusses the investigation on the mesostructure and the definition of a new Representative Volume Element. Chapter 5 presents the empirical testing of FFF products and the complications involved with it. Chapter 6 discusses the elastic properties of the Representative Volume Element, and applies a Finite Element Method homogenization approach to determine the elasticity in the 3 principle directions. Chapter 7 discusses the most important knowledge gap, the prediction of non-linear behaviour of FFF product through the Finite Element Method. In this chapter the effort and information of the previous chapters is combined to substantiate the effectiveness of the model and the results. Finally, a global conclusion and recommendation is presented in the last chapter.

# 2

## LITERATURE REVIEW

### 2.1. FUSED FILAMENT FABRICATION

To get a good understanding of the mechanical properties of Fused Filament Fabricated (FFF) produced parts, it is fundamental to have a good insight in the FFF process. Since this is a method that has been evolving quite extensively in the last decades, a quick review of the history and the applications are presented in the next sections.

#### 2.1.1. HISTORY

The FFF process has its fundamentals in polymer extrusion, which is a well known process well before the first 3D printer. Generally it is assumed that the first working robotic FFF 3D printer (as we know them) was developed in 1984 , since that moment it has been reference!

During the decade of 2010, 3D printing technology experienced an explosive growth. A wide variety of start-ups presented their systems to the market, and in some cases they have been acquired by established companies [5]. With these innovations also the process and products of 3D printers have been significantly optimized. From producing mostly fixtures, jigs, consumer, aesthetic and prototyping products, FFF parts are increasingly implemented as functional parts, e.g. machinery and vehicles . However, the reference! mechanical properties are still a fraction of the conventional made counterparts and are unpredictable. To overcome this problem more research is being done in the process and properties of FFF products. Also new solutions such as reinforced polymers are being presented to create better functional parts.

### 2.1.2. PROCESS & HARDWARE

"through", not  
trough; this  
typo appears  
a lot

The basics of FFF have been similar since the start of the technology. A polymer filament of a few millimeters (typically between 1.75 and 2.85mm) is pushed through a metal heating element before being deposited by a nozzle (a diameter of 0.4mm is most common, larger and smaller nozzles are also available). One resulting line is defined as a "road". The nozzle and heating element assembly is also referred as the "hot end", depicted as "liquifier" in figure 2.3. For simplification the "extruder" is defined as the whole assembly of the mechanism for extruding filament, shown in figure 2.3. This hot end is attached to a moving mechanism that can have different principles of motion, most of the systems use stepper motors that are connected to the extruder through rubber belts. These systems use three stepper motors which control the extruder in three degrees of freedom  $x$ ,  $y$  and  $z$  in Cartesian coordinates. Alternatively, an axis of motion can be used to move the buildplate vertically or horizontally. Above mentioned systems are called "Cartesian printers". Another popular extruder positioning method is through 3 motors connected to worm wheels in vertical moving direction, with an arm connected to the extruder allowing it to also have three degrees of freedom, these systems are called "Delta-style printers".

Reference for  
Figure 2.1

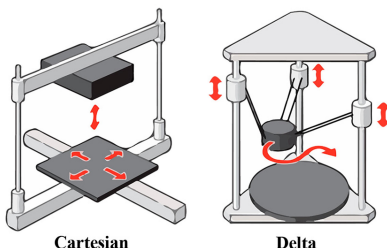


Figure 2.1: Comparison cartesian and delta system [scielo]

In this thesis, the focus will be on cartesian style printers, the specific system that will be used for investigation is the Ultimaker S5 system [6] shown in figure 2.2. The extruder is positioned according to machine code (named g-code) instructions above the so called "printbed", "builplate" or "buildplatform" and deposits molten filament in a particular path along the  $x$ - $y$  plane. After finishing the programmed path of a supposed "layer" the extruder moves up in the  $z$  direction to start depositing a new layer on top of the previous one. The part can be removed with little to no effort from the buildplate. The buildplate has often an implemented heating element to prevent large temperature gradients in the first layers, which can result in so called warping (due to difference in shrinkage in layers the corners of the part can start to curl, resulting in delamination from the buildplate), this is often an issue with materials with high thermal expansion coefficients and high glass transition temperature [7].



Figure 2.2: Ultimaker S5 [6]

Turner et al.[7] have extensively discussed the process and the effect it has on the product. The relevant concepts are summarized herein. Note that this system is typical for consumer based FFF systems and is (generally) the basis for more advanced systems. It might happen that particular systems use different processes, for this thesis the process of the Ultimaker S5 is assumed.

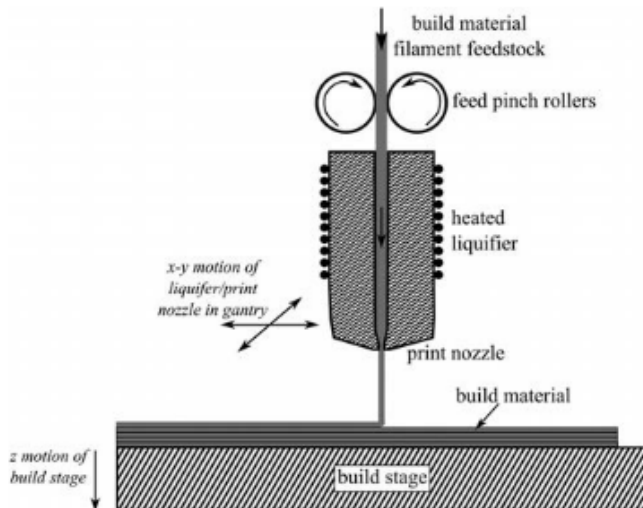


Figure 2.3: Wire feed mechanism [7].

#### FEED MECHANISM

The feed mechanism is the root of the material supply, between two feed pitch rollers a filament of material is being pushed through a nozzle as can be seen in figure 2.3. The

filament can be stored in a sealed container to prevent water absorption. Some materials are more prone to hygroscopy (like Nylon 66 and PLA), which during the extrusion results in the evaporation of the water and consequently in morphological changes in the material, blockages of the nozzle and formation of bubbles and porosity. This can be one of the issues of decreased mechanical properties, and should therefore be avoided.

## LIQUIFIER

The liquifier (figure 2.3) has a critical function: the softening of the polymer feed stock. This metal block has integrated heating elements to maintain a uniform temperature for liquefying the material. A range of amorphous and semi-crystalline thermoplastic polymers (including fibers) with different melting and glass transition temperatures can be used in filament form as feedstock material. The liquifier temperature does normally not exceed 280°C for consumer based systems, which excludes engineering polymers from use. It should be noted that due to the pressure and the shear force involved in the extrusion of filament through the nozzle, the polymer chains are being aligned in the direction of deposition (figure 2.4, which can have a significant impact on the mechanical properties of the part [8].

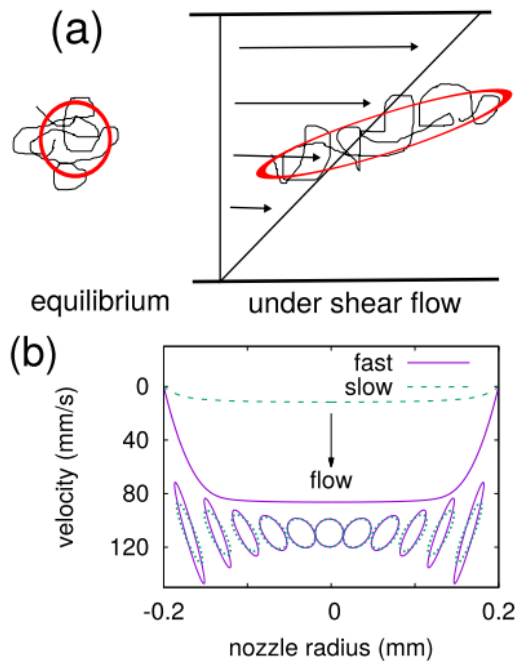


Figure 2.4: a) Alignment of polymer chains, and b) velocity profile of polymer chains exiting the nozzle [8].

### ROAD DEPOSITION

The nozzle pushes hot filament onto the buildplate. During the extrusion the polymer melt is under stress, which reduces its volume due to deformation of energy being stored elastically. The nozzle hovers above the substrate at the prescribed layer height (often between 0.1 and 0.4mm), as can be seen in figure 2.5. Consequently, the polymer melt is pushed outside and expands due to the absence of pressure. This phenomenon is called "dye swelling" and can be seen in figure 2.6. Dye swelling plays a large role in the determination of the tolerance and surface roughness of a part. A ratio ( $s$ ) can be assigned to the swelling of the material with respect to the diameter of the die opening (nozzle). This value depends on the geometry of the nozzle, material properties (such as thermal expansion coefficient) and is generally in the range of 1.05 to 1.3. Shofner et al [7] have found that the implementation of inelastic particles, such as short carbon fibers, have a positive effect of reducing the dye swelling, resulting in smoother surfaces (which is confirmed in empirical test with onyx, a carbon fibre filled nylon polymer [9]).

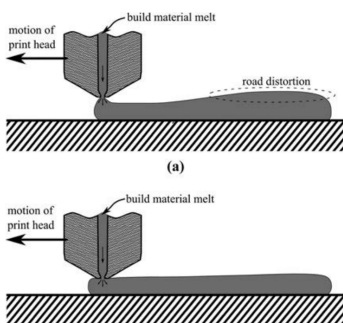


Figure 2.5: Road deposition [7]

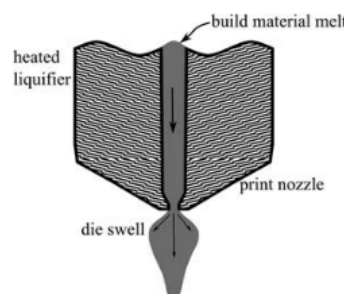


Figure 2.6: Die swelling [7]

The so called "bead" or "road" is deposited in an oblong shape (similar to a stadium shaped oval), and starts to cool due to convective cooling once it comes in contact with air and conductive cooling once it comes in contact with neighbouring roads. Bellini et al. [10] modeled this convective cooling assuming a heat transfer coefficient of  $h = 20W/m^2$ . In chapter 4 further investigation will be conducted on the shape of the road. Interestingly enough, the thermal conductivity of the feedstock material has a positive effect on the temperature of the bead after deposition. Instead of losing heat due to high thermal conduction, materials with high conductivity can more easily extract heat from the hot end at a larger distance, therefore creating better bonding between layers.

The touching surfaces of the roads are "welded" together if the temperature in both roads is high enough (figure 2.7). The deposited filament is practically uniformly melted, since the liquifier temperature is set at a higher temperature than the melting temperature ( $T_m$ ) or glass transition temperature for thermoplastics ( $T_g$ ). For perfect bonding the surface of the lower road should also reach this temperature and maintain this for enough time. However, the temperature of the lower road has cooled since it was de-

refer to Chapter 4 with "ref"; search for other references like this and do the same

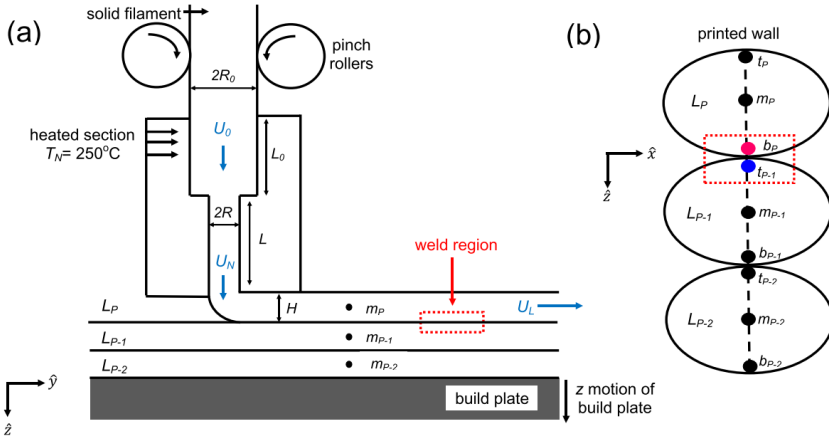


Figure 2.7: a) Welding of subsequent roads, and b) heated top layer contacts with cooled lower layer [11].

posited. The strength of the bond is therefore a function of time and temperature of both roads and can be expressed in two different mechanisms: wetting and healing (figure 2.9). This is an anisothermal process of heating and cooling different layers at high rates as can be seen in figure 2.8. One of the first researchers that began investigating this process where Thomas and Rodriguez [12] followed by Bellehumeur et al. [13] and Sun et al. [14]. Seppala et al. [15] did an extensive study on the temperature profile of extruded roads and the bond forming after different layers are being deposited on top of it. The temperature history can either empirically be observed with an infrared camera, or can numerically be approximated when the toolpath of the extruder is known. There are currently software tools available which will generate a predicted temperature profile for specific layers in a particular FFF produced geometry [16].

Wetting is defined by Wool [17] as close molecular contact (van der Waals bonds) when two pieces of molten polymers are brought into contact followed by inter diffusion of chain segments back and forth across the wetted interface. The diffusion of polymer chains is called healing, which is investigated by Sun et al [14]. After wetting of the roads, neck growth occurs which widens the area between adjunct roads. These three processes can be seen in figure 2.9.

After subsequent roads are deposited in layers on top of each other, a particular "mesostructure" of welded beads, with an elliptical shape, will appear. These mesostructures (shown in figure 2.10) are analyzed in different articles [14, 18–23], where all conclude that the mesostructure has significant impact on the mechanical properties. Most of the researchers used microtoming and optical microscopy to produce clear images (in the range of tenths of millimeters) of the mesostructure. These voids form a significant amount of porosity which has an adverse effect on the mechanical properties, resulting in stress concentrations and leading to premature brittle failure near the porous region. What is not

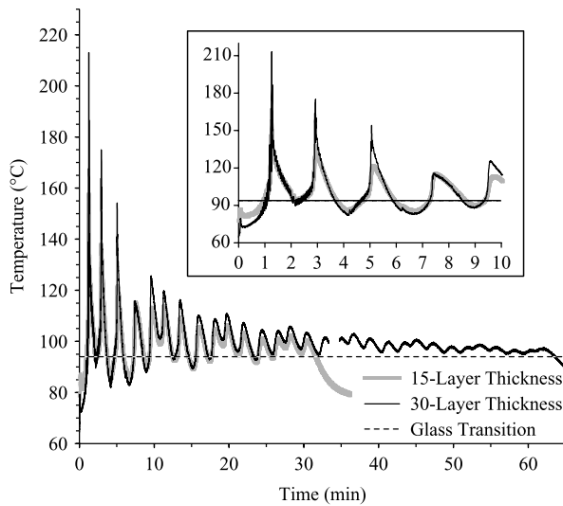


Figure 2.8: Temperature profile of the bottom filament [14]

observable in the mesostructure is the degree of healing between the roads. The majority of above mentioned researchers do not provide satisfactory information regarding their process settings or hardware used. Early experiments often incorporated Stratasys systems with their own produced ABS P400, due to their early market share.

The final shape of the road depends on the surface tension, feed rate, viscosity, rate of cooling and interaction with the print head. There have been attempts of modelling the shape and spreading of the roads without being successful. A model proposed in the work of Turner [7] assumes full wetting but does not account for the change of viscosity. The result significantly differs from empirical observations.

references

According to Sun, the amount of wetting and healing determines largely the mechanical properties of the part [14]. The healing of the polymer are related to the polymer material property called reptation time, which is the time a polymer needs, at a certain temperature, to "reptate" out of the other chains of the melt to acquire a new random position. Reptation is closely related to the glass transition temperature ( $T_g$ ), the temperature where polymers start to diffuse and lose viscosity. After reaching this temperature polymer chains start to reptate exponentially faster. Different authors [8] [24] [25] assume perfect bonding (full reptation) to be comparable to the mechanical properties of the middle of the road. With the help of WLF (Williams-Landel-Ferry graphs) a model can be made where reptation time is plotted as a function of temperature (figure 2.11). By producing a set of empirical data-points the WLF curve can be extrapolated [26]. With a higher temperature the amount of time needed for perfect healing is reduced, this can e.g. be achieved with a heated chamber or "envelope". According to Bartolai et al. [25] the strength of a road weld can be predicted using the following equation:

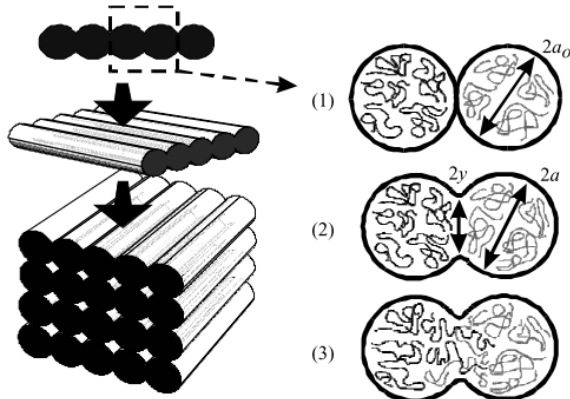


Figure 2.9: Bond formation between roads: (1) contact, (2) wetting and necking (3) healing [14]

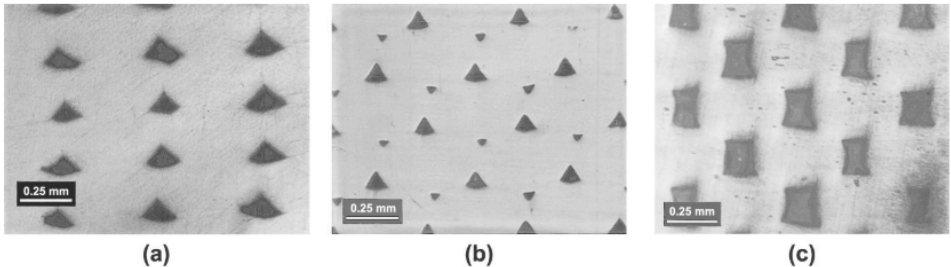


Figure 2.10: Different types of mesostructures [21]

$$\frac{\sigma_{weld}}{\sigma_{UTS}} = \left( \frac{t_{weld}}{t_{rep}} \right)^{1/4} \quad (2.1)$$

In this equation  $\sigma_{weld}$  is the weld strength in (MPa),  $\sigma_{UTS}$  is the bulk ultimate tensile strength (in MPa),  $t_{weld}$  is the time of molecular activity at a defined temperature (according to the WLF graph) at the interface (in seconds), and  $t_{rep}$  is the time average repetition time of the polymer (in seconds). As  $t_{weld}$  approaches  $t_{rep}$  the polymer becomes fully healed and best strength is achieved. In the (limited) validation and verification of Bartolai, the conclusion was the of  $\sigma_{weld}$  weld can be quite difficult for an accurate prediction.

#### BUILD PLATE AND CHAMBER

The liquefied filament is deposited on the build plate (also called printbed) and is consequently deposited on top of the previous layers. The buildplate can be as simple as a

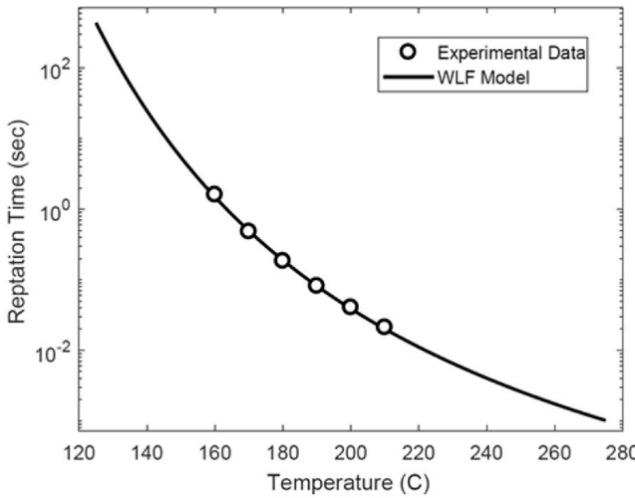


Figure 2.11: WLF model, reptation time is a function of temperature [15]

piece of metal or glass. However, there are some crucial aspects concerning the properties of the bed. The adhesion of the first deposited layer with the bed is very important to prevent delamination during the process. Therefore, heat elements are used to decrease steep heat gradients in the part, which result in warping. To prevent the bed itself from deforming (as little as a few hundredth of a mm can have negative impact on the first layer) a material with a low thermal expansion coefficient is chosen (e.g. glass). The bed temperature has a positive effect on the layer bonding in the lower region of the part. However, this is only "felt" in roughly the first centimeters of the part through conduction. It has been concluded that a higher overall temperature of the chamber has a beneficial impact on the road healing and subsequently on the mechanical properties [27]. More advanced systems therefore implement a heated envelope.

### 2.1.3. PROCESS PARAMETERS

Since the process parameters of the FFF process have major influence on the resulting parts, it is essential to analyze the parameters and identify their influence on the mechanical properties. In this section the important parameters are highlighted.

Most of these setting are defined by the so called "slicer" software, which is used to edit settings before generating a machine code that can be read by the printer. Certain machines have unique compatibility with a certain slicer (e.g. Eiger software from Markforged), or are produced by a manufacturer which also allows compatibility with other FFF systems (e.g. Cura from Ultimaker) or are produced by a third party software developer (e.g. Simplify 3D, Slic3r). These softwares have similar settings that can be adjusted which will result in a trade-off between speed and weight versus resolution, precision and mechanical performance. Since this thesis is mostly based on an Ultimaker S5 sys-

tem [6], and Cura is used as its slicer by the manufacturers, the terminology and parameters of Cura will be used as a benchmark.

The most significant parameters that have effect on the product are: - Layer height (mm)

- line width (mm)
- Feed rate ( $\text{mm}^3/\text{s}$ )
- Extrusion temperature ( $^{\circ}\text{C}$ )
- Envelope temperature ( $^{\circ}\text{C}$ )
- Build plate temperature ( $^{\circ}\text{C}$ )
- Travel speed (mm/s)
- Infill density (%)
- Infill orientation and shape ([a b c])
- (negative) Airgap (mm)

Regular slicers use different type of settings for different elements in a part. Let's consider the cross section of a cube (as can be seen in figure 2.12) for FFF printing. Once a CAD (computer aided design) file (often in the form of a STL "stereolithography" file) or other geometrical digital drawing supported by the slicer is uploaded, the slicer will define different settings for different elements. Most important being: Bottom layers, Outer shell (walls), top layers, infill. The effects of the elements will be outside the scope of this thesis and can be easily found online (3Dhubs [28], All3D [29], Ultimaker [6], Simplify 3D [30]). For this project the focus is on a part with only bottom-layers, mimicking fully "dense" parts. Applying only bottom layers will generate parts with best mechanical properties per volume [31].

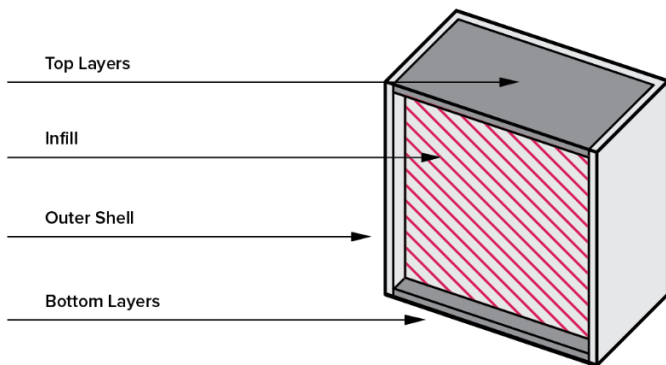


Figure 2.12: Elements of a 3D printed part [28]

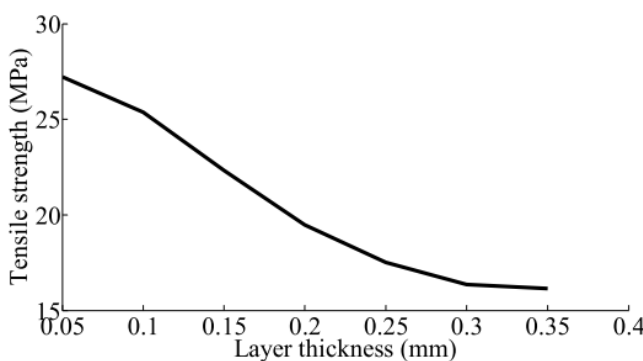
Effort that needs to be highlighted is the work of Li et al. [31] who generated empirical data and derived numerical models displaying the relation of temperature related parameters with the tensile strength of PLA, while maintaining other parameters constant.

According to parameters studied by Ahn et al. [32] the air gap and raster orientation are

the parameters most significantly affecting the mechanical properties. This is explained by the fact that the air gap is directly linked with the porosity and the raster orientation is directly linked with the stress applied at the road interfaces. A similar but more extensive research has been conducted by Mohamed et al. [33], resulting in the same conclusion.

### LAYER HEIGHT

The layer height is the height of one layer, subsequently also the height of one road. Increasing this parameter will decrease the print time proportionally, the drawback is higher surface roughness, larger porosity, larger stress concentration points and worse layer bonding. In Cura the layer height is limited between 0.04 and 0.32 mm. Since the polymer is welded by applying pressure and heat, different researchers assume that the roads have a horizontal and vertical overlap. This is about 10% according to Somireddy [18]. The empirical results of Li et al. [31] regarding the layer height parameter are shown in figure 2.13.



Clearer illustration of the XYZ system and the [45/-45]?

Figure 2.13: Layer height against tensile strength for XY[45/-45] samples [31]

Li [31] explains that a smaller layer height will actually increase bonding between roads. High conductivity combined with the small volume that needs to be heated will positively affect the temperature history of the interface, compared to thicker layer heights where the heat flux is not able to heat the material as much as for the thinner counterparts. This is also confirmed by Kuznetsov [34], who additionally claims that a reduced layer height also limits porosity in a part.

### LINE WIDTH

This process parameter can be misleading. According to Somireddy [18] FFF systems produce roads that are set to have a 10% overlap with its neighbouring roads in the xy

plane. The line width defines the distance between adjacent roads, which could be assumed as nominal line width or the distance between roads. According to him the extruded line width is therefore about 10% wider, if one would extrude a single road with a line width of 0.4 mm and a layer height of 0.2 mm it would be observed that a 10% larger ellipse is produced. This is in line with the observed increase in dimension for the production of fitted parts. A similar theory is proposed by Hodgson [35], "Extrusion Width is the thickness of a single filament extruded either in free air or above a surface. It's not the distance of two adjacent paths since some overlap will be generally applied in order to get better bonding." When printing only bottom layers the roads are constrained by the substrate on the bottom, by the nozzle on the top, and possibly by a road on one side. In figure 2.14 the sintering of roads can be observed. The problem with this model is the fact that the overlapped material is not accounted for. In chapter 4 a new model will be presented. There is currently not a consensus on the form of the mesostructure, this is partly due to large development and variety of printers and available printer settings.

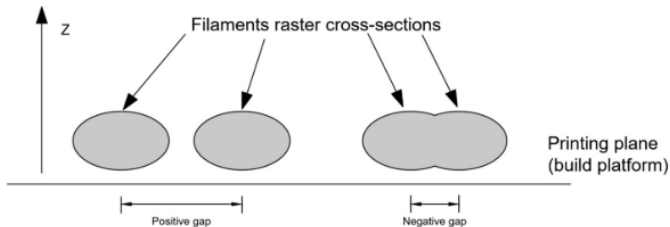


Figure 2.14: A schematic representation of filament cross-sectional areas, showing the difference between positive and negative gaps [36]

The range of the line width process parameter is limited by the nozzle diameter. For a nozzle of 0.4mm Cura allows for a line width ranging between 0.25 to 0.8. According to Montero [37] a variation in line width has no significant effect on the mechanical properties of the part. Thomas [12] and Kuznetsov [34] notice a positive effect in inter-road bonding with increased line width.

### AIRGAP

The airgap is defined as the gap in between different roads in the xy plane (intra-laminar) figure 2.14. Generating an airgap that is the same size of your road width will half your infill density, creating a negative airgap will produce an overlap between roads. It is not possible to select a negative value in Cura (implying an overlap of roads). This was possible in the Stratasys slicer settings, and has been thoroughly studied in different experiments [18, 21, 32, 38–40] and resulted in higher density and mechanical properties (increase of about 5-10% in  $E_{11}$ ,  $E_{22}$  and a 10% increase in  $G_{12}$ ) at the cost of speed and higher surface roughness and distortion. Additionally, the excess material can be accumulated on the nozzle and the part itself. Gebisa et al. [39] claim that a negative airgap has also a negative influence on the heat transfer since the roads are deposited very

plane perpendicular to the sheet?

close to each other and that more room facilitates the spread of semi-molten material between the gaps, resulting in structurally stronger parts. The conclusion of most experiments is that for ABS a negative airgap of not more than 10% can lead to improvements in mechanical properties without significant influence on the dimensional accuracy and surface quality. It appears that slicers have optimized this phenomena in the past years to achieve minimal porosity [35]. Simplify 3D has the option to enhance the infill extrusion width for only the infill (Cura can only modify it for the whole part). If we consider Somireddy's [18] mesostructure images for regular settings a 10% overlap is observed, if the line width is reduced with 10% while the extruded width remains equal, approximately 20% overlap is observed figure 2.15. The section 2.3.2 will address this subject in more detail. We can conclude from this analysis that negative airgap has an optimum where the mechanical properties are optimized without significantly distorting the surface of the product, it seems that this is already applied in some slicers.

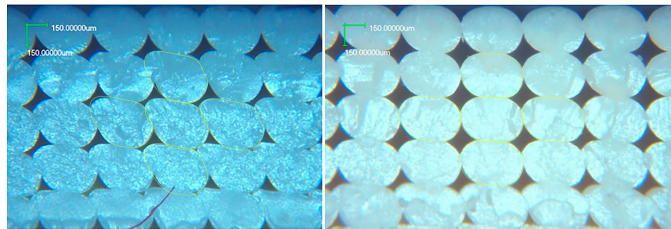


Figure 2.15: 20% overlap (left) 10% overlap (right)[18]

## FEED RATE

The feed rate is the volume of filament that is extruded per timescale. Since this is automatically calculated by Cura as a function of the layer height, line width and speed, it is difficult to precisely enhance, therefore it is defined as a multiplier of the default setting. Adjusting this will multiply the original calculated feed rate with a defined factor. This can for example fix under-extrusion (figure 2.17 when the feed rate is too low, resulting in bad bonding and large gaps) which is detrimental for the mechanical properties of the part. It can also compensate for over-extrusion 2.16, which is detrimental for tolerance and accuracy. However, this could also be used to increase the extrusion to generate the so called "negative air gap". By increasing the flow multiplier, a wider road can be deposited without an increase in distance between roads as would happen with increase line width. This could be a detour to achieve the same increase in mechanical properties as a negative air gap would have. We can conclude that the feed rate is closely related to the negative airgap parameter. The theory presented above and at the subsection of "line width" is supported by Patanwala et al. [41], who wrote a detailed report on the characterization of the flow rate and bonding of carbon nanotubes-PLA composites.

## 2

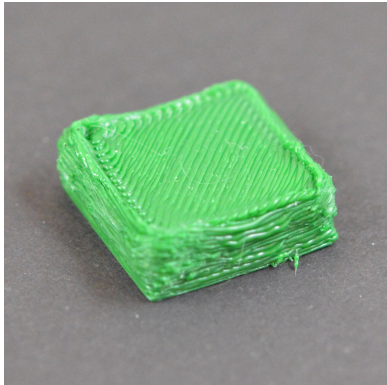


Figure 2.16: Overextrusion generating distortion of the part [30]



Figure 2.17: Underextrusion generating limited contact areas between roads [30]

#### EXTRUSION TEMPERATURE

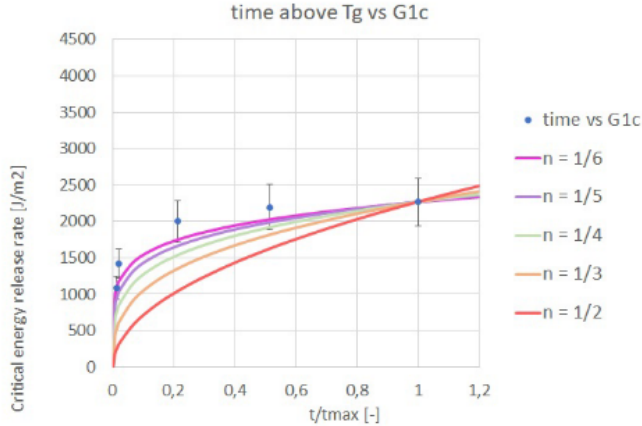
The extrusion temperature is defined as the constant temperature of the extruder. This setting is different for every material. To make a material flow more the temperature can be increased, this can help for very fast prints, or in the case of underextrusion. The dangers of printing too hot are, especially for small sections, a distortion of geometry due to a drop in viscosity. If the temperature is too low, the filament is too viscous to be extruded out of the nozzle, resulting in under extrusion or extrusion issues. There is an optimal range for the extrusion temperature which has been studied by Montero [37] and others.

#### ENVELOPE TEMPERATURE

Advanced FFF systems include a heated chamber or envelope. This is applied to increase the bonding of the roads, different studies [14] [13] have shown that the bonding properties (healing and wetting) are affected by temperature and time. The downside is the possibility of small segments being heated too much, which results in distortion. The optimal envelope temperature for semi-crystalline materials is between  $T_g$  and  $T_m$ . For amorphous polymers this is more problematic, since they do not have a specific melting temperature, instead they have a plateau after  $T_g$  as can be seen in figure 2.26, the first observation would be to not exceed the temperature of this plateau. According to van Veen [27] a clear relation was found between the envelope temperature and the bonding between layers, this is supported by the healing theory.

#### BUILD PLATE TEMPERATURE

The buildplate temperature is generally near the  $T_g$  to limit thermal stresses and warping. As a beneficial side effect, it constantly heats up a set of layers touching the build-plate. The quantitative effects of the build plate temperature on the mechanical properties of the part have not been studied yet.



2

Figure 2.18: Critical release energy rate vs. the time parts spend above  $T_g$  [27].

#### PRINT SPEED

Print speed proportionally alters the process times, but comes at a cost of larger inhomogeneity. Due to a large amount of accelerations the feed rate can differ through-out the part. Often over-extrusion is observed near the walls of a layer.

A low speed (approximately 35 mm/s) should be used to avoid large speed differences [31]. In figure 2.19 the dependency of the speed related to the position is shown.

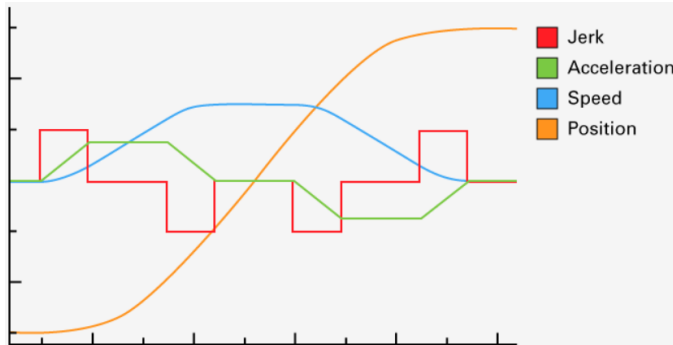


Figure 2.19: Speed graph of the toolhead while printing [42]

Li [31] also investigated the effect of the deposition velocity on the tensile strength as can be seen in figure 2.20. Print speed directly influences the feed rate, which is most likely the cause of a decrease in mechanical properties with an increasing speed. Li also explains that for slower speeds the bottom layers remain at a temperature higher than  $T_g$  for a longer period of time, which suggest that the adjacent filaments have more time to bond.

2

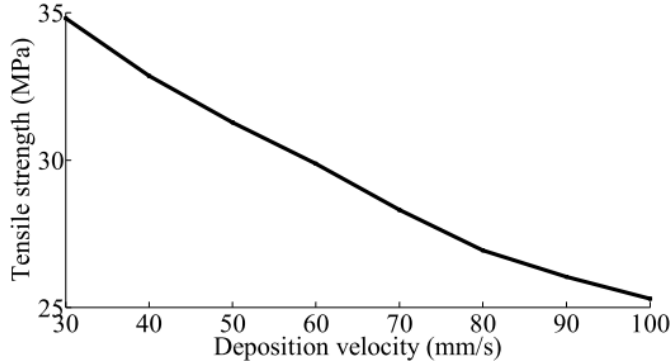


Figure 2.20: Deposition velocity against tensile strength for XY[45/-45] samples [31]

#### INFILL DENSITY

The infill percentage determines the percentage of material with respect to air used in the infill structure. The infill is generally enclosed by so called wall layers (also called perimeters) and top and bottom layers. These roads form a solid shell on the surface. This volume of the infill can have different geometries, ranging from simple rectangles, to intricate 3D patterns as can be seen in figure 2.21. The density can be changed in a variety of forms, creating thicker lines, more lines, direction etc. For this thesis the focus will be on structurally optimized parts, which includes 100% infill (which won't result in a related relative density since there is a high amount of porosity).

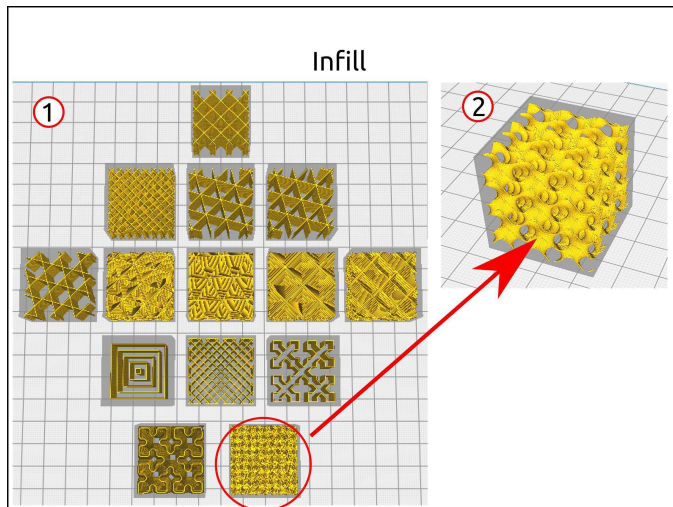


Figure 2.21: Different types of infill [42]

### ROAD ORIENTATION

If considering roads as fibres, one would notice that the structure starts to look like a composite laminate, where one layer of unidirectional roads can be considered as a lamina. Leveraging the extensive knowledge on conventional composite materials [43], the mechanical behavior of FFF products has been predicted by Rodriguez et al. [22] and compared to experimental results, as shown in figure 2.22. Section 2.4 provides a short overview on composite theory.

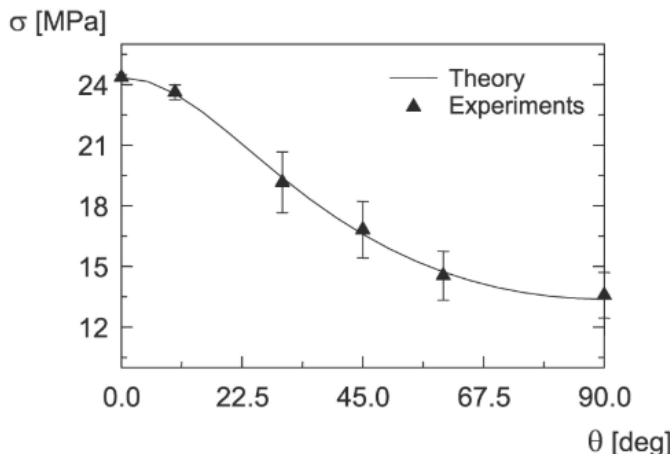


Figure 2.22: Orientations of roads with respect to load applied [22]

Intuitively, the part will have the best mechanical behaviour if it is loaded along the axis direction of the deposited roads. Stacking the layers in  $[45/ -45]_n$  configuration will result in quasi isotropic properties.

Additionally, not only the raster orientation, but the part orientation significantly influence the part properties. The printbed is in general oriented according to Cartesian coordinates,  $y$  being the longitudinal horizontal direction,  $x$  the transverse horizontal direction, and  $z$  the vertical direction (as can be seen in figure 2.23). When defining the angle of the roads, the slicers use the  $y$  direction as principle direction, meaning a  $[0]$  road will be directed along the  $y$  axis, while  $[90]$  will be directed along the  $x$  direction.

there were 2 "y", changed the second to "x". Confirm

## 2.2. MATERIALS

There is currently a wide range of polymer blends available for FFF, these can also include reinforced particles. The nature of the process, liquefying the polymer, only allows for thermoplastics. Thermosets have cross-links connecting the polymer chains, causing the material to degrade rather than to flow when heated. Parameters and properties such

I think this figure comes in too late. Even if you leave it here, you should refer to it much earlier in the document.

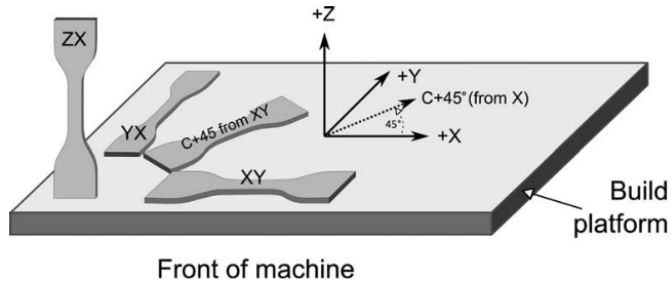


Figure 2.23: FFF coördinates for test specimen production

as crystallinity,  $T_m$ ,  $T_g$  and the thermal expansion coefficient make certain polymers more applicable for FFF. A deep comparison of different polymers and their properties will not be part of this thesis. A concise analysis and substantiation for the material that will be used in this thesis will be presented in this chapter.

### 2.2.1. MATERIALS FOR FFF

In figure 2.24 the different thermoplastic polymers can be seen. The  $y$ -axis represents the performance of the material, often related to the cost and ease of use. Be aware that the material properties of bulk or conventional produced polymer differ from the material properties found in the produced part.

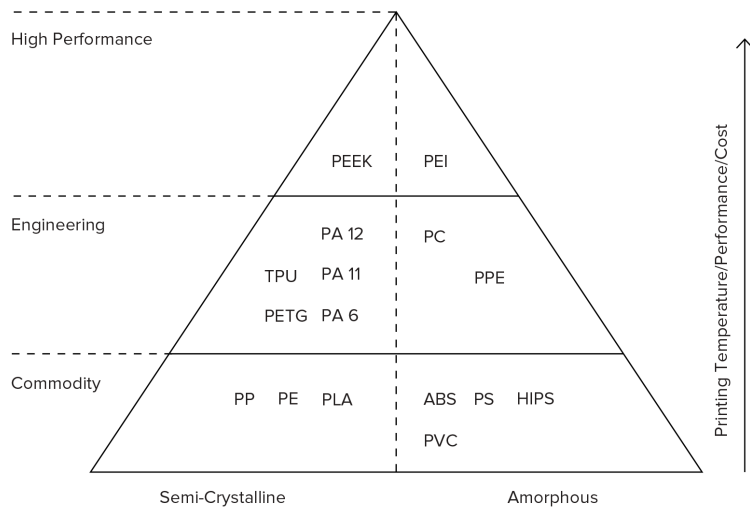


Figure 2.24: Polymer pyramid with FFF polymers [28]

To create a focus for this thesis, a particular material must be chosen to apply a scope on the research. To identify the mechanical properties of FFF produced parts, and the pa-

rameters affecting this, a polymer that has been used and researched extensively should be selected. This leads us to the lower tier of the pyramid, where PLA en ABS are by far the most implemented polymers. This is mostly due to the fact that FFF printers had only the possibility to print PLA and ABS until late 2012 [1], therefore it is not surprising that most systems are optimized for these materials. Since the academic research is limited on the topic of FFF (compared to e.g. injection moulding, which is a technology that has matured for decades), PLA and ABS are the best candidates.

PLA and ABS are most distinguishable by their polymer structure, PLA is semi-crystalline and ABS is amorphous. This difference is mostly noticeable in the thermal/viscous properties [44]. PLA has a clear melting temperature  $T_m$  (the moment where the semi-crystalline isotactic chains break its van der Waals forces), while ABS has only a glass transition temperature  $T_g$ , (where the polymer chains have enough thermal energy to start diffusing and consequently drop its Youngs modulus). This phenomenon is pictured in 2.26. The amount of crystallization can differ through a polymer based on the thermal history. High rates cooling can prevent chains from crystallizing, resulting in a smaller crystalline phase, this is typical for the FFF process. High degree of crystallinity is coupled with harder and thermally stable materials[45]. The amorphous regions provide elasticity and impact resistance. These properties are also reflected in the properties of PLA and ABS. The temperature history is dependant on the process parameters and geometry, resulting in an even larger fluctuation in mechanical properties when comparing different studies. This also means that it will be harder to generate constant samples and products with semi-crystalline polymers, as stated by Peterson [26]: "due to the high cooling rates (in the order of 10K/s) polymers experience: 1) trapping polymers in non-equilibrium conformations; 2) limited time for polymer diffusion at road interfaces; 3) complex (non-uniformly) crystallization profiles for semi-crystalline polymers". Crystallinity of polymers is extensively discussed in the books on polymer science by Vegt [46] and Halary [47].

The quoted sentence does not read well.

Despite that PLA is gaining popularity, due to its ease of use, low cost and biodegradability. However, ABS has been used more extensively in different production methods (e.g. injection moulding). Especially with the systems of Stratasys (which were optimized for ABS P400) a lot of research was conducted, as reviewed by Popescu et al. [49], Mohamed et al. [50] and Peterson [26].

Taking into account the physical issues with semi-crystalline polymers and the abundance of research presented on ABS, this thesis focuses on that material.

## 2.2.2. ABS PROPERTIES

### CHEMICAL COMPOSITION

As stated before, ABS<sup>1</sup> is an amorphous thermoplastic with a glass transition temperature of approximately 105°C [26]. Due to its amorphous nature it has no true melting point, therefore there is no sudden viscosity drop. It is a terpolymer (build from three

<sup>1</sup>Acrylonitrile Butadiene Styrene ( $C_8H_8$ ) $x$ ( $C_4H_6$ ) $y$ ( $C_3H_3N$ ) $z$

2

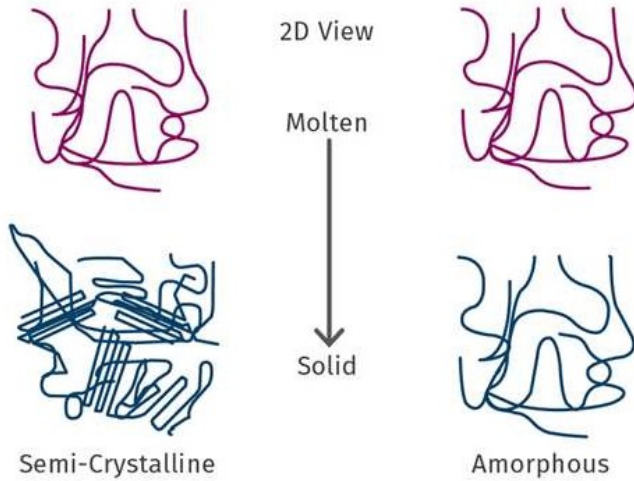


Figure 2.25: Molecule structure in molten and solid state [48].

monomers), and is created by polymerizing styrene and acrylonitrile in the presence of polybutadiene, figure 2.27.

The proportions of the different monomers vary for Acrylonitrile from 15-35%, which gives thermal and chemical resistance, butadiene from 5-30%, which gives toughness and performance over a broad temperature range and styrene 40-60%, which is cheap, eases process-ability, machine-ability and produces high gloss [51]. This results in a long chain of polybutadiene criss-crossed with shorter chains of poly(styrene-co-acrylonitrile). ABS has a general service temperature between -30 and 70 degrees, which means that the mechanical properties in use should not differ significantly in this range. An extensive study is presented by Peterson on the ABS blends and their properties for FFF

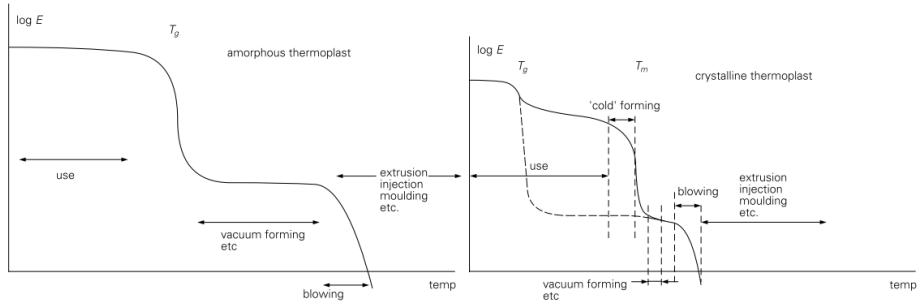
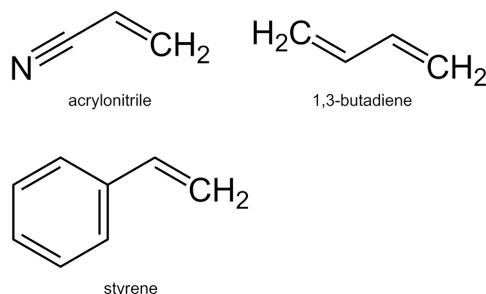


Figure 2.26: E modulus against temperature for amorphous and semi-crystalline polymers [46].



2

Figure 2.27: Monomers in ABS polymer

[26].

#### GENERAL PROPERTIES

ABS is often used due to its low cost, high impact resistance (also at low temperatures) and decent mechanical properties. It is also easy to color, is scratch and scuff resistant, and is easily processed and bonded [51]. According to CES edupack [51] general purpose extrusion ABS has low shrinkage and warpage. However, for FFF applications, ABS is difficult to use due to it's high warpage (in comparison to PLA). ABS has furthermore good resistance against chemicals and solvents and is a decent electrical insulator. The thermal process parameters (regardless of FFF) have effect on other properties of the ABS polymer, high temperature processes improve the gloss and heat resistance, while low temperatures increase impact resistance and strength. The limiting factors of ABS are its poor resistance to UV light and it's low operating temperature. The concentration of polybutadiene can increases the aging characteristics while other additives increase UV-protection. ABS is also suitable for additives such as glass and carbon fibers.

#### MOLECULAR STRUCTURE

Thermoplastic amorphous ABS looks on a molecular scale like a spaghetti of unchained polymers, as can be seen in figure 2.25. The polymers belonging to this class of materials are characterized by the temperature dependence of the Young modulus shown in figure 2.26. Each polymer chain adopts a coil conformation that strongly overlaps with its neighbors leading to chain entanglements. The entanglement density,  $\nu_e$ , is an important characteristic that affects the toughness of the polymer significantly, and is defined as the number of entanglements per unit volume of the material:

$$\nu_e = \frac{N_A \rho}{M_e} \quad (2.2)$$

where  $\rho$  is the polymer density,  $M_e$  the molecular weight of the chain between two entanglements,  $N_A$  the Avogadro number [47].

Amorphous polymers show a significant drop in stiffness after the glass transition temperature. According to Appelsved [52], this is the moment where the inter molecular bonds (van der Waals) break, after this moment the chains are able to diffuse through the polymer blend. For samples with a molecular weight higher than the molecular weight between entanglements,  $M_e$ , the Young modulus decreases through the glass transition and reaches a plateau value of about 1 MPa. This is called the rubbery plateau and its extent increases with molecular weight. At higher temperatures these high molecular weight polymers go through a fluidification zone before becoming highly viscous liquids. This is consequently the phase of material where the material is extruded. If  $M$  is smaller than  $M_e$ , the polymer skips the rubbery plateau, and almost immediately forms a viscous liquid. A relation between the temperature molecular weight and phase is shown in figure 2.28 [47].

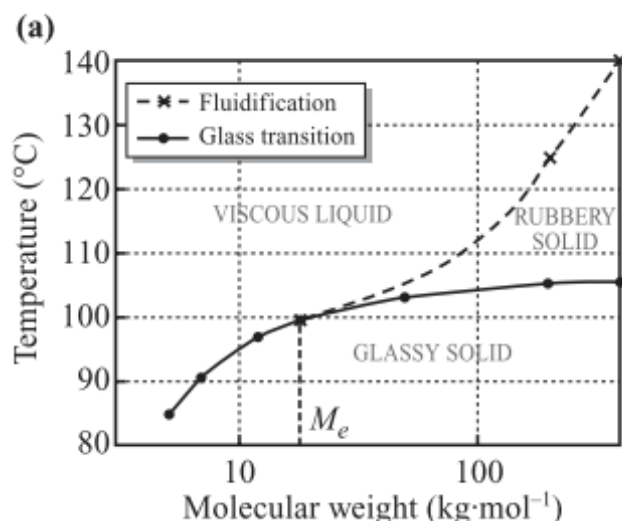


Figure 2.28: State diagram of un-cross-linked amorphous cis-1,4-polyisoprene [47]

Reptation is possible when  $M_e$  is smaller than  $M$ , and occurs after the glass transition temperature. The simplest form of the model assumes the polymer being "trapped" by entanglements, which is analogous to a chain trapped in a tube. The effective distance to free itself from the original entanglements is equivalent to the chain length. The speed at which the chain can reptate out of its entanglements is related to the temperature of the polymer blend[47]. Thermoplastics inhibit inherent viscoelasticity, also called creep, which describes the phenomenon of molecule diffusion under an applied load. This mechanism is quite difficult to predict, and will not have a focus in this thesis. Most important to notice is the significant effect of the strain rate on the mechanical response of thermoplastics, as is shown in figure 2.30 When extruding or processing thermoplastics, chains are being broken and reduced in length, this decrease in molecular weight leads to alteration of the response under different temperatures as is shown in 2.28.

### 2.2.3. ELASTICITY

Polymers exhibit an elastic response to a loading that is defined as instantaneous and reversible and may have either an energetic or an entropic physical origin. These constitutive mechanism are designated as true elasticity and hyper elasticity respectively. True elasticity, which for polymers only occurs at low strains, is linked to a poisson ratio that varies between 0.3 at low temperature and 0.5 at temperatures equal to or higher than the glass transition temperature. The entropic effect describes the increase in entropic energy (heat) of the polymer chain as a larger force due to the dynamic movement of the molecule. Random coils can be considered as a spring, multiple springs are connected to each other through entanglements. Thermosets, which contain crosslinks, have more predictable elastic behaviour than thermoplastics, which inhibit a large amount of viscoelasticity. However, these entanglements have similarities to cross links in the glassy state at a low strain, these entanglements will disappear as a result of sliding motion of the chain. Different models exists to predict the elastic behaviour of polymers, especially for thermosets, these are defined in detailed in the book of Halary [47]. If we consider the stress strain curve of a typical thermoplastic from figure 2.29, we observe a quasi-linear region up to the top of the curve where  $d\sigma/d\varepsilon = 0$ . This top is defined as the yield point for thermoplastics [53], which differs from the definition for e.g. metals. According to Appelsved [52] the true yield point of polymers is the stress at which van der Waals bonds are all broken, and chains can diffuse freely.

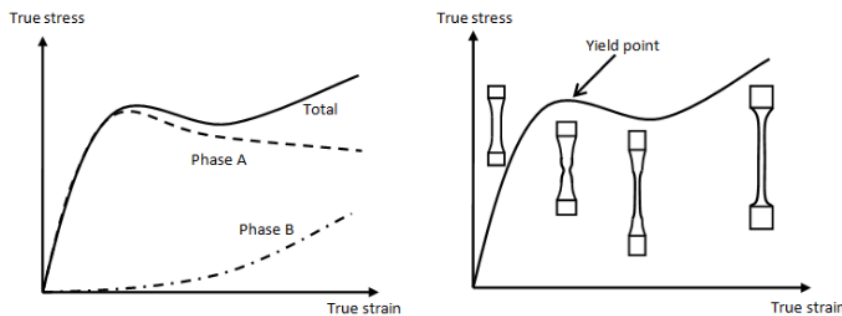


Figure 2.29: Typical stress-strain curves for thermoplastics [52]

Additionally, Appelsved differentiates two different phases (figure 2.29); phase A which dominates up to the stress maxima and deformation is mainly generated from movement of the molecular chains relatively to each other. Eventually the bonds break and the slope decreases. Since a polymer blend is a distribution of chains with different lengths, this is expected to occur over a strain range instead of a sudden drop. After the bonds are broken strain softening occurs. In phase B, the molecule chain itself is straightened, resulting in re-hardening at larger strains. The alignment at large strains cause transverse isotropy. The straightening of the molecular chains makes the material stronger, resulting in a different necking behaviour in contrast to metals.

2

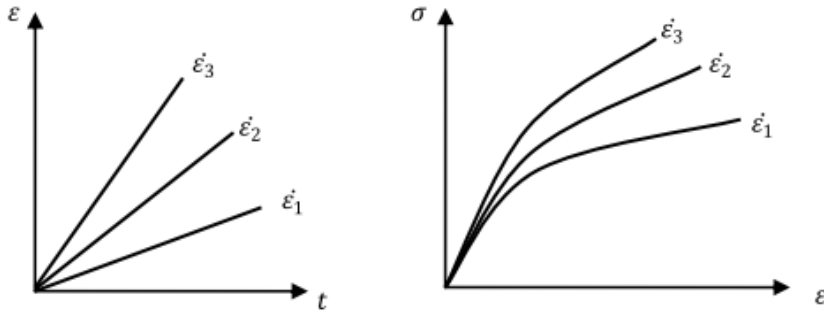


Figure 2.30: Effect of strain rate dependency on polymers [52]

#### 2.2.4. PLASTICITY, DAMAGE AND FAILURE

Due to the molecular structure of polymers, it is difficult to determine the start of plasticity. Loading/unloading experiments can be carried out to determine irreversible strains. The effect of loading and unloading is depicted in figure 2.31. The unloading is followed by recovery, until the residual strain have stabilized and can be concluded as permanent. Halary [47] claims that conducting compressive tests have the advantage of avoiding the

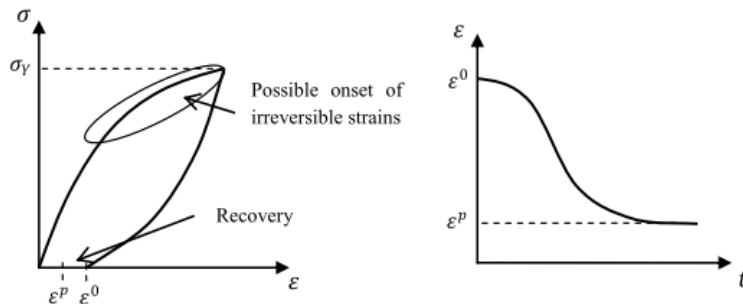


Figure 2.31: Loading/unloading behaviour with recovery [52]

effect of micro-voids always present in samples, since these voids increase sample brittleness on straining. In figure 2.32 empirically generated uniaxial compression stress strain curve of an amorphous thermoplastic polymer (PMMA) can be seen. The slope of the straight line corresponds to the material Young's modulus. Between A and B the stress-strain relation is no longer linear and the material exhibits anelastic behaviour. In figure 2.33 a schematic drawing of different loading regions is shown to support the explanation. In this region strain is still reversible. After the stress maximum at the yield point, a clear viscoplastic behaviour occurs. Additional strain is irreversible, and will lead to residual strain after unloading. It is worth pointing out that these residual strains can be removed by heating the polymer sample above its glass transition temperature. In general, it can be assumed that the Young's modulus remains relatively similar up to

the plastic range.

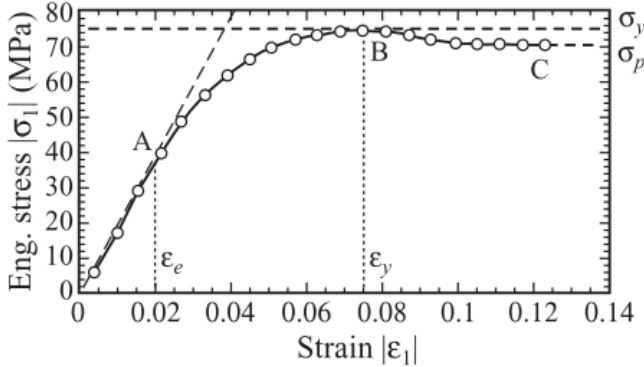


Figure 2.32: Compression stress-strain curve of a PMMA (A, elastic limit; B,yield point; C, plastic flow)[47]

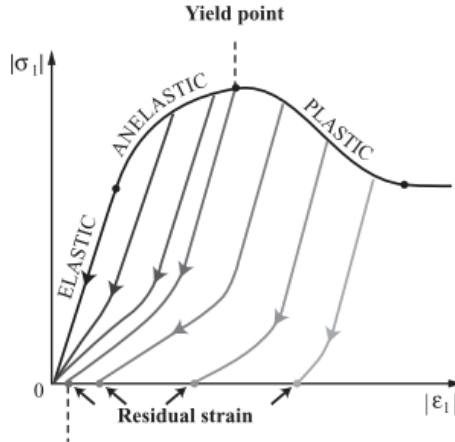


Figure 2.33: Schematic drawings of unloading profiles for a sample compressed at various strain values.)([47]

### YIELDING

Most common yield and failure criteria, like von Mises and Tresca [54], are dependent on the stress state of the material. This stress state is a function of the von Mises ( $\sigma_v$ ) or equivalent stress:

$$\sigma_v = \sqrt{\frac{(\sigma_{11} - \sigma_{22})^2 + (\sigma_{22} - \sigma_{33})^2 + (\sigma_{33} - \sigma_{11})^2 + 6(\sigma_{23}^2 + \sigma_{13}^2 + \sigma_{12}^2)}{2}} \quad (2.3)$$

However, these do not include dependency on the hydro-static stress, which is most common for metals. Yield and failure criterion for polymers are generally dependent on the the hydrostatic stress ( $\sigma_h$ ):

2

$$\sigma_h = P = \frac{\sigma_x + \sigma_y + \sigma_z}{3} \quad (2.4)$$

Additionally the yield and failure criterion are a function of the stress triaxiality ( $\sigma_t$ ):

$$\sigma_t = \frac{\sigma_h}{\sigma_v} \quad (2.5)$$

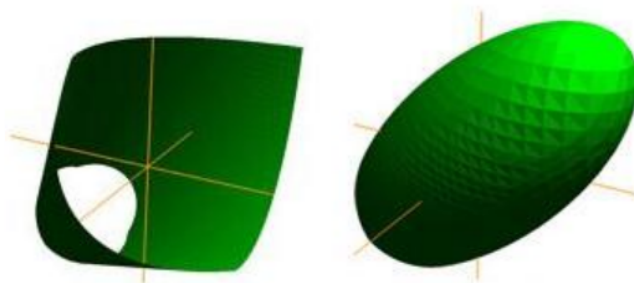


Figure 2.34: Common failure loci for metals defined by the von Mises criterion (left), and for ductile polymers (right), with the axis corresponding to the principle directions [54]

We have to be more precise.  
Is it yield or failure?  
Looks like you used Christensen's book, so it's probably failure. I think it makes more sense to start talking about yield first. Show the figures, and then talk about failure.

Figure 2.34 compares two common yield and failure loci for metals and polymers. The axis in this figure represent the principle stress directions. The left surface is defined by a stress state of the von Mises stress. If a pure hydrostatic pressure is applied, the surface will not be crossed. For polymers there is also a dependency on the hydrostatic pressure, since it will cross the surface at some point. It should me mentioned that the yield and failure surface for polymers is in reality not symmetric for tension and compression, as can be seen in figure 2.35. It has been concluded by several book on fracture mechanics [55] that polymers have a higher compressive yield strength than in tension. For ductile polymers also failure criteria are used based on the equivalent strain. This strain is calculated in a similar way as the equivalent stress. The failure surface might differ from the conventional von Mises or Tresca surfaces.

Assuming a isotropic polymer blend of ABS, we need to define a yield function based on the principal stress state of the material,  $f(\sigma_1, \sigma_2, \sigma_3)$  that is also dependent on the on the hydrostatic pressure. Claiming that a material has hydrostatic pressure sensitivity permits us to write the stress tensor as the sum of its deviatoric  $\sigma_d$ , and volumetric stress (the identity matrix multiplied with the hydrostatic stress  $\sigma_h$ ), as expressed in equation 2.6:

$$\begin{vmatrix} \sigma_1 & 0 & 0 \\ 0 & \sigma_2 & 0 \\ 0 & 0 & \sigma_3 \end{vmatrix} = \begin{vmatrix} \sigma_1 - P & 0 & 0 \\ 0 & \sigma_2 - P & 0 \\ 0 & 0 & \sigma_3 - P \end{vmatrix} + \begin{vmatrix} P & 0 & 0 \\ 0 & P & 0 \\ 0 & 0 & P \end{vmatrix} = \sigma_d + \sigma_h * I \quad (2.6)$$

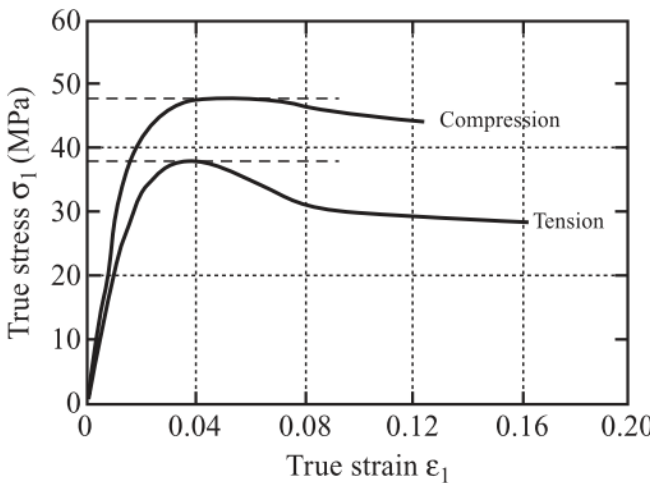


Figure 2.35: Comparison of stress-strain curves for PMMA for compression and tension [47]

where  $I$  is the identity matrix.

An enhanced form of the von Mises criterion can then be applied to polymers in the following way:

$$(\sigma_{11} - \sigma_{22})^2 + (\sigma_{22} - \sigma_{33})^2 + (\sigma_{33} - \sigma_{11})^2 = (2\sigma_y + \mu_{vM} * \sigma_h)^2 \quad (2.7)$$

after an equation, if you want to continue the text you have to use "noindent"

where  $\mu_{vM}$  is an internal friction coefficient.

The corresponding yield criterion is a cone whose axis is the hydrostatic pressure axis, and whose axis increases with hydrostatic pressure, similar to the yield locus for polymers in figure 2.34. A similar procedure can be applied to the Tresca criterion.

The Ree-Eyring model explains the yield behaviour on a molecular scale, according to this model, the sliding of molecules with respect to each other is achieved by passing through a transition state, called activated state, overcoming an energy barrier depending on both temperature and applied stress. This model assumes plastic deformation of amorphous polymers occurs as the displacement of chain segments from a site A to a site B once an activation state related to energy  $\Delta G$  is overcome, both located in a sliding plane resulting from the presence of a shear component. The principle of the model can be seen in figure 2.37. In the anelastic range the chains are merely "stretched" and will not be permanently displaced with respect to the other chains in the blend. In comparison with the theory presented by Apselveld, one could argue that the "activation energy" for permanent displacement is analogous to the breaking of the van der Waals bonds.

Rewrite previous sentence; not clear

I think you are using anelastic as "elastic", but I would prefer if you just write elastic or plastic. It's just simpler. Please update everywhere

2

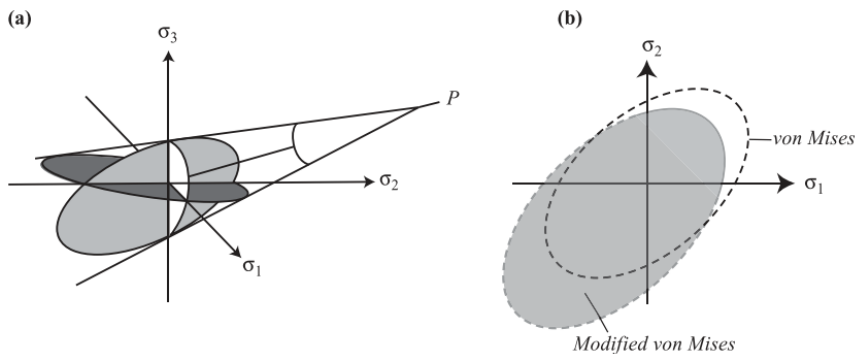


Figure 2.36: Yield surface for polymers a) three-dimensional b) two-dimensional compared with von Mises [47]

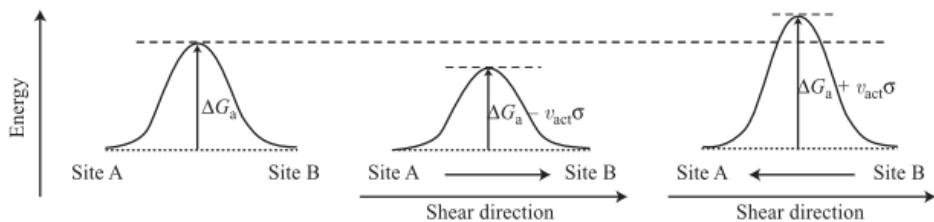


Figure 2.37: Energy diagram showing the principle of the Ree-Eyring model [47]

During tensile tests beyond the yield point many polymers, including amorphous polymers, undergo a plastic instability, the necking phenomenon. In this plastic region, chains have reached their extensibility limit, further neck propagation occurs through neighboring regions. After development of the whole neck, propagation with a uniform strain occurs again, until the sample breaks as can be seen in figure 2.38. In figure (a) stable necking is observed, while in figure (b) unstable necking leads to quick fracture. This behaviour depends on the considered polymer, possible defects, temperature and strain rate conditions.

There exist many other yield and failure criteria for thermoplastics, thermosets and composite materials. Lin [56] confirms the lack of accurate yielding and failure criteria for thermoplastics. Additionally, the PhD thesis of Melick [57] on the deformation and fracture of polymer glasses also mention the lack of failure criterion, and does not produce a satisfying solution for this issue. Different models (brittle or ductile) are implemented in commercial software such as the equivalent strain criterion, von Mises, Johnson-Cook, Hill and Drucker-Prager. The main drawback in these fracture models is that accurate predictions of failure can only be achieved for limited stress state and strain rate, which cannot be applied for thermoplastics. One of the currently popular material models for polymer plasticity in LS-DYNA is SAMP-1 (semi analytical model for polymers).

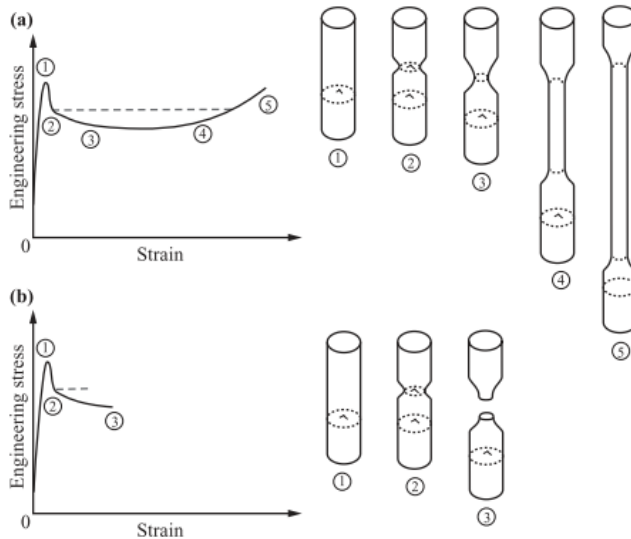


Figure 2.38: Schematic drawing of the necking phenomenon [47]

Melro [58] proposes a paraboloidal yield criterion for epoxies defined by Tschoegl, which can be defined as:

$$\Phi = 6J_2 + 2I_1(\sigma_c - \sigma_t) - 2\sigma_c\sigma_t \quad (2.8)$$

where  $J_2$  is the second invariant of the deviatoric stress tensor, and  $I_1 = \text{tr}(\sigma)$ . This is a variation of the general yield criterion shown in equation 2.7.

Du Bois [59] implemented a semianalytical model for the simulation of polymers (SAMP-1) in LS-DYNA under MAT187.

$$f = \sigma_v^2 - A_0 - A_1 * \sigma_h - A_2 * p^2 < 0 \quad (2.9)$$

For further details the reader is referred to the mentioned article.

Another popular yield criterion that is used by the SAMP-1 material model in LS-DYNA is the Drucker-Prager yield criterion.

#### DAMAGE AND FAILURE

Damage and fracture are important to investigate to identify the failure mechanism of the polymer, both concepts cannot be dealt with separately, since fracture, which results in the sample breakdown, usually comes after damage. Depending on the deformation conditions (stress field, temperature, strain rate) and characteristics of the polymer chains (chemical structure, molecular weight), two types of deformations may occur: shear bands and crazes.

Shear bands are deformations in shear direction (45 degrees for uniaxial compression tension). Important to note is that they do not create any voids inside the material, and therefore will not induce volume change. Shear band growth is controlled by plastic sliding only, therefore, stress associated with shear band formation is assumed to be equal to the yield stress.

Crazes are small microvoids containing fibrils bridging the two craze faces. Such fibrils play a major role in the ability of the craze to sustain loading in the direction perpendicular to its faces. These microvoids are ellipsoidal heterogeneities with a size ranging from  $10 \mu\text{m}$  to  $10 \text{ mm}$  along the major axis and from  $1$  to  $10 \mu\text{m}$  along the minor axis. In figure 2.39 a schematic of crazes is shown. The ratio between crazes and fibrils are approximately equal.

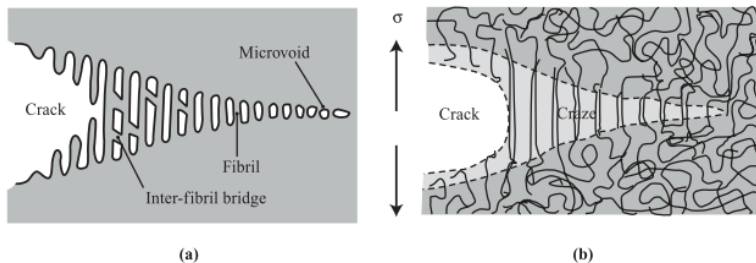


Figure 2.39: Schematic drawing of a craze a) Microvoids b) conformations of chains within a craze [47]

A crack systematically initiates from a sample “defect”. Despite a crack being inherently different from a craze, a craze initiates from microvoids. These defects lead to stress concentrations allowing the craze to grow, but only at temperatures under the glass transition temperature. These stress concentrations can be predicted by conventional fracture mechanics, but are outside the scope of this thesis. Fibrils in the crazes may either break, which requires to break high energy covalent bonds, or when undergoing higher mobility, may slide with respect to each other. The first results when high strain rate is applied at low temperature, and the latter occurs at a temperature near  $T_g$ . These mechanisms occur under tension at a stress lower than yield stress, and grow perpendicularly to the direction of the highest principle stress.

A craze criterion is proposed based on two arguments:

- Crazes are formed when strain reaches a critical value,  $\epsilon_c$ , along one direction.
- The strain craze value, which varies with temperature and strain rate, depends on the hydrostatic component of the stress tensor according to:

$$\epsilon_c = Y + \frac{X}{\sigma_1 + \sigma_2 + \sigma_3} \quad (2.10)$$

where X and Y are experimental parameters. From this criterion an envelope can be made to compare it with the von Mises yield criterion as can be seen in figure 2.40.

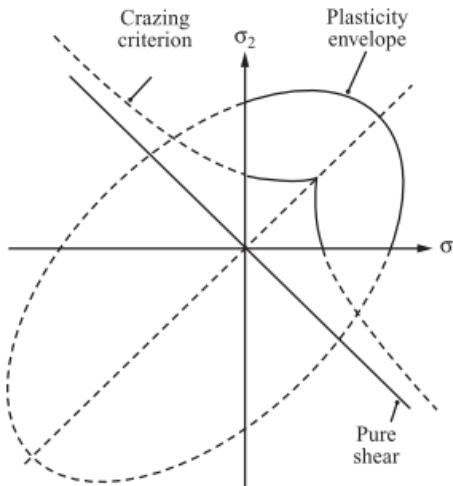


Figure 2.40: Plasticity envelope and craze criterion for PMMA [47]

The craze strain criterion can occur before yielding and plasticity, whereas shear bands only occur beyond the plasticity threshold. This result implies that any combination of two tensile stresses generates crazes instead of shear bands. A combination of a tensile and compressive stress might lead to both. Pure compression always generates shear bands.

To discriminate between shear bands and crazes, one could perform optical microscopy. Extensive research was conducted on this topic, the general conclusions are that the type of damage (crazing or shear bands) are dependent on the polymer, stress state, and temperature. In amorphous thermoplastics, both can be identified by a whitening phenomenon due to the scattering of light through polymer alignment. This effect is more intense for crazing, as a result of the higher density, and is more localized for shear banding. Additionally interactions may exist between these two types of damage. Initiation of shear deformation zones at the craze tip can occur when the craze propagation rate and widening are small.

Halary et al. concluded that despite the issues with microvoids, the uniaxial tensile test and uniaxial compressive tensile have, generally, identical shape and domains. Fracture occurs in the viscoplastic domain, and is usually ductile fracture with a specific angle of about 45 degrees between the fracture line and stretching direction. At lower temperatures, fracture generally takes place in the anelastic domain, there might be overlap with theory concerning brittle fracture of metals at low temperatures.

For tension too? That sounds very odd  
elastic?

In FEM modelling software different damage and failure models are implemented. The damage initiation point defines the start of degradation of stiffness, it only leads to effective damage if damage evolution is specified [60]. In case of ductile damage, the damage variable  $D$  is a function of plastic straining and affects the yield stress rather than the elastic modulus. This is equivalent to plastic softening. The material point is assumed

to fail when the overall damage variable  $D$  reaches a critical value  $D_{max}$ . A general form of the strain based fracture loci for thermoplastics can be written as follows

$$\bar{\epsilon}_f = f(\eta) = f\left(\frac{\sigma_h}{\sigma_v}\right) \quad (2.11)$$

## 2

where  $\bar{\epsilon}_f$  is the equivalent strain at failure. One of the most popular fracture and damage models for polymers is the Johnson Cook model, widely implemented in ABAQUS and LS-DYNA software:

$$\bar{\epsilon}_f = (D_1 + D_2 * \exp(D_3 * \frac{\sigma_h}{\sigma_v})) * (1 + D_4 * \frac{\dot{\epsilon}}{\dot{\epsilon}}) \quad (2.12)$$

where  $D_i$  are material parameters [61] that can be defined by the Hancock-McKenzie approach defines the following parameters:  $D_1 = 0, D_2 = 3/2, D_3 = \epsilon_{1f} * \exp(-1/2)$ . There are different variants of the Johnson Cook criterion, as proposed for example by Gao [62]:

$$\bar{\epsilon}_f = 1.65\epsilon_{1f}(-\frac{3}{2} * \frac{\sigma_h}{\sigma_v}) \quad (2.13)$$

where  $\epsilon_{1f}$  is the critical strain for ductile materials at which cracks are initiated under tension in one direction.

Different strain based failure criteria are proposed in LS-DYNA and Abaqus. Most implement a simple plastic strain at failure ( $\epsilon_p < \epsilon_{pf}$ ) or a major strain failure ( $\epsilon_1 < \epsilon_{1f}$ ), and others use the Johnson-Cook criterion as is described.

Damage in combination with the Johnson Cook model is defined in material model SAMP-1 in LS-DYNA as:

$$D = \epsilon_p / \epsilon_f \Rightarrow D < D_c \Rightarrow \epsilon_p < \epsilon_{pf} = D_c * \epsilon_f \quad (2.14)$$

The influence of stress triaxiality in a strain based failure criterion is important because different states of stress would result in a different equivalent strain at failure[61].

A damage variable, denoted as  $D$ , quantifies the part of the material cross section that no longer transmits forces (cracks or voids). In the following, only isotropic damage is considered. Elastic damage affects material stiffness, ductile damage affects material strength or both material strength and stiffness. This depends on the chosen formulation where two different approaches may be postulated: strain equivalence or energy equivalence. We will be discussing strain equivalence in this section.

Damage in polymers is relatively hard to model, since different mechanisms play a large role in the determination of damage. A study on the damage behaviour of polymers [63], Gu et al. presents different damage functions based on literature and proposes damage functions based on experimental data. The general stiffness damage as function of plastic strain is defined as:

What about  
 $D_4$ ?

reference

$$E_{eff} = E_0 * (1 - D) \quad (2.15)$$

where Nutini and Vitali proposed a simple definition of the damage parameter calculated from the volume strain, since an important characteristic of thermoplastics is the generation of damage (voids and crazes) during plastic volumetric deformation  $\epsilon_v$ , which is defined as the sum of the principle strains.

$$D = 1 - \exp(-\epsilon_v) \quad (2.16)$$

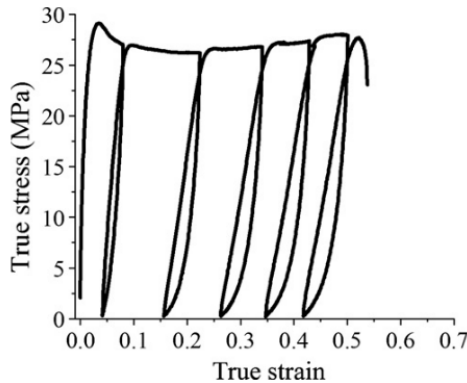


Figure 2.41: Sample of trues stress-strain curve of polypropylene[63]

In figure 2.41 the results from a loading/unloading experiment was carried out on a polypropylene sample to get more insight on the damage behaviour. As can be seen, the Young's modulus slightly decreases with plastic strain. However, after the first cycle (just after the softening region) the change in stiffness seems minimal. Unfortunately, no absolute values of the Young's moduli are presented in this study.

Following the results of the above experiment, this study proposed a damage function according to equation 2.16 that can be fitted to the experimental results. Since the damage only occurs in the plastic region for polymers, the result is a function of plastic strain ( $\epsilon_p$ ), and is fitted with a double term exponential function:

$$D = A * (\exp(B * \epsilon_p) - \exp(D * \epsilon_p)) \quad (2.17)$$

This can be a bit misleading. Stiffness in this context is the same as Young's modulus. Rewrite?

The study concludes that the damage parameter calculated with the volumetric deformation underpredicts the damage occurring. A possible reason is that besides voids and crack that might be captured with the volumetric strain, microcracks that do not lead to macroscopic volume change also contribute to damage.

Christensen [54] published a detailed book on failure criteria, but did not take into account materials that exhibit strain softening, therefore his extensive work does not discuss this behaviour.

Rodriguez [22] investigated yield modelling for composite materials under multi-axial loading. He implemented a theory proposed by Tsai-Hill for composites that defines failure for composites. Originally the Hill theory was developed for anisotropic ductile and brittle materials. Different variations are used for either failure or yield criteria. The surface is assumed to be quadratic in the stress components. Details on these yield criteria can be found in books on composite mechanical behaviour [43, 64].

## FRACTURE

Another failure approach is the study of fracture in cracked surfaces. Among the three opening modes, mode I requires the smallest stress to propagate the notch. Therefore, it is considered as the most destructive mode and is often used to estimate the material toughness. A sample weakened by a notch and or crazes will exhibit a lower Youngs modulus, therefore, the stress at break,  $\sigma_b$  is lowered. On the opposite  $\sigma_y$  is only slightly modified. Classical fracture theories can be implemented for crack growth and fracture, these assume a thick plate with a crack of length  $2a$ . An approach that combines Irwin criterion and the approach of Griffith is that a sharp crack can propagate within an finite sample under a critical stress:

$$\sigma_{cc} = \frac{K_{Ic}}{\sqrt{(\pi * a)}} \quad (2.18)$$

where  $K_{Ic}$  is the critical stress intensity for mode I loading. This relates the value of the local stress intensity in the surroundings of the crack tip to the applied loading and is dependent on the material and geometry of the crack.

The  $K_{Ic}$  has a correlation with the material energy release rate,  $G_{Ic}$  under plane strain state, involving the Young's modulus and the Poisson ratio according to:

$$K_{Ic} = \frac{E * G_{Ic}}{\sqrt{1 - v_p^2}} \quad (2.19)$$

Irwin was the first to take into account that stress concentrations at the crack tip may be large enough to move from a local elastic to a plastic response. The radius of the plastic region,  $r_y$ , as is shown in figure 2.42 has been modeled by Irwin under plane strain with the following dependency:

$$r_y = \frac{1}{6\pi} * \left( \frac{K_I}{\sigma_y} \right)^2 \quad (2.20)$$

There are different ways to calculate  $K_{Ic}$  and  $G_{Ic}$ , but this thesis will not go into the details of determining these values. These values are dependent on numerous polymer characteristics, such as chemical structure, molecular weight, glass transition temperature, etc. It should be noted that the values shift with the thickness of the specimen and is significantly higher for plane stress than for plane strain. Therefore, this method is less

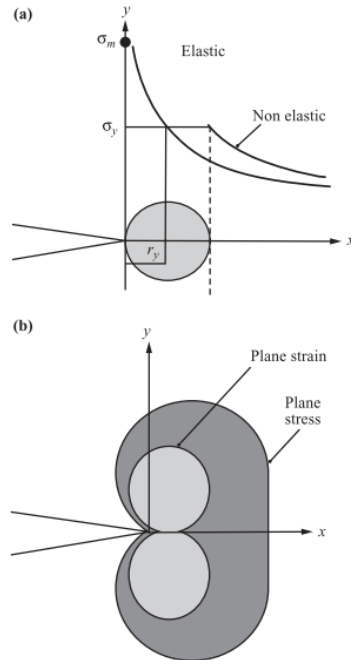


Figure 2.42: Geometry of the plastic zone at a crack tip a) Irwin model b) analysis using von Mises stress[47]

appropriate for parts not consisting of plates. Chain entanglements play a fundamental role in fracture properties. Correlations between the fracture properties of polymers and their entanglement density,  $v_e$  were found by Halaray et al. [47], as can be seen in figure 2.43. These empirical results show that there is a linear dependence between the two factors as would be predicted by theory. Unfortunately, the work of Halary et al. does not include investigations on ABS polymers. Oskui [65] determined a fracture toughness of  $4.32 \text{ MPa m}^{-3/2}$  for a 10 mm thick specimen.

### 2.2.5. APPLICATION OF ABS FOR FFF

Due to its low glass transition temperature, its ease of processability, low cost and decent mechanical properties, ABS is a popular polymer to be used for FFF printing of functional parts. Since PLA is even cheaper and easier to use, this polymer is generally used for prototyping and aesthetic parts. Polymers such as PETG, PC and PA are generally used for functional parts. When printing without a heated chamber, polymers with high  $T_g$  (for PC  $T_g \approx 147^\circ\text{C}$ ) will lose a significant part of their properties due to bad bonding. ABS has a relatively high glass transition temperature ( $T_g \approx 105^\circ\text{C}$ ), PETG ( $T_g \approx 80^\circ\text{C}$ ) and PA ( $T_g \approx 60^\circ\text{C}$ ) will have less issues with this. What causes difficulty for the use of ABS with FFF is warping. Coating the build surface with an adhesive will

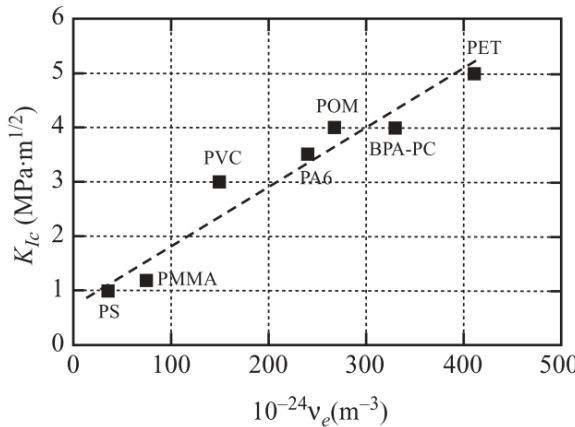


Figure 2.43: Correlation between toughness,  $K_{Ic}$ , and entanglement density,  $v_e$  [47]

significantly reduce warping.

It is important to note that the parts produced with FFF are weakest at the inter-laminar interface, and that in different loading conditions the parts most certainly will fail at the laminar interface [24, 49]

### 2.2.6. STANDARD PARAMETERS FOR ABS

The technical data sheet of ABS produced by Ultimaker [66] assumes the "fine" settings in Cura. These include a 0.4mm nozzle printed at 240 – 250 °C and has a build plate temperature of 85 °C, additionally it has a printing speed of 55 mm/s. These settings are recommended for an optimal print, the amount of infill orientation and shell architecture is up to the judgment of the producer. Automatically the slicer produces a shell of about 3 roads thick and applies an infill of 20-50% filled with a triangle structure. Due to differences in parameters, difference in material and system, lack of standardization, qualification and characterization of results, the produced parts by different researchers will differ widely. Therefore it is difficult to compare the different empirical results from different researchers and datasheets; e.g. the UM datasheet only states that the test specimen are printed with 90% infill, but the orientation, geometry of the infill and additional parameters have a crucial influence on the mechanical properties of the part.

### 2.2.7. STANDARDIZATION

In the prior sections it has been made clear that there are a wide range of parameters that can be adjusted. However, there is limited guidance in the standardization of the production process to produce a procedure that can be reproduced. Different researchers have tried to create standardization for their work, generating a multitude of different parameters that are being used, this is well portrayed by review studies such as [26] and

[49]. Most plastic producers give relatively little to no information on the process parameters used to test their filament, as can be observed in the Ultimaker ABS datasheet [66]. One of the most important characteristics that fluctuate in parts being produced (even if the same process parameters are used), is the healing, wetting and porosity in parts. Although the wetting and porosity can be analyzed by observing the mesostructure, it is extremely hard to characterize the extent of polymer entanglement that will result in road bonding. Employing good hardware (such as a constant envelope heater), reliable sensors and thermocouples and high quality robotics and stepper-motors will generate more consistent results. After a part is produced it can be checked through some relatively easy steps to determine the quality as described by Tanikella et al. [67], e.g. one can weigh the produced part to create an estimation for the porosity, and to determine the fluctuation in extrusion by comparing it with the calculated weight by the slicer. Additionally, one could perform a density test by applying the Archimedes principle.

In the past years efforts have been made to use standard printing processes and test procedures. NIST [68] published a standard for testing additively manufactured polymer materials, including FFF thermoplastic testing. These test methods advise using either ISO 527-2 [53] or ASTM D638 [69] for tensile test, which both describe the tensile test for thermoplastic polymers. They are similar on most points, indicating a geometry and test conditions for the experiments, including a sample size of 5 specimen per test. In general this seems like a decent test method, however, in some cases (due to the large anisotropic behaviour and nonuniform bonding between roads) the test specimen fails in unexpected ways, often failing at the clamps or the fillets due to stress concentrations [70], or having consecutive roads failing due to bad layer bonding and surface roughness [32, 71].

As an alternative to the ISO 527 or ASTM D638 standard, a composite alternative is proposed by Rodriguez [21], which applies the ASTM D3039 on his tests, which are normally used for long fiber samples. The advantage of this standard is the fact that it does not have fillets at the end of the sample, reducing the stress concentration and possibility for defects.

The document presented by NIST [68] still lacks standars on the production of test specimen. Additionally, ISO and ASTM published useful documents on general principles and terminology including ISO 17296 [72], ISO/ASTM 52900 [73], ISO/ASTM 52901 [74], ISO/ASTM 52910 [73], ISO /ASTM 52921 [75], ASTM F2971 [76], the last standard assumes a coordinate system (figure 2.23) which will be used for further reference. A book on standards and quality control was presented by Chua et al. [77]

Rodriguez [22] has assumed three normal material directions in line with the Chauchy stress tensor to simplify the reference to the road structure as can be seen in figure 2.44. This is in accordance with the notation for orthotropic materials such as long fibre composites.

If one were to produce test specimens, the convention states that the orientation of the test specimen has two directions which define the orientation of the test specimen, the first being the direction of the longest side of the specimen, the second being the smaller side. In figure 2.23 the coordinates for sample production are defined. To define the di-

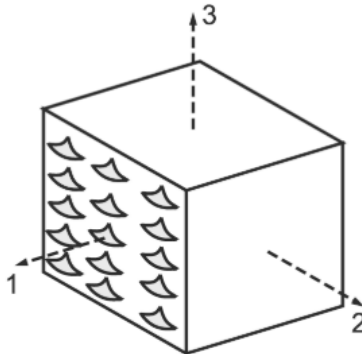


Figure 2.44: Three principle directions in the axis of asymmetry

rection of the roads (the raster orientation) one could look at the slicer software used (in this case Cura) which defines the deposited road orientation at the angle [0] to be in the Y direction (therefor [90] is in the X direction). Multiple papers use different orientation systems which can be quite confusing and ambiguous. To be consistent and easily comprehensible, this convention will be used throughout this thesis. This will be important when referring to orientations and tested samples in rest of the report.

After damage or delamination of a layer or a set roads, the properties of the part change, which create a difficult situation to model. Li et al. [20] have developed numerical approaches that use composite theories including elasticity, softening and debonding. Since these are complicated and strongly dependent on the process parameters, these will not be further discussed here.

## 2.3. FFF PROPERTIES

We have concluded that the process parameters largely influence the properties of FFF produced parts and are dissimilar from conventional produced counterparts. It is made clear that the products from this process create significant anisotropy resulting in orthotropic parts (three mutually perpendicular planes of symmetry), porosity, weak layer/road interfaces and surface roughness and inconsistencies. The benefits from FFF produced parts are the geometrical freedom, almost negligible start-up cost due to the absence of a mill or expensive machinery, relatively fast production, integration of different parts without the need of joining and for, Defense applications, the large logistic freedom to create parts in remote areas.

### 2.3.1. EXPERIMENTAL MECHANICAL CHARACTERIZATION

Conducting experimental tests with constant process parameters and 100% infill in the three general directions (as is shown in figure 2.44) will give more insight in the mechanical behaviour of FFF products. The notation of the produced samples in the 3 directions

are respectively; YX[0] direction 1, XY[0] direction 2 and ZY[0] direction 3. The properties that govern their behaviour are: the axial road properties (intra fiber properties), the horizontal (adjacent, inter fiber properties) road bonding, the vertical (stacked, inter fiber properties) layer bonding. This theory is supported by different papers including work done by Alaimo [70].

I am not sure if this is still clear...

2

Intuitively, the YX[0] specimen would generate the best behaviour, since there are no bonds in the direction of the load. Montero [37] concluded that the bond between layers in shear is stronger and stiffer than between roads. They also did a tensile test including horizontal specimen with transverse and axially aligned rasters, the results of his stress strain graphs are shown in figure 2.45.

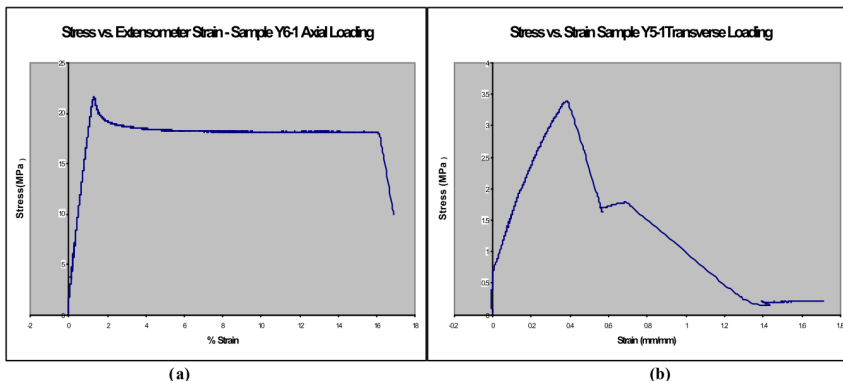


Figure 2.45: a) (YX)[0] b) (XY)[0] [37]

Multiple researchers did similar research, which is limited to the research of the raster orientation in the horizontal plane. This lacks information concerning the layer bonding ZY[0]. Rodriguez et al. were probably one of the first to analyze the mechanical behaviour of different FFF orientations, they provide a clear graph (figure 2.46) comparing the results with bulk ABS [21]. This graph clearly suggests an almost linear elastic region with a perfect plastic response for the longitudinal direction and a linear elastic brittle behaviour for the transverse directions.

Without knowing the exact behaviour of the ZY[0] test (3 direction), we can predict (using the properties stated in the TDS of Essentium [78] that it might respond similar to XY[0] but with a lower yield (and UTS) point. However Essentium indicates that the flexural properties of a XY[0] sample are worse than ZY[0]. Montero indicates shear in XY[0] is also worse. Be advised that these experiments are made with different settings and materials, so no conclusions could be made before obtaining comparable data. Blok [23] indicates that the stiffness can be 11% lower and tensile strength up to 50% lower in the XY[0] and ZY[0] direction compared with the YX[0] direction.

Rodriguez [21] also tested the filament and additional features such as crazing and necking. Localized whitening of the specimen has been observed before the yield stress was reached. Failure occurred at whitened areas where localized fiber delamination oc-

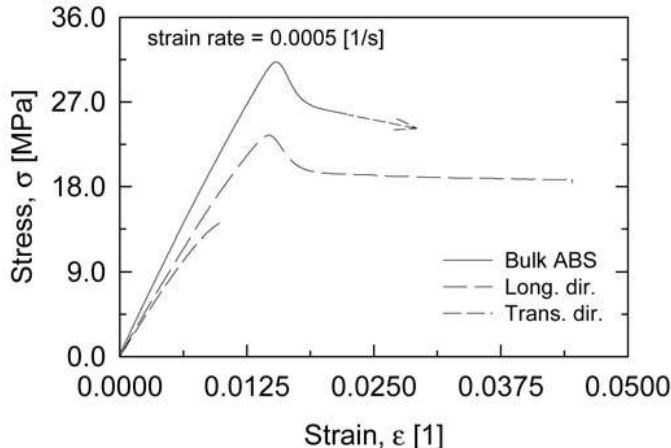


Figure 2.46: stress strain graph for (YX)[0] (long.dir.) and (XY)[0] [21]

curred, these white areas can also be caused by shear bands. He concluded that crazes propagate much faster along the bonding regions than they do in the ABS bulk due to the low interface strength. When loading in the axial direction of the roads there is a small amount of necking observed [79], which is in line with the stress-strain curve of figure 2.46. Since crazes are formed due to the plastic deformation induced by polymer stretching, crazing at interroad bonds should suggest a high degree of polymer entanglement.

One of the last things to mention about the result of FFF parts is the assumption of the thermal residual stresses induced by the process. Since they show visco-elastic behaviour at room temperature, one would suggest that the chains would relax over time towards a relaxed state. It has been shown [27] that thin walled polymer samples with a low  $T_g$  will relax its chains after a period of time resulting in a strain in the z direction.

Annealing and post processing has been discussed to some extent in academic literature (e.g. by Thomas and Rodriguez [12]).

### 2.3.2. MESOSTRUCTURE

The mesostructure of a FFF part (the road structure on 0.1 to 1 millimeter scale) characterizes a significant amount of the mechanical properties of the FFF produced part. It was already discussed that the laminate-like nature of the FFF parts resembles composites. Multiple studies [18, 19, 21] were conducted to characterize the mesostructure by microtomining, a process to cut micrometer thick slices of a specimen, this procedure will be further discussed in chapter 4. Afterwards the sample is inspected with optical microscopy and a digital image is produced. This procedure is used in different scientific fields and has been adopted for the inspection of the cross section of FFF sam-

ples. A few, among which Enrique Cuan-Urquizo [36] (figure 2.47) and Ahn [32] (figure 2.48) observed the mesostructure with SEM (scanning electron microscope). This gives a more detailed perspective on the mesostructure, but might be too expensive and time-consuming for multiple investigations.

The fundamental mesostructure (cross section of XY[0] specimen) is a structured stacking of multiple roads in a rectilinear cadence. If standard extrusion settings are implemented with a well calibrated system, the FFF system should deposit a road structure similar to the one seen in figure 2.15b. As has been discussed in the section 2.1.3, the process parameters have a large influence on the result on the mesostructure. The mesostructure could be optimized (meaning a decrease in porosity) by increasing the flow multiplier.

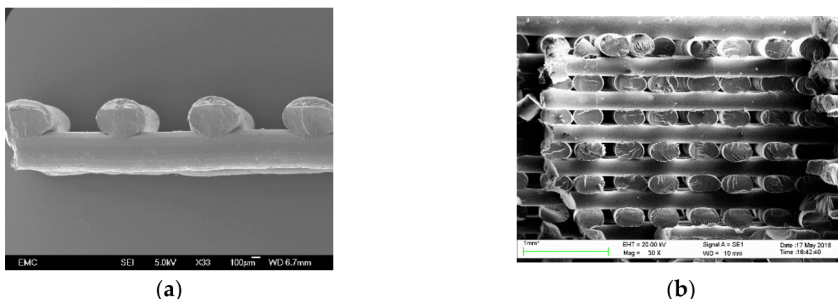


Figure 2.47: Mesostructure observed with SEM by Cuan-Urquizo [36].

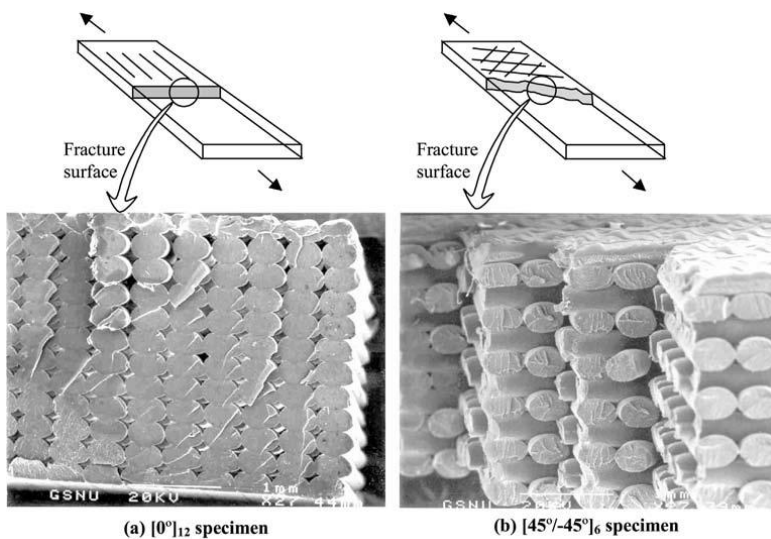


Figure 2.48: Mesostructure observed with SEM by Ahn [32].

These micrographs give an abundant amount of information on the road structure, wetting, necking and the amount of porosity in a part. This type of characterization is essential to determine the quality of the parts and the consistency of the process. Different systems, parameters and materials have influence on the results of the mesostructure. There is also a common consensus in these studies that the degree of polymer bonding (and consequently weld strength) are a function of the temperature and time of the contact area between two roads. Although, there is not a common agreement on the form of the roads nor the connection to the process parameters and the degree of overlap. The roads are interpreted as different forms by different academics, including ellipses, ovals and oblongs. Someridley [19] and Sun [14] assume ellipses in their work, the disadvantage is that the overlapped material is not accounted for.

It is difficult to make a good assumption concerning the form of the roads in the mesostructure, since the form is largely influenced by the process parameters and other non-controllable process phenomena which result in a relatively complex form. However, characterizing the road forms is relevant because it enables to model the geometry of the mesostructure in FEA for the prediction of mechanical properties. This will be further discussed in chapter 5.

## 2.4. COMPOSITE THEORY

Since it was concluded that FFF parts are anisotropic and have particular mechanical behaviour due to the processing conditions, it is difficult to predict the properties of such parts. Therefore, it would be beneficial if these properties were possible to model, so the parts could be implemented based on the prediction from the models.

### 2.4.1. ELASTIC MODELLING

#### STIFFNESS IN ORTHOTROPIC MATERIALS

As has been discussed in section 2.3 we can conclude that the layers are thin and behave as orthotropic materials. Therefore, orthotropic constitutive relation for plane stress can be considered, a similar approach has been found in multiple papers [19, 22, 80]

The stress strain relation for an orthotropic body can be written in the contracted notation as

$$\begin{vmatrix} \sigma_{11} \\ \sigma_{22} \\ \sigma_{33} \\ \sigma_{12} \\ \sigma_{23} \\ \sigma_{13} \end{vmatrix} = \begin{vmatrix} C_{11} & C_{12} & C_{13} & 0 & 0 & 0 \\ C_{21} & C_{22} & C_{23} & 0 & 0 & 0 \\ C_{31} & C_{32} & C_{33} & 0 & 0 & 0 \\ 0 & 0 & 0 & C_{44} & 0 & 0 \\ 0 & 0 & 0 & 0 & C_{55} & 0 \\ 0 & 0 & 0 & 0 & 0 & C_{66} \end{vmatrix} \begin{vmatrix} \epsilon_{11} \\ \epsilon_{22} \\ \epsilon_{33} \\ \epsilon_{12} \\ \epsilon_{23} \\ \epsilon_{13} \end{vmatrix} \quad (2.21)$$

Since this matrix is diagonally symmetric, the amount of elastic constants is reduced to 9. Plane stress is achieved by defining  $\sigma_{33}=0$   $\sigma_{23}=0$   $\sigma_{13}=0$ . The compliance matrix  $|C|$

written becomes:

$$\begin{vmatrix} \epsilon_{11} \\ \epsilon_{22} \\ \epsilon_{12} \end{vmatrix} = \begin{vmatrix} \frac{1}{E_1} & \frac{-v_{12}}{E_1} & 0 \\ \frac{-v_{12}}{E_1} & \frac{1}{E_2} & 0 \\ 0 & 0 & \frac{1}{G_{12}} \end{vmatrix} \begin{vmatrix} \sigma_{11} \\ \sigma_{22} \\ \sigma_{12} \end{vmatrix} \quad (2.22)$$

The stresses and the stiffness matrix  $|Q|$  can be acquired by inverting equation 2.22 resulting in

$$\begin{vmatrix} \sigma_{11} \\ \sigma_{22} \\ \sigma_{12} \end{vmatrix} = \begin{vmatrix} \frac{E_1}{1-v_{12}v_{21}} & \frac{-v_{12}E_2}{1-v_{12}v_{21}} & 0 \\ \frac{-v_{12}E_2}{1-v_{12}v_{21}} & \frac{E_1}{1-v_{12}v_{21}} & 0 \\ 0 & 0 & G_{12} \end{vmatrix} \begin{vmatrix} \epsilon_{11} \\ \epsilon_{22} \\ \epsilon_{12} \end{vmatrix} \quad (2.23)$$

The resulting independent material constants,  $E_1, E_2, v_{12}$  and  $G_{12}$  are needed to determine what the mechanical response of a thin FFF product would be.

### MECHANICS OF MATERIALS

The mechanics of materials approach is based on simplifying assumptions of either uniform strain or uniform stress in the constituents. These predictions are adequate for longitudinal properties such as Young's modulus  $E_1$  and major poisson's ratio  $v_{12}$ . These properties are not sensitive to fiber shape and distribution, this approach underestimates the transverse and shear properties [43].

### RULE OF MIXTURES

The rule of mixture (ROM) is a commonly used principle in the application of composites. When two different materials are combined in a solid, the ROM can combine different material properties to predict the new solid characteristics. When loading a composite ply in the 1 direction (along the fibre axis), the elastic properties can be predicted by this rule, which is also called the parallel or Voigt micromechanical model [43]:

$$E_1 = V_f * E_{1f} + (1 - V_f) * E_{1m} \quad (2.24)$$

where  $E_1$  is the elastic modulus of the ply in direction 1,  $V_f$  is the fibre volume and  $V_m$  is the matrix volume. Following this formula, and considering the ABS roads as  $V_f$  and the porosity as  $V_m$ , one could predict the elastic properties in the 1 direction by obtaining the void density in the 1 plane.

The different approach can be used for loads in the transverse (2) and (3) directions. The model used for composites is called series of Reuss model [43]:

$$E_2 = \frac{E_{2f} * E_{2m}}{(E_{2f} * V_m + E_{2m} * V_f)} \quad (2.25)$$

However, this takes a few strong simplifications, since the cross section of the voids are not continuous in the 2 and 3 directions in contrast to the 1 direction, it will be more difficult to determine the void density in the 2 and 3 directions. Li et al. [20] proposed an equation to account for transverse stiffness:

## 2

$$E_2 = \zeta(1 - \rho_2) * E \quad (2.26)$$

where  $\zeta$  is an empirical factor that takes into account the bonding strength,  $\rho_2$  is a linear void fraction along the transverse direction, so  $1 - \rho_2$  represents the relative contact area of the neck between roads. The void area density is determined according to empirical observations.

Rodriguez [22] proposed a method to obtain the  $E_1$  and  $E_2$  where he calculates the cross sectional void density to be squared voids with perfect bonding. He additionally assumes the void density to be uniform in any given plane through the solid.

$$E_1 = (1 - \rho_1) * E \quad (2.27)$$

The void area density in the 2 direction is assumed to be the square root (one side of the void) of the void area density in the 1 direction.

$$E_2 = E_3(1 - \sqrt{\rho_1}) * E \quad (2.28)$$

### CLASSICAL LAMINATE THEORY

It has been made clear that the FFF produced parts have a significant overlap with long fibre composites, due to the linear structure of the road in different layers a FFF produced part can be treated as a laminate with thick fibres and no matrix. The layer can be treated as a lamina or ply, and therefore the classical laminate theory can be employed to account its material behavior in the analysis of the plate. This approach has also been followed by different researchers including Somireddy [18, 19, 81], Alaimo [70], Li [20] and Casavola [82]. Most of them used it as a basis and benchmark for the development of models that predict the mechanical properties of different ply orientations.

Once the material properties of a single ply are acquired one can predict the properties in different orientations and have them stacked as a composite and predict the properties of the laminate as is shown in figure 2.49.

The analytical implementation of the Classical Laminate Theory is widely documented in composite books, and will not be discussed here in further detail.

### FINITE ELEMENT METHOD

FEM (Finite Element Method), is a popular method to perform structural analysis according to discretization of the geometry in small elements. Critically important is the definition of the constitutive models of the materials involved. When used to predict

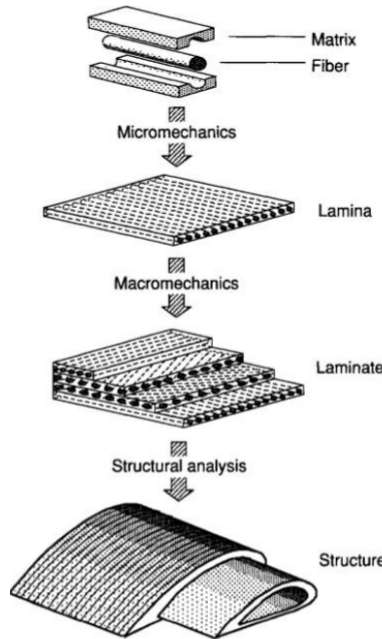


Figure 2.49: Principle of the Classical Laminate Theory [43]

the behavior of materials, the Finite Element Analyses (FEA) are conducted on Representative Volume Elements (RVEs) of the mesostructure and then the stress-strain relationship of the RVE is obtained by homogenization. This can be applied for composites when combining materials with different properties.

Studies from Garg [79] and Gorski [83], modeled the road structure in a whole part instead of an RVE. Both Garg [79] and Groski meshed a whole specimen with roads and performed a FE analysis for different loading conditions. Groski is one of the few that implemented plasticity and failure in his part. He implemented a standard model used by LS-DYNA.

#### HOMOGENIZATION APPROACH

An RVE homogenization approach in combination with the Finite Element Method (implemented with Abaqus software) was proposed by Melro et al. [84]. A composite consisting of long carbon fibres with an epoxy matrix was modeled at the micro-scale level, with the use of periodic boundary conditions (PBC's), an RVE could be defined to be representative of the bulk properties of the composite. Periodic boundary conditions enforce such a deformation on the volume element that the displacement of one of the nodes belonging to one edge must be related to the displacement on the corresponding node in the opposite edge [84]. The volume average of strain in the RVE equals the applied far-field strain.

$$\bar{\epsilon}_{ij} = \frac{1}{V_{RVE}} \int_V \epsilon_{ij} dV = \epsilon_{ij}^0 \quad (2.29)$$

2

In order to determine the stiffness tensor, where afterwards the 9 elastic constants can be retrieved by inverting the stiffness tensor to the compliance tensor, an analysis for each column should be carried out. Therefore, through the average volume stress from the elements in the RVE for the 6 different loading conditions the stiffness tensor can be found:

$$C_{ijkl} = \bar{\sigma}_{ij} = \frac{1}{V_{RVE}} \int_V \sigma_{ij} dV \bar{\epsilon}_{kl}^0 = 1 \quad (2.30)$$

Rodriguez [22] implements a method known as the asymptotic theory of homogenization. He assumed in his FEM model a mesostructure based on empirically obtained micrographs. This method allowed him to predict the Young's moduli in the 1 and 2 direction with an overestimation of approximately 5 percent. The reader is referred to his paper for further details. Apart from Rodriguez, Sheth [85] has investigated the homogenization method implemented in a damage prediction software, BSAM to predict the elastic properties of the RVE. Lui and Shapiro [86] used Green's functions to find the elastic moduli for a part fabricated by FFF. In the homogenization method used in Somireddy's work [19] a RVE is treated as a macroscopically homogeneous orthotropic material. He used a similar method to Melro to homogenize the RVE. Somireddy however, took different sizes of RVE's based on elliptical road geometry in different directions.

## 2.5. SUMMARY

From the literature review we can conclude that the process parameters largely influences the properties of FFF products. The three main contributors to the mechanical quality of the part are: the healing and wetting between the roads which is governed by the temperature history in the process; the mesostructure of the cross section which dictates the amount and geometry of porosity, which is mostly influenced by the process quality and printing strategy; and finally the properties of the plastic blend that is used.

Some plastics have the tendency for better healing and increased entanglements between roads, this is respectively a matter of the material property called glass transition temperature  $T_g$  and the entanglement density  $\nu_e$ . Due to the large amount of porosity in samples, the fracture toughness largely dominates the mechanical properties, which in turn is dominated by the entanglement density.

Thermoplastics have complex mechanical behaviour. Since the polymer chains act like independent molecules, the mechanical properties are highly dependent on the temperature and strain rate of the load. There are some constitutive models derived from

thermosets that predict the yielding, damage and failure of polymers to a certain accuracy. There is some work done on predicting elasticity of FFF products, but very limited results are achieved on non-linear modelling.

The standardization for production and testing of FFF products is very limited to this day, however, the experimental work done in this field is quite large. The lack of standardization makes it difficult to compare research.

FFF products exhibit large orthotropy, behaving like a laminate of multiple layers. Three principle directions can be distinguished when producing test coupons. The 3 directions decrease consecutively in mechanical properties. There is no solution yet to increase the isotropy in all directions.

Micrographs from different studies show some significant differences in mesostructure, researchers assume different shapes and models and there is not yet a consensus on the geometry of the mesostructure.

Since FFF products have large similarities with composites, different analytical and numerical composite theories have been applied successfully to predict the elastic behaviour of FFF products, these include the rule of mixture and the Classical Laminate Theory. There was no successful prediction on non-linear behaviour yet, to the best knowledge of the author.



# 3

## HYPOTHESIS AND RESEARCH QUESTIONS

### 3.1. KNOWLEDGE GAP IN THE CURRENT STATE OF THE ART

The current use and experimentation in the field of FFF tries to bridge the gap between simple consumer parts towards functional and mechanically reliable parts. For this a significant amount of effort has been put in the characterization of mechanical properties through loading tests, including the effect that process parameters have on the samples. It has been concluded that the properties are dramatically different from bulk material due to porosity and weak bonding areas. To be able to predict these anisotropic properties, different approaches have been proposed by multiple researchers, with considerable effort from Rodriguez et al [22].

To determine the effect of porosity on an FFF product the mesostructure is first analysed using micromotoring. The results from different systems can significantly alter in mesostructure, where the quality and accuracy of the mechatronics are most likely the cause of this discrepancy. Due to the different observations no clear agreement was concluded between the researchers on the formation of this porosity. The Ultimaker S5 is a current FFF systems that shows promise to achieve reproducible quality.

The empirical loading tests conducted by different researchers often used testing standards for isotropic polymers. The geometry of the samples used resulted in stress concentrations and crack initiation points, causing the samples to fail prematurely. Additionally, the production procedure is not yet standardized, meaning that the produced samples show significant difference between research methodologies.

There have been several attempts to analyze and predict the degree of bonding of the road interface. Since this is a complex time dependent parameter, no exact prediction was made to this date on the bonding between roads. Most researchers assumed perfect

healing (bulk properties) of the interface.

Multiple researchers found overlap between FFF products and composites, therefore they applied elasticity models such as the mechanics of materials approach and the Classical Laminate Theory to FFF products. Additionally, a few Finite Element Analysis were performed to determine the elastic properties of FFF products. The results of the elastic models are in accordance with the experimental results.

3

Since the non-linear behaviour of polymers is complex and difficult to predict, due to their molecular structure and strain rate dependency, the FEM knowledge on this topic is limited. For composites that incorporate an epoxy and long fibres, some validated models have been proposed on a micro-mechanical scale. Epoxies have a more predictive non-linear behaviour due to their cross-links. If the understanding of polymer molecular behaviour is sufficient, one could try to adjust the composite model to simulate the micro mechanical properties of FFF products.

### 3.2. HYPOTHESIS

Based upon the knowledge gap defined in previous section the following hypothesis has been formulated:

I updated the hypothesis

- High-fidelity FFF RVEs can be developed to predict not only the elastic behaviour, but also the complete non-linear elasto-plastic, damage and fracture behavior based on mesostructure characterization and elementary experimental tests of the base filament.

### 3.3. RESEARCH QUESTIONS

Verification of the above mentioned hypothesis involves addressing different research questions:

I simplified the questions and made them more specific.  
Please check.

1. What are the processes parameters that influence the mechanical properties the most?
2. How does the mesostructure obtained from the system in use (Ultimaker S5) differ from the literature, and can a geometric model for this porosity be defined?
3. What are the elementary tests of the base filament that allow to predict the mechanical behavior of the FFF RVE via FEA?
4. What experimental tests of the FFF specimens appropriately validate the FEA of the RVE?

## 3.4. RESEARCH METHODOLOGY

To answer the research questions stated in the previous section a research methodology needs to be defined. This section will describe the steps necessary to answer the research questions.

First the system under analysis, Ultimaker S5 (UMS5), is compared with results available in the literature to identify the process parameters that are influencing the mechanical properties.

Subsequently, the mesostructure is analyzed with micrographs to identify the form and amount of porosity in the UMS5 products. Then, the mesostructure is reproduced digitally and an RVE is defined for further analysis via the FEM. Ideally, this analysis is dependent of the process parameters.

The ABS filament is then tested to determine the bulk properties of the material. Hence, the FEA of the RVE can be conducted considering the mesostructure and the elasto-plastic and damage models. These models need to be adequate for polymers used in FFF, so it is important to implement the correct constitutive equations in the RVE model. Besides the RVE model, other analytical models can be compared to determine its effectiveness.

Finally, it is important to validate the developed RVE model with experimental tests of the FFF specimens and, perhaps include a comparison with other analytical models. The RVE model can afterwards be validated for different process parameters when additional process parameters are empirically tested. Note that different experimental tests may need to be considered for the FFF specimens because boundary effects that cause premature failure should not occur (otherwise, the RVE cannot be used to predict the mechanical behaviour).



# 4

## DIGITAL RECONSTRUCTION OF MESOSTRUCTURE: CREATING THE RVE GEOMETRY

In chapter 2 it was concluded that the FFF produced parts have inherent porosity due to the principle of the production process. In the literature, experimental analyses were performed to determine the amount of porosity in FFF parts. The results varied with system and process settings, which results in the hypothesis that the settings and the system has a large impact on the mesostructure of the FFF parts. To verify this hypothesis and to analyze the porosity of FFF parts it has been decided to perform a series of tests to identify the degree of porosity and the road structure for FFF parts produced on the Ultimaker S5. These tests have the goal to compare the results from the Ultimaker S5 with the results from the literature to validate the hypothesis and to obtain more knowledge on the geometry of the mesostructure. These results are needed to adjust the RVE model.

To achieve this different approaches are taken to gain insight on the degree of porosity and the geometry of the mesostructure. This includes a cross sectional microscopy analysis and a comparison with the micrographs from the literature. Based on this information a road geometry will be chosen for the RVE modelling and will also be compared with literature.

### 4.1. METHODS AND PROCEDURES

In this section the methods and procedures of the experiments will be presented.

### 4.1.1. CROSS SECTIONAL ANALYSIS

The literature uses a method of cross-sectional analysis to determine the porosity and mesostructure of FFF parts called micro-tomography. This method uses a machine that constrains a plastic or organic specimen and cuts fine pieces using a razor sharp blade, this process is illustrated in figure 4.1.

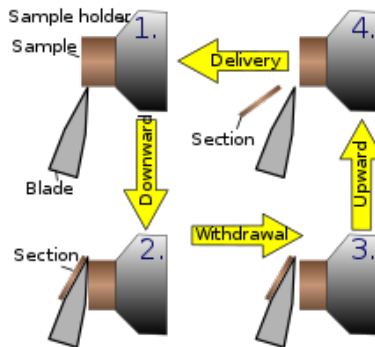


Figure 4.1: Microtome principle

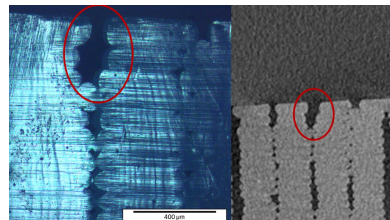
These pieces have a thickness that is thin enough to have light transmitted through them, images of these samples can be observed in figure 2.10 and figure 2.15. Since there is no microtome available at the TU Delft or TNO an alternative method was developed. The samples were printed out of ABS grade provided by Ultimaker [66].

The goal of cutting the sample was to obtain a cross-section of the part that is flat enough to perform optical microscopy without altering the material of the part. The first approach was to create a notch with a razor blade attached to a UTS machine before freezing the part in liquid nitrogen and break it with an impact test machine. This resulted unsuccessful, since the part shattered in multiple shards and only created ruptures in between the roads (the desired cross section surface is an perpendicular intra-road cut). After examining the resulting shards, the surface of the notch seemed relatively clean and smooth. After analyzing this surface with an optical microscope, the micrographs showed significant overlap with the microtomed samples.

To validate this method, results of a sample analyzed with Computer Tomography (CT) were compared with a FFF produced part by the DDDrop [27] in PETG which was cut with a UTS machine with a razor blade that is normally used to notch polymer specimen. The rate of cutting was kept low (2mm/min) to minimize the plastic deformation and allow the polymer to "creep" around the blade. The results are presented in figure 4.2 and seemed to have a large degree of coherence with the results of the CT scan. Images from the OM results were compared with the CT scan on a point that is in relative proximity (<5mm) in the axial direction. A particular point in the cross section of both images seemed to overlap in shape and position. Even if the location has not been fully verified, the image of the OM show a large enough overlap with the CT cross

section and the micrographs of the literature (figure 2.10 and figure 2.15) to assume that this method produces relevant micrographs to determine the mesostructure and road structure.

Therefore, it can be concluded that the method applied with the cutting of a sample through a UTS machine with a razor can generate relevant cross-sectional images that represent the mesostructure.



4

Figure 4.2: Optical Microscopy (left) and CT (right) [27]

The method that is used for the cutting of cross-sectional parts has therefore been defined as follows; a part produced according to table 4.1 is cut by a UTS machine (4.2) with a razor blade used for polymer notching at a compression rate of 2mm/min. The part is placed on a wooden frame base plate, and is cut with >1mm offset from the bottom.

#### 4.1.2. PRODUCTION STRATEGY

The used production parameters and hardware are defined in table 4.1. As is discussed in chapter 2, high speed has a negative effect on the mechanical properties, therefore an appropriately low speed was used to produce the samples.

Table 4.1: Parameters for cross sectional analysis

Parameter	
Line thickness	0.2 mm
Line width	0.4 mm
Speed	35 mm/s
Flow multiplier	100%
Printing temperature	230 C°
Bed temperature	85 C°
Thickness beam	4 mm
Width beam	10 mm

A part was produced in the YX[0] and analysed to determine the form and amount of porosity in the sample. Additionally a bi-chromatic YX[0] sample was analysed to observe the bonding between roads. The print strategy for the bi-chromatic sample is

Table 4.2: Hardware specification

Type	Hardware	Software
FFF system	Ultimaker S5	Cura 4.0
UTS system	Zick/Roell z010 10kN	Test Expert
Optical Microscope	CHECK!	CHECK!
Digital Microscope	plugable usb 2.0 digital microscope	plugable digital viewer
Computational Tomography	Phoenix nanotom CT	phoenix datos x CT

shown in 4.3. The slicer software is not able to define different types of filament for a resolution smaller than 4 roads.

## 4

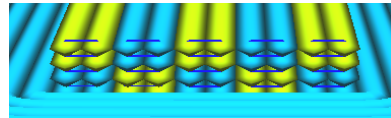


Figure 4.3: CURA visualization of the road structure

be consistent:  
use always  
UMS5 or UM  
S5

The dual head of the UMS5 allows to deposit alternating black and white roads. The extruding system is configured to deposit all roads of a type consecutively in a layer, this effect alternates between layers. This phenomenon alters the road structure slightly in comparison with single filament parts. Since the goal is to identify the adhesion and geometry of the deposited roads, the above mentioned phenomenon needs to be taken into account.

## 4.2. MICROSCOPY

The used optical microscope (4.2) has a default magnification of 10 and has a lens revolver with minimum magnification of 5. This would result in a magnification of 50, which would give an image of about 3 by 5 roads with the current process parameters. Since the micrographs with a magnification of 50 do not include the whole cross-sectional surface area, a set of points across the specimen where observed. This is also done to observe the effect of the razor blade on the sample. To achieve an image of the whole cross sectional area a digital microscope was used. The image produced with this microscope allows a larger view of the image.

## 4.3. RESULTS

The results of the optical microscopy are presented in figure 4.4 and 4.5.

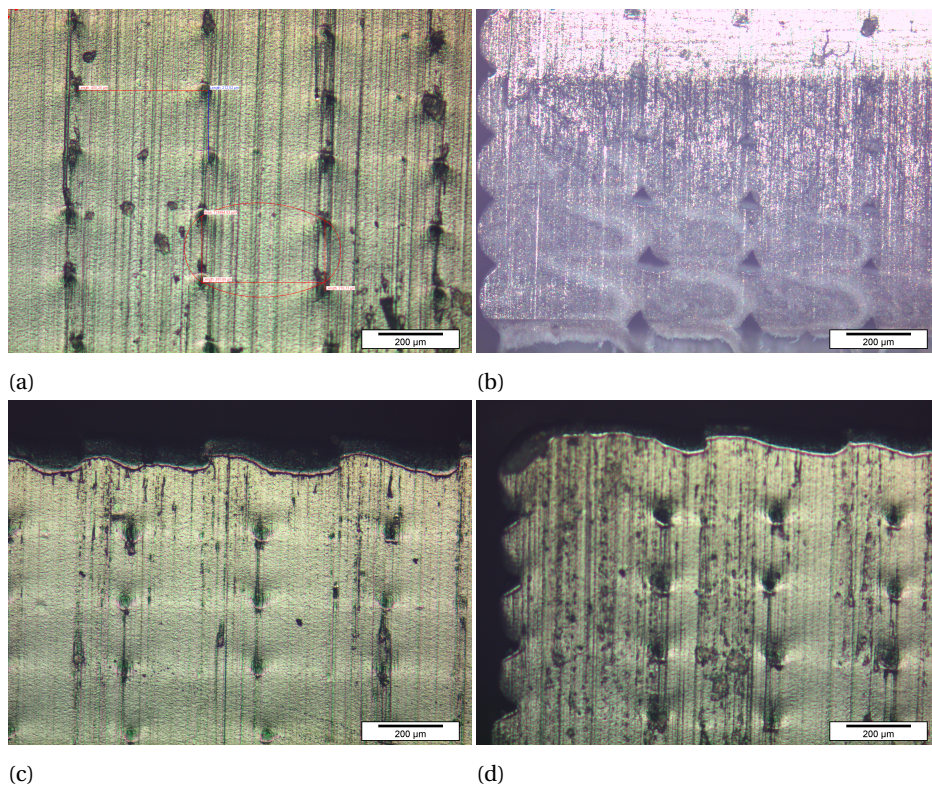
**4.3.1. OPTICAL MICROGRAPHS MESOSTRUCTURE REGULAR ANALYSIS**

Figure 4.4: Mesostructure of different positions, produced according to table 4.1. (a) middle, (b) left bottom, (c) top, (d) left top

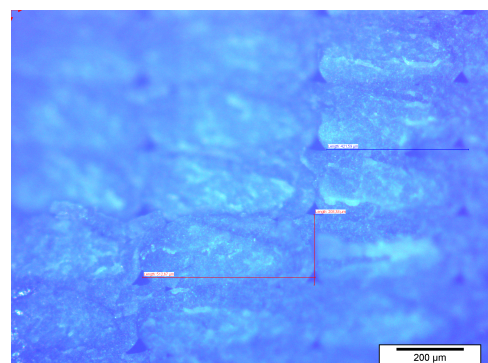


Figure 4.5: Fractured surface observed with optical microscopy

Define top,  
sides and bot-  
tom with a  
schematic

In figure 4.4 images of different regions of the mesostructure are shown (surfaces at the top, sides and bottom). In figure 4.5 a fracture cross section is showed after a specimen was subjected to a tensile test. The image is blurred due to the rough failure surface.

### 4.3.2. OPTICAL MICROGRAPHS MESOSTRUCTURE COLORED ANALYSIS

The results of the optical microscopy of the colored analysis are shown in figure 4.6 and 4.7. As can be seen, these roads have alternating color. Figure 4.7 shows a 500x zoom on a road interface to observe the weld between different roads.

4

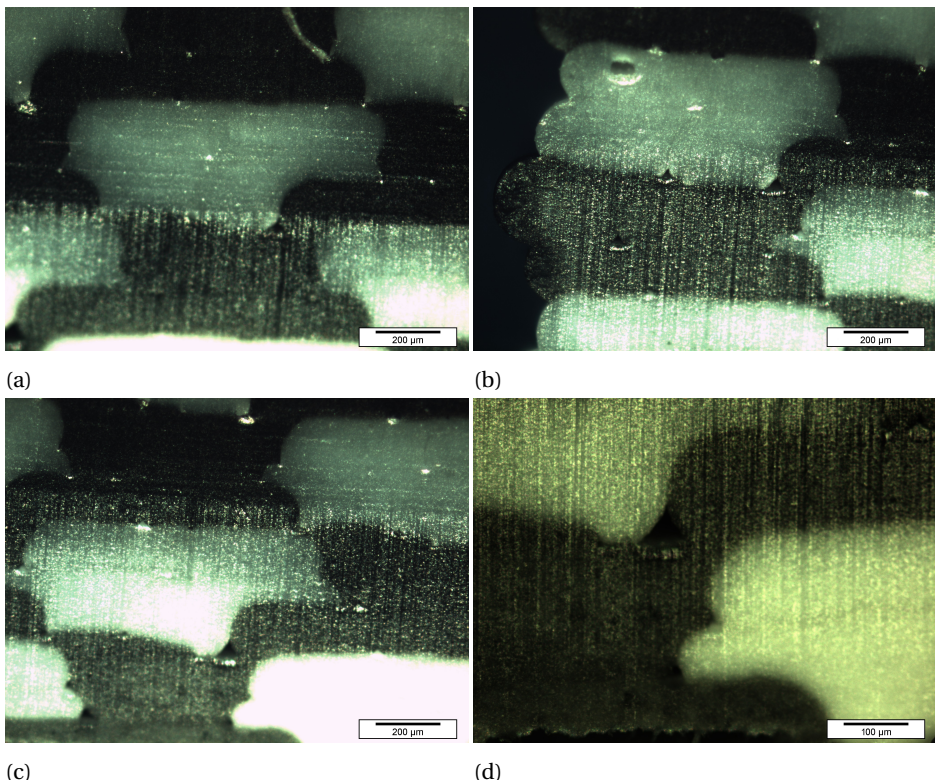


Figure 4.6: Cross sectional mesostructure of the colored roads at different positions.

### 4.3.3. DIGITAL MICROGRAPHS MESOSTRUCTURE COLORED ANALYSIS

In figure 4.8 a larger cross section of the colored roads is shown.

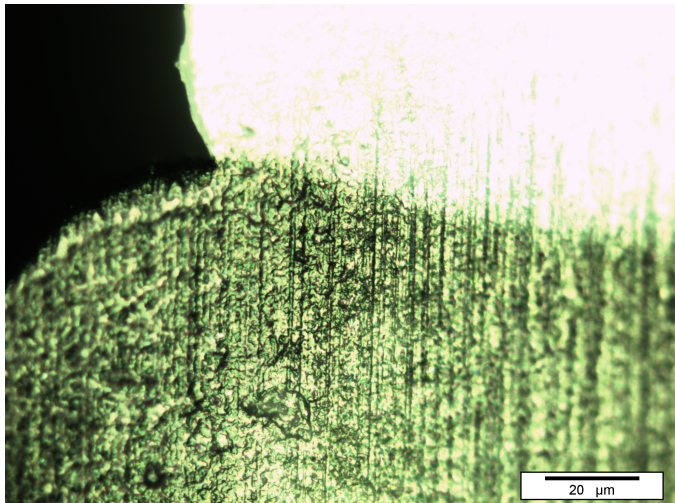


Figure 4.7: Road interface 500x zoom

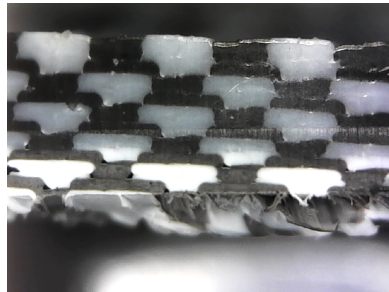


Figure 4.8: Digital microscopy of the colored road analysis

#### 4.4. DISCUSSION

In the investigated micrographs (figure 4.4) it can be clearly seen that the porosity is significantly different from the mesostructures defined by the literature, figures 2.10 and 2.15. The porosity of Somireddy, figure 2.15, exhibits a diamond shape. In the porosity analyzed by Rodriguez 2.10 a more triangular cavity is observed. The SEM pictures of Ahn, figures 2.48 and 2.47, show a different form, where the cavities are quite large and the form is shaped like a four armed star. Other micrographs, e.g. presented by Li [20] show a reversed triangle as porosity. The differences in porosity suggest a strong dependency on process hardware and process parameters.

The produced micrographs have triangular shaped cavities, which is clearly seen in figure 4.4b and figure 4.5. Figures 4.4a, 4.4c, 4.4d have a particular form, resembling dots. The pressure of the cutting knife could have deformed the mesostructure significantly. Another explanation might be the accumulation of material towards the top, reducing

the porosity.

Since the slicers are modeled to create a certain percentage of overlap (5-10%), pushing the roads closer together, some of the material of the extruded road is "pushed" on top of the road next to it. This eliminates the porosity of the top corner (the side next to the adjacent road) of the road that is being extruded. This theory is in line with the observed results, which show a lack of porosity which exactly matches the before mentioned effect.

The sides of the specimen show clear curvature of the molten roads. The spots between the curvatures are potential stress concentration points, which will be discussed in chapter 5. On the top the mono-chromatic sample (figure 4.4 (c) and (d)) there seems to be a certain amount of distortion (wave like artifacts), this can be accounted to the theory of overlap between roads. Additionally, the nozzle can create nicks in the roof by passing too close to the surface.

4

The multicolored specimen with black and white filament was produced to investigate the interfaces between road. The figures 4.6 and 4.8 are cross sectional micrographs of these multi-colored specimen, these show a significantly less structured mesostructure in comparison to the mono-chromatic specimen. This is likely due to the sequence of deposition; a type of filament is consecutively deposited in one layer, ensuing squeezing of the second type between roads due to the programmed road overlap. This phenomenon largely influences the density and the contact surface between roads, resulting in better mechanical properties.

The theory of the larger line width which causes overlap is supported by a slicer producer called "Slic3r" [35]. One of the programmers of Slic3r explains how the line width is calculated based on the porosity that needs to be filled. They assume that roads are extruded in rectangular shape with semicircular ends as can be seen in figure 4.9, this shape is generally referred to as "stadium shapes".

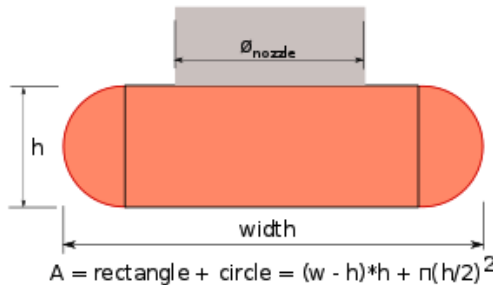


Figure 4.9: Road geometry according to Slic3r [35]

The height of these roads is defined by  $l_h$ , the distance between roads is defined by  $l_w$ . The ratio between these two is presented as  $R = (l_h/l_w)$ . These roads have a certain "extruded width", which is a function of line height  $l_h$  and line width  $l_w$  according to equa-

tion 4.1 and are deposited with a certain distance relative to the center of the adjacent road which is equal to the line width.

$$e_w = l_w + l_h \cdot (1 - \pi/4) \quad (4.1)$$

This creates a certain "overlap" defined as  $\Delta l$ , earlier defined as "negative airgap", which is defined by equation 4.2. Slic3r calculates this overlap in the "line width" based on the porosity that the geometry of the roads would generate to be filled up with the overlap surface. In figure 4.10 the yellow area represents the void area to be filled. If the roads were to be deposited closer to each other, an overlapped surface will emerge, which ideally would generate enough overlap to fill up both voids. He proposes an overlap factor (from 0 to 1) to find the optimum for filling in the void area's, the overlap factor represents how much void remains between the extrusions. It's difficult to estimate this amount, since it also depends on viscosity of the plastic, extrusion speed and temperature. In the this discussion we will assume the  $\Delta l$  to generate an overlap to fill both the cavities.

who?

4

If the road is deposited next to the adjacent road from the top, it is very unlikely that the bottom void is filled. To be sure that there is abundant material available to fill these voids, the line width is still defined based on a equal surface of void and overlap area. A similar process has been presented by Sun, Li and Bellehumeur [20] but results in a reversed triangle which is not in agreement with our micrographs. Tronvoll et al. [87] explain the same phenomenon in a recently published article.



Figure 4.10: Road overlap according to Slic3r [35]

The overlap  $\Delta l$  between roads is defined as the difference between extruded width  $e_w$  and line width  $l_w$ :

$$\Delta l = e_w - l_w \quad (4.2)$$

For a line ratio of 0.5, the  $\Delta l$  is equal to 0.043 mm, which is in line with the observations in literature, among others Somireddy, who observed a 10% overlap. The line ratio is recommended to be around 0.5, and is not recommended to surpass 1. In figure 4.11 the resulting RVE is presented.

The area of a road is subsequently calculated as:

$$A_{road} = (e_w - l_h) * l_h + \pi(l_h/2)^2 \quad (4.3)$$

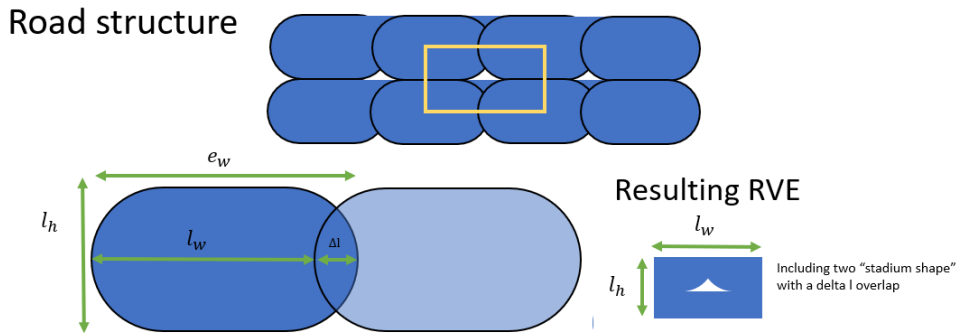


Figure 4.11: New defined road structure

4

And the area of the RVE with the simple relation between line width and line height:

$$A_{RVE} = l_h * l_w \quad (4.4)$$

Now that the form of the RVE is defined by the  $l_h$  and  $l_w$  parameters, we can define a relation of the void surface according to:

$$A_v = \frac{((l_h/2) - (e_w - l_w)/2)^2 * (l_h/2) - (\arcsin((l_h/2) - (e_w - l_w)/(l_h)) / (2 * \pi) * (l_h/2)^2 * \pi}{-\sqrt{(l_h^2 - ((l_h/2) - (e_w - l_w)/2)^2)} * (l_h/2) - (e_w - l_w)/2} * 2 \quad (4.5)$$

And the surface fraction of the RVE can be found with

$$f_v = \frac{A_v}{A_{RVE}} \quad (4.6)$$

With this information, we can identify the surface fractions in different directions as a function of the line ratio. The surface fraction of the 1 direction is straightforward, for the 2 and 3 directions it is more tricky since the cavity is not consistent in these directions. As is assumed by Li and Rodriguez, we can identify the largest void fraction in the cross section as can be seen in figure 4.12. For example, RVEs with ratio 1 and 1/8 are shown in figures 4.13 and 4.14.

This theory is validated if one were to look inside of the g-code generated by the CURA software. If the roads form according to the described process, stadium shapes with a certain overlap, one would observe that the commands of the g-code almost exactly overlap with this theory. The g-code enables the user to determine the coded material flow per second at a certain location. According to this analysis, the g-code matches the needed material flow per second within 2%.

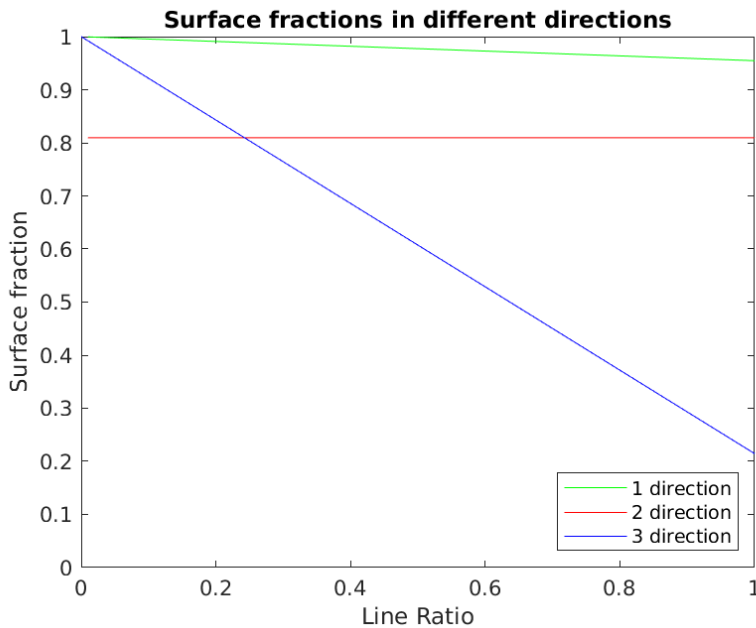


Figure 4.12: Surface fraction of RVE vs line ratio

## 4.5. CONCLUSION

With the information gathered from the literature, generated micrographs and slicer information a geometry can be defined that corresponds with our hardware and process parameters. The obtained micrographs show the same periodicity that can be found in the micrographs from the literature, additionally, it corresponds with the theory provided by Hodgson. In literature no good definition was given for this phenomenon, mainly due to the fact that different FFF systems produce a variety of mesostructures. With these definitions an RVE can be defined that is dependent on the line width and line height, the surface of the cavity can be predicted based on these parameters. Now that we have a model that can predict the volume, shape and location of the porosity, analytical and numerical models can be implemented to determine the effect of this mesostructure. Note that appendix A includes additional details of the derivation of the road deposition.

This road structure can be used as an RVE in further analysis, as discussed later. Recall that the goal is to investigate whether the FEM predictions for this mesostructure are in line with experimental results for specific line width and height parameters.

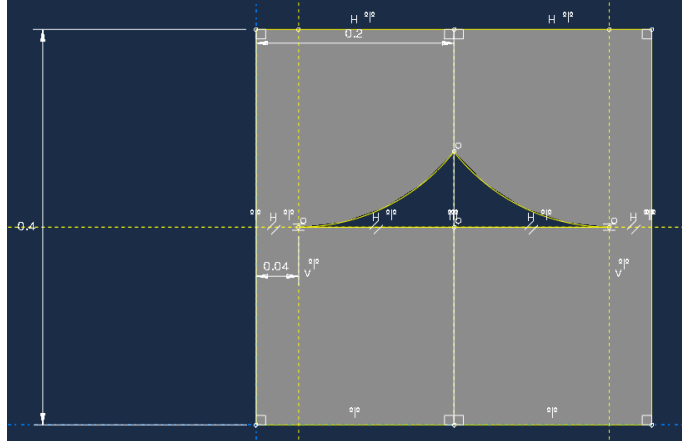
**4**

Figure 4.13: RVE with a ratio of 1

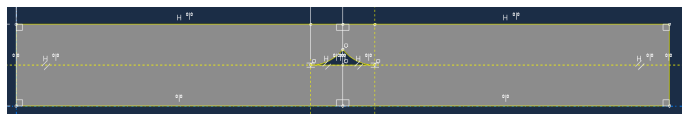


Figure 4.14: RVE with a ratio of 1/8

# 5

## EXPERIMENTAL TESTING

To gain a better insight on the mechanical properties of FFF produced ABS parts and the bulk filament, a series of experimental tensile tests were conducted. These tests are used afterwards as validation for the constitutive elasto-plastic models with damage to predict the mechanical behaviour. First a set of tensile tests in the three principle direction are conducted according to ISO 527[53, 88]. Since FFF produced parts show significant anisotropy and have no accepted testing standard, the results are non-satisfactory because premature failure occurs due to the geometry of the dogbone shape of the ISO 527 standard. Therefore an additional test is conducted using the ASTM D 3039 [89] standard, which defines a different geometrical shape, generally used for long fibre composites. Additionally, a ASTM D 3039 test with wall layers in the XY direction and a set of YX[45]n samples has been tested for shear. Finally, a set of filaments are tested to determine the bulk properties. These properties are important to implement in the RVE model, since it will determine how the plastic response of the bulk material will be.

### 5.1. METHODS AND PROCEDURES

In this section the methods and procedures of the experiments will be presented. All samples were produced and tested with the same hardware and parameters (with some exceptions). The tests are performed with the corresponding ISO 527 and ASTM D 3039 standards.

The samples are produced on a UMS5 machine with Ultimaker black ABS [66], a road width of 0.4 mm and a speed of 35 mm/min. For each set five samples were tested in the 3 principle directions (YX[0] XY[0] ZX[0] of figure 2.23). The samples were tested on a Zwick/Roell 10kN universal testing machine. The test was strain driven and included an extensometer of 50 mm gauge length that immediately processes the stress strain data in the Test Expert software. Before testing the samples, the dimensions of the cross

section were measured. It should be noted that the true dimension of the cross section can vary significantly from the nominal production dimensions. Additionally, the roughness of the sample makes it more difficult to exactly determine the cross section of the sample. This results in a inaccuracy of the true measured values for stress and Young's moduli.

The strain rates differ slightly per testing standard (ISO 527 and ASTM D 3039). Both advise a strain rate of approximately 1%/min for the calculation of the E modulus (both standards calculate the E modulus between 0.05% and 0.25% strain). ISO 527 specifies a speed of 1 mm/min while ASTM D 3039 specifies a test speed of 2 mm/min for the calculation of the *E* modulus, both correspond to approximately 1%/min, since both samples are in the range of 100-200 mm.

## 5

After the determination of the *E* modulus, which is calculated by a linear regression calculation between 0.05% strain and 0.25% strain, the strain rate can be adjusted. Since thermoplastics show significant viscoelastic behaviour this can significantly alter the obtained stress-strain curve. Both standards give a wide range of possible testing speeds, ISO 527 ranges from 0.125 to 500 mm/min. ASTM 3039 specifies that failure should occur in between 1 and 10 minutes after starting the tensile test. The tests conducted in literature often remained on the same strain rate as was defined for the *E* modulus. To make a better comparison between the tests from the different standards a strain rate of 2 mm/min was chosen for the strain rate after the calculation of the *E* modulus. In the plastic region, the yield point is defined as the top of the slope where the derivative of the stress strain curve is zero. If this point is not reached (due to failure), the yield point is defined at the same point as the break point.

### 5.1.1. ISO 527

The ISO 527-2 standard [53] prescribes a tensile test standard for thermoplastics. The 1A sample 5.1 was used to perform this test. The thickness of the sample is 4 mm.

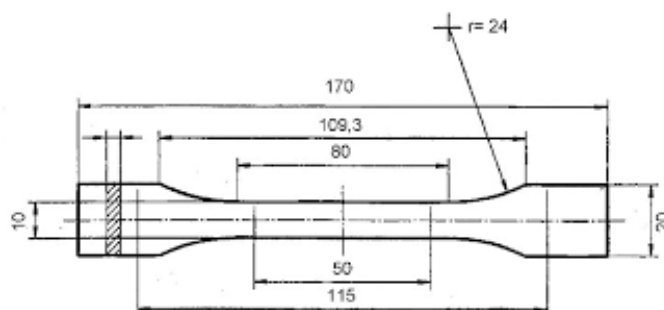


Figure 5.1: Dimensions of the ISO 527 dogbone used

### 5.1.2. ASTM D 3039

The ASTM D 3039 standard [53] prescribes a tensile test standard for long fibre composites. This standard has been used by Rodriguez [21] to prevent stress concentrations occurring at the fillets of the ISO 527 specimens. The geometry of the ASTM sample used was a simple rectangle with a nominal dimension of 110 x 20 x 4 mm, including an image is otiose. The ASTM standard advised to use a form of tabs at the interface of the grips and specimen to minimize the damage and stress concentration. The tabs should be slightly longer than the area where the grips are clamped. The tabs used for the ASTM 3039 sample were 20 x 30mm and made out of thick (approximatly 1mm) paper.

5

### 5.1.3. ULTIMAKER ABS FILAMENT

To determine the bulk properties of the Ultimaker ABS Filament a set of single filament pieces are tested. There is currently no testing standard for testing thick (nominal diameter of 2.85mm) thermoplastic filament. For the process parameters the settings of ISO 527 specified by the Ultimaker Technical Datatsheet [66] were largely followed. These include the E modulus testing of 1 mm/min followed by a strain rate of 50 mm/min. The hardware used is similar to the setup for the FFF produced samples. Ideally, special grips for filament would be used, since these were not available regular grips were used. FFF filament is inherently bent, to solve this problem the filament was straighten out and clamped before a pre-load of 5 MPa was induced to align the filament.

## 5.2. RESULTS

The results are presented in stress strain curves with the corresponding testing standard, images of the tested samples are presented when relevant. Every set includes a minimum of 5 tested samples. In the figure, the longest or most representative response is plotted together with the yield points of every sample. This gives a representation of the yielding behaviour and its consistency.

This is not a great practice... We should have done the same as Michael Houldier's thesis... I saw this too late...

### 5.2.1. ISO 527

In figure 5.2 and table 5.1 the results are presented of the ISO 527 samples with two wall layers.

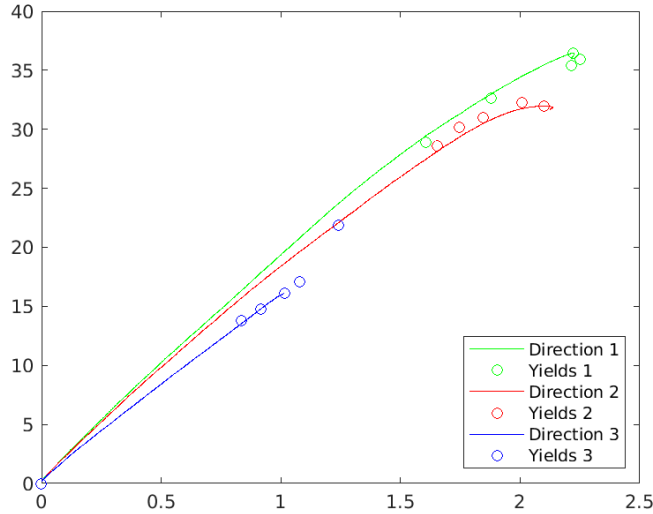


Figure 5.2: Stress strain curves of the ISO 527 samples

Table 5.1: Properties of the ISO 527 tests in the 3 principle directions

direction	$E$ avg. [MPa]	$E$ std. dev.	$\sigma_y$ avg. [MPa]	$\sigma_y$ std. dev.	$\epsilon_y$ avg. [%]	$\epsilon_y$ std. dev.
1 (YX[0])	2019	53	33.8	4.5	1.84	0.37
2 (XY[0])	1974	77	30.8	1.3	1.87	0.16
3 (ZY[0])	1793	119	16.3	2.8	0.95	0.19

In figure 5.3 the tested specimen of the ISO 527 samples are shown.



Figure 5.3: Tested specimen, left: YX[0], middle: XY[0] right ZY[0]

The results of these specimen show significant brittle failure (especially in the XY[0] and

ZY[0] direction). Most of the specimens fail in the region near the fillet of the specimen. The ZY[0] specimens failed at approximately the same point, at the beginning of the fillet.

### 5.2.2. ASTM D 3039

#### NO WALL LAYERS

In figure 5.4 and table 5.2 the results are presented of the ASTM 3039 samples with no wall layers. For comparison, observe figure 5.1 for the specimens tested with the ISO 527.

5

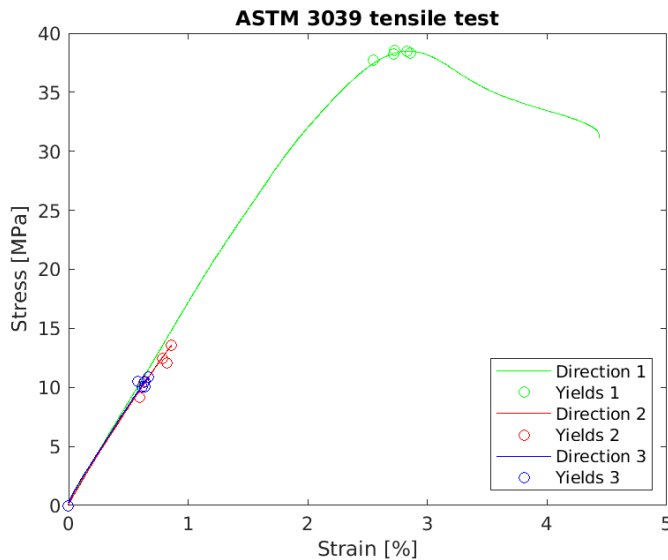


Figure 5.4: Stress strain curves of the ASTM 3039 samples with no wall layers

In figure 5.6 the tested specimen of the ASTM 3039 samples with no wall layers are shown. The YX[0] specimen showed much more ductile behaviour in comparison with the ISO 527 samples. However, the XY[0] and ZY[0] still showed significant brittle behaviour. The ZY[0] specimen failed again in the region near the clamps.

Table 5.2: Properties of the ASTM D 3039 tests in the 3 principle directions

direction	E avg. [MPa]	E std. dev.	$\sigma_y$ avg. [MPa]	$\sigma_y$ std. dev.	$\epsilon_y$ avg. [%]	$\epsilon_y$ std. dev.
1 (YX[0])	1811	62	39.1	0.29	2.84	0.11
2 (XY[0])	1616	85	11.4	2.21	0.73	0.14
3 (ZY[0])	1606	64	9.9	0.65	0.61	0.04



Figure 5.5: ASTM Tested specimen, left: YX[0], middle: XY[0] right ZY[0]

#### ADDITIONAL

In figure 5.6 and table 5.3 different results are presented of ASTM 3039 XY samples. A set without wall layers, a set with wall layers and a set with XY[45] samples.

5

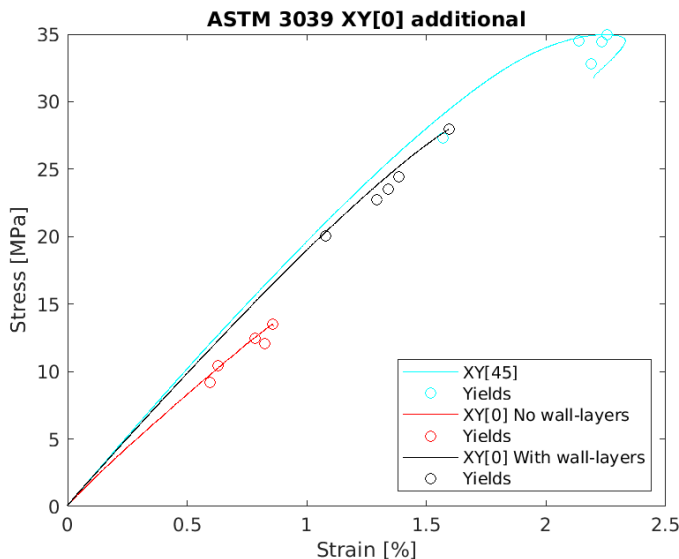


Figure 5.6: Stress strain curves of the ASTM 3039 XY samples, without wall layers, XY[0] with wall layers and XY[45] with wall layers.

In figure 5.7 the tested specimen of the ASTM 3039 samples with no wall layers are shown. The XY[0] sample with wall layers showed less brittle behaviour, and had a significant increase in yield strength. The XY[45] sample showed more ductile behaviour, even reaching the softening region.

Table 5.3: Properties of the additional ASTM D 3039 tests in the 3 principle directions

direction	$E$ avg. [MPa]	$E$ std. dev.	$\sigma_y$ avg. [MPa]	$\sigma_y$ std. dev.	$\epsilon_y$ avg. [%]	$\epsilon_y$ std. dev.
XY[45]	1945	72	32.8	2.83	2.07	0.26
XY[0] (No WL)	1616	85	11.4	2.21	0.73	0.14
XY[0] (WL)	1879	70.5	22.9	3.36	1.3	0.21



5

Figure 5.7: ASTM additional tested specimen, left: XY[0] (no WL), middle: XY[0] (WL) right XY[45]

### 5.2.3. ULTIMAKER ABS FILAMENT

In figure 5.8 and table 5.3 the results of the Ultimaker ABS filament are presented. Note that the stress strain curve is moved 0.225% to the right to determine the average representative properties. The sample was pre-loaded with 5 MPa to straighten the filament out, this corresponded to approximately 0.225% strain. This only affects the effective strain at yield and break.

In figure 5.8 the tested specimen of the ABS filament are shown. The set of tested filament showed a similar behaviour, but had significant difference in break point. Nonetheless the yield points are quite close to each other. The tested specimen show some whitening, which would indicate plastic deformation.

We should have offset the correct value by extrapolating the linear part... Be aware of this at the defense.

Table 5.4: Properties of the tested filament

direction	$E$ avg. [MPa]	$E$ std. dev.	$\sigma_y$ avg. [MPa]	$\sigma_y$ std. dev.	$\epsilon_y$ avg. [%]	$\epsilon_y$ std. dev.	$\epsilon_b$ avg. [%]	$\epsilon_b$ std. dev
Exp. fila- ment	2019	81.3	42.8	0.57	4.27	0.26	6.52	1.44
Injection molded [66]	2030	-	43.6	-	4.8	-	34	-

Check if I found the correct reference used in Table 5.4.

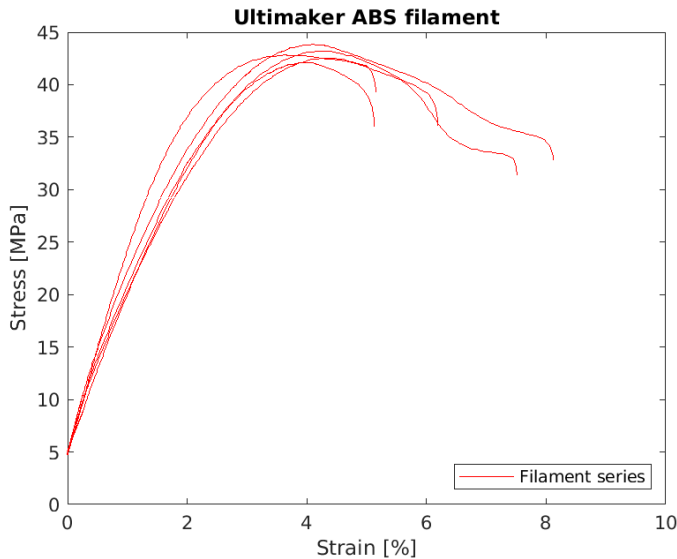


Figure 5.8: Stress strain curves Ultimaker ABS filament

### 5.3. DISCUSSION

The conducted experimental tensile tests of FFF produced specimen were produced to create a benchmark and to validate the FEM model that was created to predict the behaviour of FFF produced part. The tests of the ABS filament is used to create hardening curves that are imported in the FEM model. Overall, these tests also verify the results in the literature and give significant insight on the behaviour of FFF produced parts. During these test it is observed that the production technique, test method and environment had significant impact on the response of the stress strain curve. As has been analysed in the literature in chapter 2, the production parameters are inherently linked to the properties of FFF produced parts. Therefore, a standard set of production pa-



Figure 5.9: Tested Ultimaker ABS filament

rameters, which have proven to generate decent results, and that were close to the conducted experiments in literature, are chosen. This thesis will not investigate the effect of different process parameters empirically. The test method, where the most influential parameters include the geometry of the specimen and the strain rate, proved to significantly alter the response of the test. The ISO 527 specimen (dogbone shaped) exhibited major complication during testing. Failure is predominantly brittle and initiated at the beginning of the fillets. This is probably due to stress concentrations and crack initiation points.

Be aware that the geometry and printing strategy also affects the temperature history of a certain road interface. For example, the time a toolhead passes an interface of a adjacent road is much shorter in the xy plane than the z direction, since the printer first finishes a layer before moving in the z direction to a new layer. Therefore, considering the parameters in table 4.1, the toolhead in the xy plane for the XY[0] ASTM D 3039 test samples will reach the adjacent road 10 times faster than the inter layer interfaces for the respective ZX[0] sample (1 second versus 10 seconds). According to the healing theory, this would lead to a better healed interface for the XY[0] samples perpendicular to the loading direction, compared to the ZX[0] samples, assuming they are not fully headed. The results in figure 5.4 support this due to the lower UTS measured for the ZX[0] samples. However, we do not yet know if this is affected by the healing or by the difference in mesostructure. This will further be investigated in chapter 7.

Stress concentration occur when a load is applied along a body with a geometrically altering cross section [87]. The "dogbones" are designed to ensure failure in the mid region of the specimen and to compensate for the stress of the grips. However, for the FFF parts the stress is not transferred homogeneously, creating stress concentrations. Additionally, crack initiation points at the surface are produced during the production process, this is due to the sintering of the roads. Finally, the internal pores also act as crack initiation points. To limit the effect of the surface roughness and stress concentration, the ASTM 3039 standard was chosen to have an even cross section along the specimen. The results show that the ASTM 3039 samples provide a significant better response in the 1 direction, which implies that there is less stress concentration leading to brittle failure. Adding wall layers in the ASTM 3039 samples also significantly increases the response (factor 2) but still does not reach a softening region. The ASTM 3039 samples in 1 direction perform better than the ISO sample, but under-performs in the 2 direction. This might be caused by the stress induced by the grips, which is supported by the observation of failure at the start of the gripping area in the ASTM 3039 XY[0] and ZY[0] directions. The ZY[0] ISO 527 samples exhibit a significantly better (increase of 5MPa) compared to the ASTM 3039 samples, this can be attributed to the same phenomenon as is described for the XY[0] direction. The XY[45] sample shows significantly higher ductile response in comparison with the YX[0]. Since the load is not fully perpendicular on the interface of the roads, the road is also loaded in tension, which explains the better response.

The results from the filament test show a response that is characteristic of thermoplastics, showing a quasi-linear elastic region followed by a yield point and softening, finishing in a perfect plastic plateau. This curve is characterized as a C curve in different standards [53, 90]. The filament inhibits less plasticity than would be expected [21]. Since

Again, replaced TechnicalUM citation

this filament has been stored in an unconditioned room, there is a large possibility of moisture uptake, which decreases the ductile properties of the filament [7]. This can explain the difference between the observed strain at break and the strain at break from the technical data sheet [66]. The filament has been tested on a relatively high strain rate to determine the stress strain curve, the technical datasheet provided by Ultimaker prescribed a strain rate of 50mm/min. Higher strain rates lead in general to a harder (higher UTS and lower elongation at break) response, since they limit the visco-elastic behaviour of the plastic. Following this method the results for the Young's modulus and yield point were close to the provided technical data sheet, for  $E, \sigma_y, \epsilon_y$  respectively 0.5%, 1.83% and 11.04% lower. The strain at break is much higher for the injection molded data, this might be due to the sample form of the injection molded sample and additionally due to the absorbed moisture by the ABS filament.

When importing these hardening curves in a FEM model one should take into account the limited visco-elastic behaviour.

## 5

### 5.4. CONCLUSION

Different methods were used to determine the properties of FFF parts in different directions. The results between methods differ, but can be attributed to the geometry and method of the test standard. No optimal method was found for testing the three principle directions. With the generated results, it can be concluded that there is significant anisotropy between directions. The 1 direction shows a ductile behaviour while the 2 and 3 directions a very brittle behaviour. Since it was concluded that the RVE shows large porosity, and the strength of the FFF is largely governed by the healing between roads, the probable mechanism of failure is crack initiation at stress concentrations where roads have sub-optimal healing. These phenomena are in line with the theory on polymer physics as is discussed in chapter 2. The validation and additional knowledge on the behaviour of FFF products is important in choosing the appropriate constitutive relations in the FEM model.

The RVE model discussed in the next chapters generates data assuming the roads behave as the filament material and full healing (perfect bonding between roads). This data could help identifying the best representative response from the different testing standards. The hardening curves extracted from the filament tests are close to the data mentioned by the specification sheet. Therefore, these can be useful as input curves for the FEM model. However, since filaments in use are relatively old (multiple months) and have not been stored in a controlled environment, these will likely give a more brittle response.

# 6

## ELASTIC MODELLING

This chapter discusses the different elastic modelling approaches and will present the results. The properties used in this analysis are based on the ABS blend specified in the the Ultimaker technical data sheet [66].

### 6.1. METHODS AND PROCEDURES

#### 6.1.1. RVE HOMOGENIZATION MODEL

The RVE homogenization model is a combination of a Matlab (version 2018b) code of multiple scripts and functions where parameters for the RVE are assigned and where the results of the FEA are processed to obtain the elastic properties. The Matlab code designs an RVE based on the line width and thickness of the road structure as can be seen in figure 4.11. Additionally, multiple RVE's can be stacked and the orientation of layers can be altered according to the composite notation. The resulting RVE is presented in chapter 4. The design is exported to Abaqus (version 2018), and is meshed with elements of a specific size. The finite element analysis includes an implicit model where the design is quasi-statically loaded with a 0.03 strain. Periodic boundary conditions are applied to the opposing faces of the RVE to simulate a larger solid, in figure 6.1 the RVE is defined with the different faces. When the properties of the 1 direction are determined, face 1 is loaded while face 3 is constrained. Periodic boundary conditions, simulating the stresses on the opposing faces, are applied. Face 6 is linked with 5, and face 4 is linked with 3. The internal stresses from the FEA in Abaqus are imported to Matlab and are used in the homogenization step according to equation 2.30. After this step the compliance matrix can be calculated and the elastic properties can be extracted. These properties are saved for the specific settings used to generate the RVE design. A convergence study was conducted to determine the appropriate mesh size of the RVE.

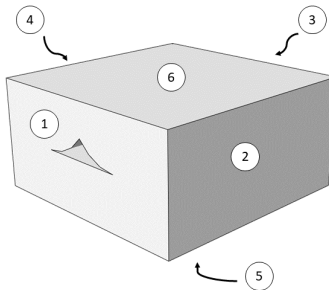


Figure 6.1: RVE with the defined faces where the load and periodic boundary conditions are applied

### 6.1.2. MESH

6

For this solid model a mesh of first order 3D hex-dominated elements was chosen and supplemented with wedge type triangular prisms. Hex-dominated elements are preferred for simple geometries since these are more accurate due to the degrees of freedom (8 nodes in 3 DOF). Additionally, tetrahedrons are prone to volumetric locking, generating an artificially stiff response. To apply periodic boundary conditions on the faces of the RVE, the seed of nodes should be identical on opposite faces. To achieve these requirements the RVE is divided in partitions as can be seen in figure 6.2.

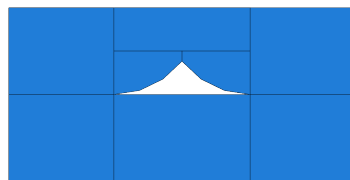


Figure 6.2: RVE with partitions to generate a evenly distributed hexahedral mesh

The results from the homogenization model seemed to be insensitive for mesh size, as they did not alter significantly for an element size smaller than 0.05mm (1/8 of the RVE width, which is quite a coarse mesh). The results also did not seem to alter with multiple RVEs used in the simulation. Since the homogenization simulations are not computationally intensive, a fine mesh with a global size of 0.01mm was chosen as is shown in figure 6.3.

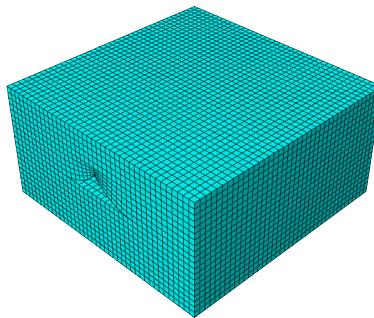


Figure 6.3: The meshed RVE

Table 6.1: Elastic properties of different methods in the 3 principal directions

direction	$E$ Voigt [MPa]	$E$ RVE [MPa]	$E$ ISO [MPa]	$E$ ASTM [MPa]
1 (YX[0])	1984	1972	2019	1811
2 (XY[0])	1643	1909	1974	1616
3 (ZY[0])	1233	1469	1793	1563

### 6.1.3. VOIGT MODEL

Additionally to the RVE homogenization model, the analytical predictions by the Voigt model is also used to compare the elastic properties for different orientations. The Voigt model is explained in chapter 2 (equation 2.24). The cavity in direction 2 and 3 is not constant and will therefore generate less accurate results. For this analysis, a cavity density is considered equal to the largest cavity surface in the corresponding direction. This will most likely under-predict the elastic properties due to decrease of the cavity along the cross section. Additionally, it should be noted that here also full healing (homogeneous bulk material) is considered, theoretically this should not influence the elastic properties, since the healing region that affect material properties is very thin and will likely only alter non-linear properties.

## 6.2. RESULTS

In figure 6.4 and table 6.1 the results are presented of for the FEA of the RVE and the analytical predictions as compared to the empirical data for the elastic properties. The models are plotted as a function of the line ratio, which is the line height divided by the line width. Empirical measurements were only made for samples with a line width of 0.4 mm and a line height of 0.2mm.

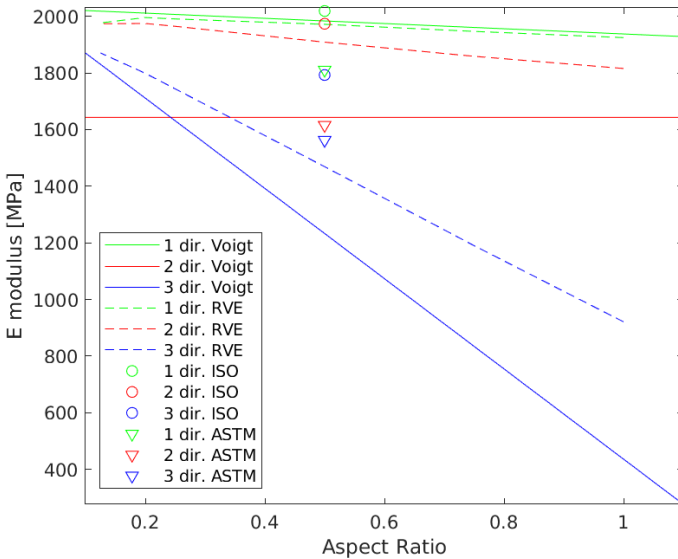


Figure 6.4: Elastic properties for different aspect ratios ( $l_h/l_w$ ) comparison between simulated RVE, experimental ISO 527 and ASTM D 3039 method, and according to the Voigt model.

6

### 6.3. DISCUSSION

#### EXPERIMENTAL ELASTICITY

The results in the previous section show the two approaches as a function of the aspect ratio including the results from experimental testing. In chapter 5 the effect of the sample shape on the properties is discussed. The ISO samples will probably over-estimate the elastic properties in the 2 and 3 direction due to extra wall layers that are implemented, this is in line with the observations of the models and the ASTM sample. The results from the ASTM sample should in theory give the most representative elastic response. However, since the large surface roughness and non-constant sample cross section, it can be difficult to exactly measure the cross sectional area. Additionally, since there is no perfect healing, there may be some localized damage (e.g. debonding) which would lead to a decrease in the  $E$  modulus. Surprisingly, the 1 and 2 empirically tested directions significantly under-perform compared with the results from the models. This might be due to inaccuracies in the measurements. Since the surface is very rough, the measured surface might be larger than the actual surface, generating low elasticity for the empirical results. Interestingly, the 3 direction in both empirical methods show a better performance compared with the models. This can probably be explained due to the large cavity area that is assumed in the 3 direction. This area would in reality be smaller, and would have blunted corners.

### VOIGT MODEL

The Voigt model makes some drastic simplifications in the 2 and 3 direction as is described in "Methods and procedures" of this chapter. Since the largest cavity fraction is assumed, the model will significantly under-predict the elastic properties.

### RVE MODEL

The FEA of the RVE still leads to a lower result compared with both the empirical tests. The RVE model is in general closest to the empirical results, for the 1 and 2 direction it is slightly lower than the ISO test, and higher than the ASTM test. For the three direction, it is lower than both tests for reasons mentioned before.

## 6.4. CONCLUSION

The models and empirical tests show subtle differences with respect to the each other. In general the ISO samples have the highest results due to the included wall layers. The Voigt and RVE model show similarities, but the RVE model has less problems with simplifications and shows more consistency with the empirical results. The ASTM samples show some complications in the 2 directions due to the large surface roughness in the 2 direction, which seems to have approximated the response obtained for the 2 and 3 directions. The varying empirical results display the demand for a good standard that produce consistent representative results. To correctly compare the models with the empirical tests, and the dependency on the line ratio, more experimental data should be gathered for different line ratios and a good measuring standard should be created for FFF products. Research question 4 in Chapter 3 can partly be answered on the elastic properties of of FFF products. The elastic properties differ significantly in the 2 and 3, especially for larger aspect ratios. There is still little relevant experimental data available to make a strong statement on the predictive power of the different models. These do however, indicate the stiffest directions accurately.



# 7

## NON-LINEAR MODELLING

This chapter consists of non-linear (beyond elasticity) modelling for the Finite Element Analysis with Abaqus including a user defined subroutine (VUMAT), where user defined constitutive behaviour is coded. Additionally other analytical models are proposed to make a prediction for the non-linear behaviour of FFF products.

### 7.1. METHODS AND PROCEDURES

#### 7.1.1. FINITE ELEMENT METHOD

The Finite Element Analysis was conducted in Abaqus in combination with a pre-written VUMAT according to the three papers proposed by Melro [58, 84, 91]. This code was originally created for long fibre reinforced composites, and has been adjusted to analyse FFF RVEs. The implicit FEM method has convergence issues when dealing with non-linear material behaviour, so an explicit method was used [92].

The main difference between explicit and implicit analysis is the dependency on time and increments. For static cases without plasticity the implicit method is often used, for dynamic cases including plasticity explicit method is used to determine the state of the material at every increment. Implicit simulations adopt a method called Euler integration scheme which ensures stability (unconditionally stable) and facilitates larger time steps. This method may be time consuming for dynamic loads. Explicit analyses aims to solve for acceleration. Using simplifications, the acceleration of a body can be found for every increment, and additionally, the velocity and displacement. This method is not unconditionally stable, and thus smaller time increments are required. This must be smaller than the Courant time step, which dictates the time taken by a sound wave to travel across an element. Explicit analysis offer a faster solution in events where there is a dynamic equilibrium. The stable time increment when simulating quasi-static conditions with explicit dynamic analyses can be artificially increased by scaling the mass

of the elements, allowing the stress wave to propagate faster. The downside of this is the increase of kinetic energy introduced in the system. A rule of thumb is to keep the kinetic energy at least below 10% of the total energy.

A VUMAT subroutine was used in combination with ABAQUS to implement non-linear constitutive models. A VUMAT is used if the Abaqus material model library does not represent the behaviour of the material appropriately, or if a user wants a more accurate response in a complex situation [93]. Considering the very limited commercial models available for polymers, an adjusted VUMAT was implemented to simulate this behaviour. The VUMAT is written in FORTRAN and makes use of inputs for material properties, and outputs Solution Dependant Variables, which can be displayed by the Abaqus interface. The VUMAT requires hardening curves as an input to determine the plastic behaviour of the material, these hardening curves need to be extracted from uniaxial tension and compression data. For this study the tensile experimental data is extracted from the filament tensile tests as is presented in chapter 5. The compressive curve is of less importance, since our simulations will be focused on uniaxial tensile loading cases. However, the yield function, as is presented in equation 2.7, is strongly dependent on the yield stress in compression, therefore an approximation for the hardening curve in compression is needed. Wang et al. [94] present an extensive study on the compressive behaviour of PC/ABS, one of the curves from this work is used as the compressive input curve.

Before implementing the hardening curve, the curve needs to be converted from normal uniaxial strain to plastic strain, with the following equation:

7

$$\epsilon_{1p} = \epsilon_{1t} - \epsilon_{1e} \quad (7.1)$$

where  $\epsilon_{1p}$  is the plastic strain,  $\epsilon_{1t}$  is the total strain and  $\epsilon_{1e}$  is the elastic strain, which follows the regular  $\sigma/E$  relation. The corresponding hardening curves are shown in figure 7.1, and are subtracted from the filament stress strain curves presented in chapter 5. This uniaxial plastic strain corresponds with the uniaxial equivalent plastic strain. The equivalent plastic strain is calculated in a similar way to the von Mises stress:

$$\bar{\epsilon} = \frac{2}{3} \sqrt{\frac{3(\epsilon_{11}^2 + \epsilon_{22}^2 + \epsilon_{33}^2 + \epsilon_{23}^2 + \epsilon_{13}^2 + \epsilon_{12}^2)}{2}} \quad (7.2)$$

where  $\bar{\epsilon}$  is the equivalent strain. The equivalent plastic strain against the equivalent stress can therefore be calculated, and will be used as the input hardening curve. The code will know when the "yield" point (in reality the anelastic point) is achieved, and will afterwards follow the equivalent (or von Mises) stress related to the equivalent plastic strain curve for a particular element.

The 0.2% offset is used to indicate the yield point that would be defined for metals. The "anelastic" point (the point where linear elasticity practically ends and where the hardening curve starts) is near this 0.2% offset point.

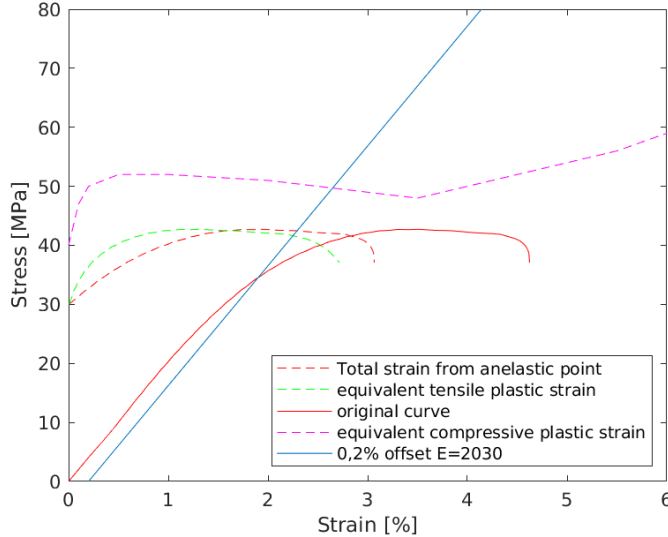


Figure 7.1: Implemented hardening curves for Ultimaker ABS

7

Similar to the elastic modelling code, MATLAB is used to provide the input parameters and geometric shape. For the explicit method no periodic boundary conditions are applied, this would require too much computational power to run. In return, a convergence study is carried out for multiple stacked RVEs next to a convergence study for mesh sensitivity.

The mesh is loaded in the different load-cases, uniaxial tension in the 1, 2 and 3 principal direction. The RVE is constrained on one face and loaded with a velocity boundary of  $(a/20)/s$  where  $a$  is the side length of the RVE that is parallel to the loading face. The RVE and its respective faces are seen in figure 6.1. This results in a strain rate of around 1 mm/min, which is in accordance with the test speed used for the experimental investigation in chapter 5.

When the appropriate ABAQUS input files are generated by the MATLAB code, and the VUMAT file is defined alongside with the corresponding harderning curves, the job is submitted through the unix shell to the kernel.

For testing the constitutive model defined in the VUMAT, a one element test was performed to asses the material response. The subroutines in VUMAT determines after every increment what the stress state is in the element, and what behaviour the element is coded to display. For the first region of the load, the element will behave elastically, up to the increment where the yield function defined by Tjoegl (equation 2.7) is surpassed. At this moment the element behaves plastically and will follow the implemented hardening curve through an integration algorithm, which is described in more detail in Melro's paper [58]. Additionally the subroutine checks if the strain based Johnson Cook

check this  
name

failure model is surpassed according to the defined Johnson Cook variation presented in equation 2.13. This criterion implements an uniaxial tension strain to determine an equivalent strain that needs to be met before the element starts to fail. After this moment the element is deleted and will not exhibit any stiffness.

In a larger model consisting of multiple elements, the geometry will create stress concentration points where elements will prematurely yield and fail. This will cause a crack to grow and finally will lead to fracture. The goal of the simulation is to determine the effect that the geometry has on the macroscopic response of the RVE, that is, the reaction force opposite from the load face. In a model consisting of multiple elements this subroutine is repeated for every element through every increment. This RVE has more than 300,000 elements and can go up to more than 300,000 increments, resulting in running the subroutine more than  $9 \cdot 10^{10}$  times. This requires extensive computational power, therefore the High Performance Computing cluster of the TU Delft is used to perform this explicit analysis. Using the capabilities of one of the nodes in this computer, the simulation for each loading case took more than 4 hours in general.

The goal of the FEM simulation is to predict the stress strain response in the 3 principal directions and to compare these with the empirical tests. Additionally, different aspect ratios of the RVE (as is discussed in chapter 4) can be simulated. But first a convergence study should be conducted to determine the accuracy of the simulations.

When the FEM simulation finished, an ODB file is generated including the requested field and history output of certain time intervals. This includes the different types of stresses and strains at the integration points as well as other output variables defined in the input file. The reaction forces are calculated at the nodes. The nodes at the constrained face will generate enough information to determine the stress strain response of a certain load according to the following equation:

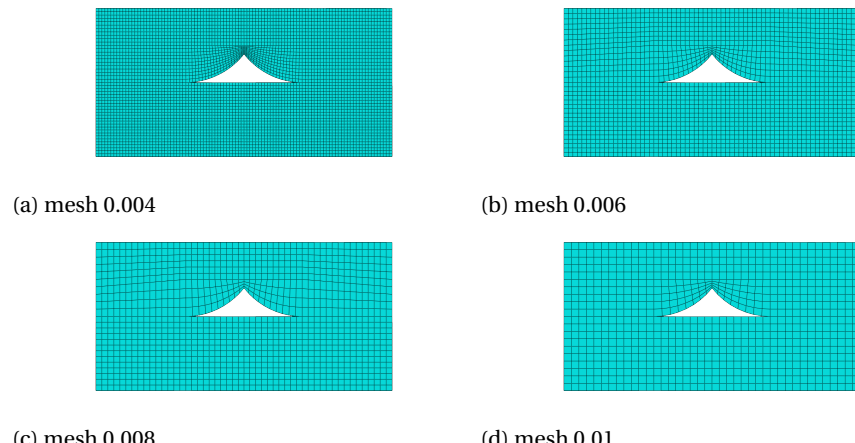
$$1/A_{face} \cdot \sum_{n=1}^{n_{face}} F_n = \sigma \quad (7.3)$$

where  $A_{face}$  is the surface of the constrained face,  $n_{face}$  are the nodes at the constrained face and  $F_n$  is the reaction force of a single node.

### 7.1.2. CONVERGENCE STUDY

To determine the mesh sensitivity a convergence study is conducted. The same meshing strategy, including the partitioning, was implemented as is presented in chapter 6. Element sizes of 0.004 0.006 0.008 and 0.01 mm are tested for the 3 directions for an aspect ratio of 0.5. The different forms of meshes are presented in figure 7.2. The results of these meshes are found in figure 7.5. However, these meshes did not seem to converge. Especially since the ratio between element size and porosity for the lower aspect ratios would only increase, resulting in a even larger difference. Additionally, the computational resources for the 0.004 mesh were already quite expensive, needing +30 hours CPU time for 1 simulation. Therefore, a different strategy was used. First, multiple CPU's

were used for the following simulations, 8 CPU's seemed the optimal amount for running Abaqus Explicit jobs. Secondly, mass scaling was applied to increase the Stable Time Increment. After some experimentation, mass scaling of 27.5 was applied to increase the Stable Time Increment of the smallest elements from  $2 \cdot 10^{-7}$  to  $1 \cdot 10^{-6}$ . Higher mass scaling introduces too much kinetic energy, which in turn generated stress waves in the stress strain curves, which is highly undesirable. Finally, the mesh strategy was adjusted. The goal was to still implement hexahedrals, due to their symmetry and favourable geometry, but to decrease the density in the area's without stress concentrations. The new strategy resulted in seeding the edges of the cavity with a fine mesh, while the rest of the RVE is meshed with a coarse 0.01 mesh as can be seen in figure 7.3. This mesh will be referred to as "optimized mesh", and reduced the number of elements with a factor 10 (from  $4 \cdot 10^6$  to  $4 \cdot 10^5$  elements). With these measures the computational time has been decreased with approximately factor 400. The current simulations are often finished in 8 hours.



7

Figure 7.2: Different element sizes implemented for convergence study.

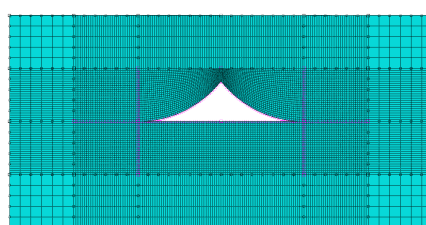


Figure 7.3: Optimized mesh with a fine node seed (0.002 indicated in purple) along the cavity and coarse (0.01) for the rest

Additionally, a convergence study is conducted for multiple connected RVEs. Four stacked RVEs in the XY and ZX planes are analyzed and additionally a block of  $2 \times 2 \times 2$  RVEs is

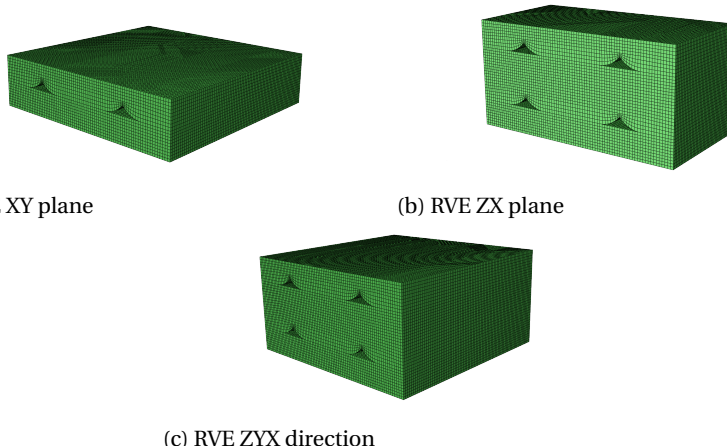


Figure 7.4: Different RVE duplicates implemented for convergence study.

simulated. The RVEs are produced with an aspect ratio of 0.5 and with an element size of 0.01, similar to the generation of the RVE for the elastic analysis. The RVE combinations can be seen in figure 7.4.

## 7

### 7.1.3. STRESS INTENSITY APPROACH

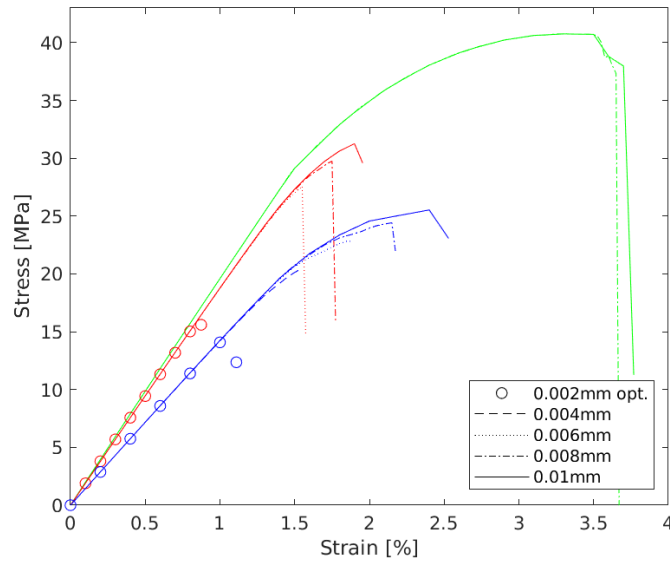
An additional approach was investigated with respect to the failure mechanism in the RVE. As is described in chapter 2, linear elastic fracture mechanics states that the critical failure stress can be predicted if the form and size of a crack is known. The equation for the stress intensity factor can be seen in equation 2.18. The periodic voids can be assumed as cracks for a plane strain loading condition in the 2 and 3 direction, which are dependent on the line thickness and width. With these parameters a critical stress ( $\sigma_c$ ) can be found which should give an approximation for the failure stress in FFF produced parts. For the fracture toughness of ABS, a  $K_{Ic}$  of  $4.32 \text{ MPa} \cdot \text{m}^{-3/2}$  was chosen, as is discussed in chapter 2.

Additionally, the cracktip plasticity theory, explained in chapter 2 (2.20) is used to predict the radius of the plastic deformation. This is useful to predict the plastic behaviour involved in the failure of parts. Products that show low plasticity in their fracture surface are suspected to have a low toughness at the fracture surface, resulting in brittle failure, which might be caused by improper bonding. To have a better understanding of the size of the cracktip plasticity, the radius of plasticity is plotted against the distance between the crack tip and the edge of the RVE.

## 7.2. RESULTS

### 7.2.1. CONVERGENCE STUDY MESH

The convergence study of the mesh for mesh sizes 0.004, 0.006, 0.008 and 0.01 with an RVE with aspect ration 0.5 is presented in figure 7.5. The 3 principal directions are presented consecutively in green, red and blue. For some mesh sizes the simulations were unsuccessfully (0.004 in 1 and 2 direction and 0.006 in 1 direction), the simulations in the 3 direction give a representative view on the mesh sensitivity. As can be seen, convergence is difficult to achieve due to the large stress concentrations at the tips of the cavity, the difference between 0.004 mm and 0.002 mm is still significant. It is however very difficult, and computationally expensive to decrease the mesh even further.



7

Figure 7.5: Convergence study for different mesh sizes

### 7.2.2. CONVERGENCE STUDY RVE's

The convergence study for the RVE duplicates (figure 7.4) are presented in figure 7.6. Here the ZYX RVE in the 1 principal direction failed, the other results give a good representation of the sensitivity of the multiple RVEs. As can be seen, the difference in response is minimal for different RVE stacks.

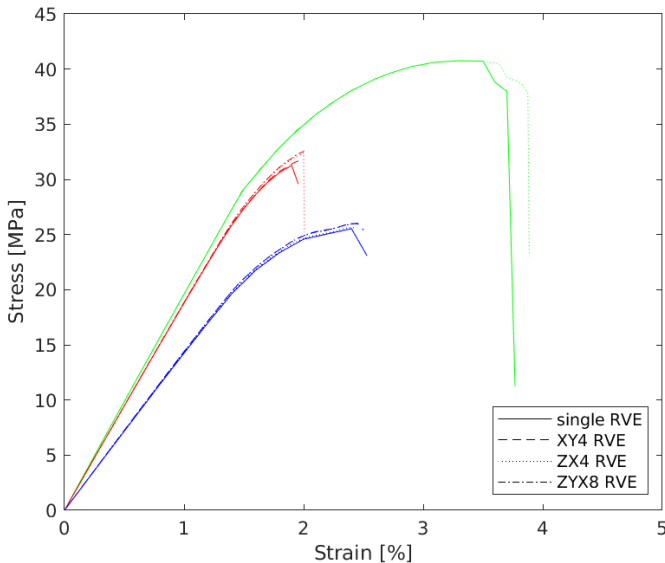


Figure 7.6: Convergence study for RVE duplicates. For understanding the nomenclature see figure 7.4.

## 7

### 7.2.3. SIMULATIONS COMPARED WITH EMPIRICAL RESULTS

In figure 7.7 the 0.5 aspect ratio simulation with the optimized mesh is compared with the empirical results from the  $0.4 \times 0.2$  ASTM 3039 tensile test samples presented in chapter 5. The results between the empirically measured and simulated RVE show significant overlap, with the 1 and 2 direction showing 10% difference in the UTS. Elongation at break is very accurately predicted for the 2 direction, with a difference of 6%, the 1 direction has a difference of 25%. The 3 direction is less accurate for the UTS and elongation at break, but the ASTM curve still overlaps the simulated RVE. This will further be explained in the discussion.

### 7.2.4. SIMULATIONS WITH ALTERING ASPECT RATIO

In the following figures (7.8,7.9,7.9) the dependency on the aspect ratio is shown for the optimized mesh. Aspect ratios of 0.125, 0.2, 0.25, 0.5, 0.75 and 1 are simulated for the 3 principal directions.

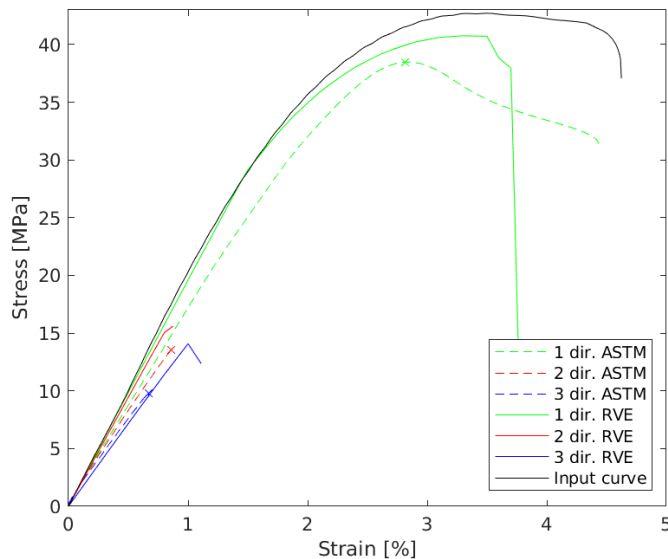


Figure 7.7: Comparison between the empirical obtained results and the simulated RVE in the 3 principal directions

7

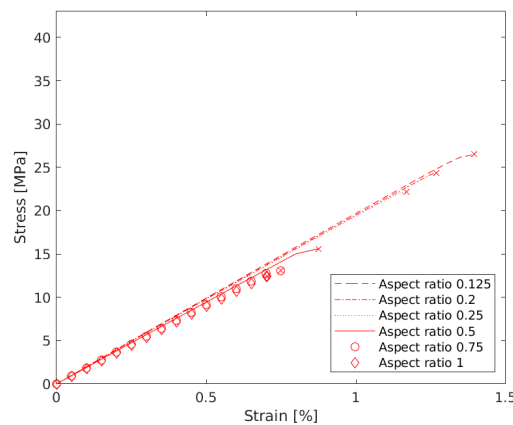


Figure 7.9: Comparison between different aspect ratios in the 2 direction

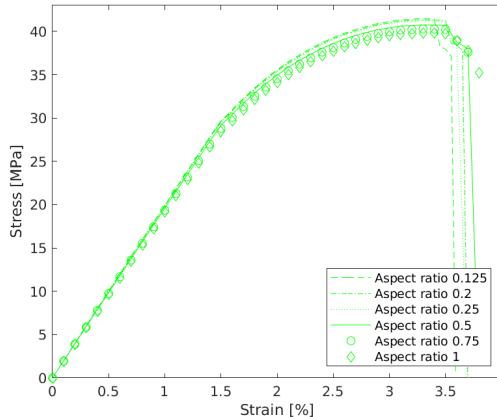


Figure 7.8: Comparison between different aspect ratios in the 1 direction

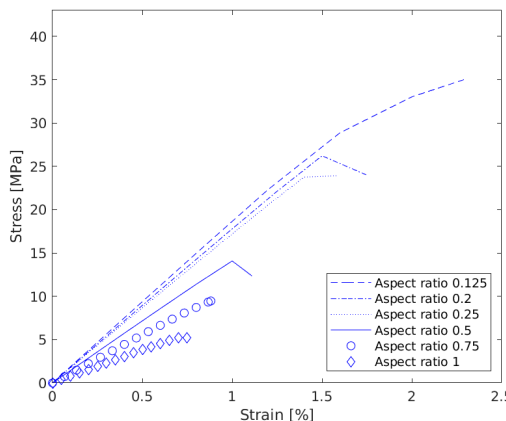


Figure 7.10: Comparison between different aspect ratios in the 3 direction

### 7.2.5. CONTOUR PLOTS

The following figures (7.11) will present the contour plots at the moment before failure of the Von Mises stress of the 3 principal directions for a 0.5 aspect ratio. These plots give a representation of the stress concentrations in the RVE. The 1 direction loaded RVE is shown in perspective since the stress distribution varies along the 1 direction, the stress distribution of the 2 and 3 loaded directions is constant. Appendix B will show additional plots, including different aspect ratios and crack propagation.

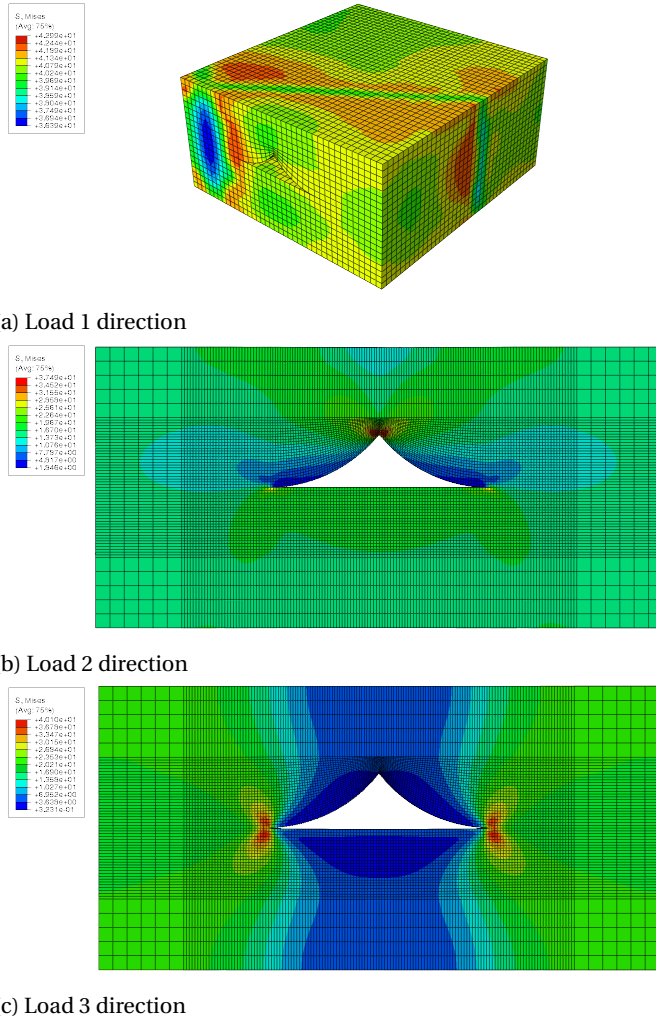


Figure 7.11: Contour plots of loading in the 3 principal directions with a 0.5 aspect ratio

### 7.2.6. COMPARISON FRACTURE STRESS

In figure 7.12 the plots (according to equation of critical stress in fracture mechanics 2.18 and the Voigt model 2.24) and simulated fracture stresses are presented and compared along different aspect ratios. The 1 direction is predicted with a plot of the Voigt model, while the 2 and the 3 directions are predicted with the plot of the critical stress equation. The Rule of mixtures overestimates the fractures stress with about 5%. When looking at the 2 and 3 directions, one can see the similarity of the inverse exponential behaviour between the plotted results from the equation and simulated data points.

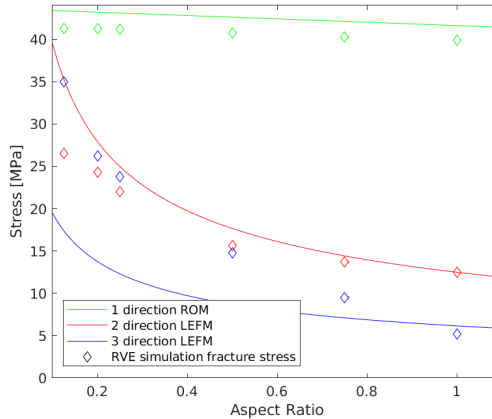


Figure 7.12: Comparison between fracture stress of the Stress Intensity approach and the RVE simulations for different aspect ratios

### 7.2.7. CRACKTIP PLASTICITY

In figure 7.13 the radius for cracktip plasticity is plotted and compared with the distance to the end of the RVE. This would in theory mean that the crack tip plasticity at the point of fracture will always be larger than the distance from the cavity to the end of the RVE, creating a fully plastic fracture.

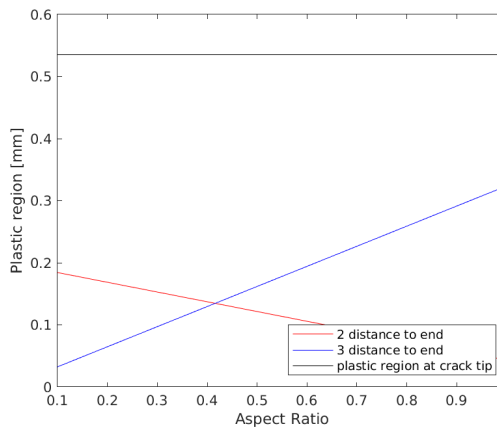


Figure 7.13: Crack tip plasticity radius for different aspect ratios compared with the distance to the end of the RVE

## 7.3. DISCUSSION

The mesh convergence study shows that the mesh is not fully converged, this means that it might be possible that the results will be altered even more. However, due to the computational expense of the simulations and the time constraints for writing this dissertation no further analyses were conducted. Yet, the current results are very close to the empirically obtained stress strain curves, therefore it is probable that this is a mesh close to the representation of reality.

The RVE convergence procedure was done with a 0.01 coarse mesh. This implies that there would be a possibility that the response for multiple RVEs could be altered for finer meshes. However, due to the limitations in computational power, this study should settle with the assumption that multiple RVEs would not lead to an alteration in results.

The comparison between the empirically obtained response using the ASTM D 3039 standard and the RVE simulations for 0.4 mm line width and 0.2 mm layer height who significant overlap in the behaviour of the FFF products. As is discussed in Methods and Procedures, the non-linear behaviour is rather difficult to predict for thermoplastics, however the implemented yield and failure criterion does seem to achieve a reasonable prediction in the 1 direction. The input curve could be optimized to achieve a more overlapping response. As is mentioned in chapter 5 the input curve was obtained from a relatively old filament, which is suspected to have degraded due to UV light and water absorption, resulting in a more brittle response in comparison with the fresh filament that was used for the ASTM D 3039 test samples. The 2 and 3 direction show significant overlap in its behaviour.

The 2 direction almost perfectly predicts the UTS, the difference between the simulated RVE and the empirical test can be accounted to a difference in mesostructure, a sub optimal healing or measurements defects (in chapter 4 it was discussed that the dimensional accuracy of FFF parts are limited, and accurate calculations for the surface might be troublesome). The difference in elasticity might be produced by this phenomenon. To more accurately determine the mechanical properties through experimental test, more data needs to be generated with an optimized testing method.

Direction 3 predicts the the elasticity relatively well, but has a lower UTS. This is may be attributed to the decrease in healing, as is concluded in chapter 4. Additionally, in the work of van Veen [27], PETG experimental tests with envelope temperatures close to  $T_g$  and room temperature were conducted with ZX[0] samples. These stress strain curves showed the same brittle behaviour and showed a UTS of roughly 26% of bulk UTS for  $T_g - 55$  (room temperature) and 36% for  $T_g - 15$ , which means an increase of 10% in relative bulk UTS for an almost fully healed part. For the experimental data generated for ABS, the UTS went from 23% of the UTS for a tensile test at room temperature, to a 34% relative UTS for simulated fully healed material. This may very well explain the difference between the sub-optimally healed experimental test, and the fully healed simulated RVE (which assumes bulk properties). However, this theory should still be strengthened by additional empirical tests for different temperatures and additional test for the aspect ratios in the 3 direction, both empirically tested and simulated.

In chapter 5 it was discussed what testing method would generate a most realistic response. The results from the RVE simulations clearly indicates that the ASTM D 3039 standard has a far better correlation, the reasons behind this are discussed in chapter 5.

As can be seen in figure 7.8, the response in the 1 direction does not change significantly for different aspect ratios, this is due to the fact that the surface fraction slightly decreases with an increasing surface fraction, this can be seen figure 6.4 and is discussed in chapter 4. The response in the 2 and 3 directions are significantly different due to the difference in surface fraction in the respective directions. As is expected from the theory, and discussed in chapter 6, the elastic moduli in the 2 direction does not change drastically. However, according to fracture mechanics, the critical stress scales exponentially instead of linearly as in elasticity, therefore the stress at fracture significantly decreases with a larger aspect ratio. In the 3 direction, the surface fraction does change by a large factor (from 0.9 to 0.21 for respectively an aspect ratio of 0.125 and 1), therefore both elastic modulus and fracture stress will drastically change. The smallest aspect ratio (0.125) even shows a ductile response, meaning the porosity might be small enough to decrease the stress concentrations at the tips. Also, a finer mesh might result in a different response as was discussed before. According to the simulated results, a smaller aspect ratio will result in better and more isotropic properties in all directions, which is in line with the results generated in the literature. The issue is that the printing time will scale inversely proportionally with an increase in aspect ratio, therefore a trade-off should be applied, for engineering applications, an aspect ratio of 0.25 often seems reasonable.

## 7

The prediction of the UTS in the one direction is in reality trivial, one can simply use the Voigt equation 2.24 when the mesostructure is known to obtain a good prediction. The 2 and 3 directions show significant overlap with fracture mechanics theory. These results also shows overlap with experiments from [31] shown in figure 2.13, however these experiments were conducted with different process parameters and can therefore not be directly compared. The slope of the curve in figure 7.12 (which is governed by the exponent operator), and the magnification (which is governed by an empirically determined factor) could be altered to produce a fitted equation, but before implementing this, a more extensive mesh convergence study needs to be performed. This is however not part of this thesis, it is sufficient to conclude that a significant overlap between linear elastic fracture mechanics exist in order to predict the fracture behaviour of FFF parts since the porosity can behave like microcracks.

The contour plots show the stress concentrations at the crack tips for the 2 and 3 directions. These stress concentrations have the same form as is predicted in plane strain fracture mechanics (figure 2.42), which indicates the relevance for the application of fracture mechanics theory. In the contour plots for the 1 direction, shear bands are observed for the strain contour plots. This is due to the yield criterion (equation 2.8), which dictates a yield loci that will deform first plastically in shear. Due to the applied positive Poisson ratio a certain shear stress will develop once the material is loaded in tension, therefore the material will develop larger strains due to these shear bands, and will finally fail in this region due to the strain based failure criterion 2.13. This is in line with

polymer science as is discussed in chapter 2, where polymers loaded in tensile will form shear bands and will finally fail due to the maximum strain of a polymer molecule. The contour plots additionally show the formation of a crack, which in most cases is perpendicular to the loading face, starting at the cavity tip.

Finally, the prediction of the crack tip plasticity indicates that a fully healed FFF product will exhibit plasticity at the crack surface. This is in line with the empirical observations of tested samples produced at high envelope temperature (showing whitened regions, indicating shear bands or crazing), while samples produced at room temperature did not show any whitening, indicating sub optimal healing. This might serve as a visual inspection method to confirm full healing was achieved.

## 7.4. CONCLUSION

After the mesh convergence study and optimization of the FEM analysis, a result was generated for a 0.5 aspect ratio that shows significant overlap with the experimental tests from the ASTM D 3039 standard. The 1 and 2 direction show a variation of less than 5% percent in the determination of the UTS, the elongation is more difficult to determine since polymers have a complex strain (rate) dependency. Nonetheless, the strain at break is also predicted inside an acceptable margin (since the standard deviation of empirical results in strain is also significant). The 3 direction from the simulated RVE shows a difference in UTS compared to the empirical results due to the worse bonding between layers, this is exactly in line with the healing theory explained in literature. However, this effect seems to be significantly less pronounced than first was assumed. According to the obtained results in this thesis, for ABS specimen printed at room temperature, the porosity has a major influence compared to sub-optimal healing. The healing effect in the 2 direction is minimal (less than 5% decrease of the original UTS), since the toolhead quickly reaches the same spot before cooling. This will obviously differ for different geometries and speeds. In the 3 direction, the healing effect would be most significant, and is responsible for roughly 10% of the decrease in mechanical properties. This therefore means that, with these process parameters, porosity is by far the dominant influencer of mechanical properties, responsible for more than 90% of the decrease in every direction. This decrease in mechanical properties is most present in the 2 and 3 direction, where the UTS decreases with more than 65%, additionally the E modulus is decreased with as much as 30%.

7

Linear Elastic Fracture mechanics shows significant resemblance with the results derived from the RVE simulations. Further research into the porosity for different aspect ratios might give more tools to predict the fracture behaviour with analytical approaches.

As is expected from literature, the decrease in aspect ratio significantly increases the mechanical properties of FFF products, due to the reduced porosity. However, this comes at a cost of increased printing time. To also validate the RVE model for the aspect ratios used, empirical tests should be performed with the same aspect ratios. If these also seem to provide corresponding results, different combinations of RVEs could be simulated to replicate layer orientations and hopefully determine the best layer build up.

Finally, different materials could be used in this model. The same procedure to determine the hardening curve should be applied as is explained in chapter 5. Carbon fibres could help increase the fracture toughness, as they are stiffer and stronger which would lead to an obstruction of cracks that would propagate through the sample.

# 8

## CONCLUSION AND RECOMMENDATIONS

### 8.1. CONCLUSION

#### 8.1.1. IDENTIFICATION OF PROCESS PARAMETERS INFLUENCING THE MECHANICAL PROPERTIES (RESEARCH QUESTION 1)

The drop in mechanical properties is, according to literature, accredited to the inherent porosity that is induced during the process and the sub-optimal healing between roads.

##### POROSITY

The porosity is influenced by the temperature dependant viscosity of the filament, printing strategy, accuracy, quality of the system and most importantly, the aspect ratio, layer height over line width ( $l_h/l_w$ ).

##### HEALING

Healing is influenced by the filament properties glass transition temperature ( $T_g$ ) repetition time ( $t_{rep}$ ) and entanglement density ( $\nu_e$ ). The temperature history defines the degree of bonding between adjacent roads. This effect is more articulated in the  $z$  direction, due to the larger time period that the toolhead needs to reach the subsequent point in the next layer, giving the lower road sufficient time to cool down.

##### INTERROAD STRENGTH

Due to these two phenomena, the interroad strength is drastically reduced, resulting in a brittle failure when loaded. This effect can be reduced to some degree by alternating

layer directions in a composite like lamina to distribute the weak links and to achieve more isotropy. Quantifying the effects and optimizing the mechanical properties has only been achieved to a limited extent in current literature.

## ELASTICITY

According to theory, only the mesostructure should significantly alter the elastic properties of the FFF products. When the elastic properties are measured with the RVE homogenization approach, a prediction of the elastic properties with an accuracy of approximately 10% can be made compared to the empirical results. The largest uncertainty for validation this prediction is related to the difficulties regarding the dimensional accuracy of the sample.

### 8.1.2. MESOSTRUCTURE (RESEARCH QUESTION 2)

The mesostructure was constructed with the assumption of two overlapping stadium shaped roads, generating a triangular periodic cavity. The size and geometry of this cavity seemed to be dependent of the aspect ratio and could be defined through a geometric model. An experimentally-validated finite element analysis of Representative Volume Elements of the mesostructure confirmed this dependence. Not only does this model match the observed mesostructure, but also the results from the FEA indicate a very strong overlap with the empirical results from the ASTM D 3039 testing method (deviation of less than 5% of the UTS between the fractions relative to bulk material in the relevant directions).

### 8.1.3. EXPERIMENTAL TESTING (RESEARCH QUESTION 3)

#### ASTM D 3039 AND ISO 527 TESTING

Stress concentrations and crack initiation points give an unexpected and inconsistent response of the tested samples. The large surface roughness and limited dimensional accuracy make it difficult to accurately measure the cross sectional area. Between the two tested methods, the ASTM D 3039 seemed to exhibit most representative behaviour, due to the possibility of capturing the true behaviour of the weakened bonds and the effect of the porosity. This statement is strongly supported by the results from the FEA, and the comparison between the responses of the ASTM D 3039 and ISO 527 standards.

#### FILAMENT TESTING

Filament testing results seemed indicative of the bulk properties of the ABS filament and showed the same behaviour as injection moulded counterparts as well as filaments tested with appropriate clamps from the literature. Therefore, the results were accepted with this provisional method and introduced into the RVE model as hardening curves.

### 8.1.4. DOMINANT PHENOMENON OF THE DECREASE IN MECHANICAL PROPERTIES (RESEARCH QUESTION 4)

With the RVE simulation, the properties of FFF products with fully healed interfaces were simulated since bulk material properties were assumed in the generation of the RVE. This makes it more difficult to compare and validate correctly with the sub-optimally healed samples used for the experimental testing. This limitation introduces a significant uncertainty when comparing it with the empirical results.

#### DROP IN MECHANICAL PROPERTIES IN THE 3 PRINCIPAL DIRECTIONS

The results indicate that the simulated directions 1 and 2 have overestimated the UTS for less than 12% with respect of the ASTM standard. The simulated direction 3 however, has a much higher UTS (43%) than the experimentally obtained 3 direction. This might be related to the decrease in healing in the  $z$  direction.

Therefore, for the parameters used at room temperature and assuming sub-optimal healing for the direction 1, the drop in UTS is explained by the porosity and accounts for a drop of 10% with respect to the bulk properties. The direction 2 experiences a drop in UTS of approximately 70% and is largely accounted by the porosity as well. However, direction 3 experiences the most significant drop; 77%, from which 10% is responsible for the healing. This effect could be simulated by adding cohesive elements that simulate a weaker interface between roads. This was not explored in this thesis.

Nevertheless, considering these process parameters, decreasing the porosity is predicted to have more potential of increasing the mechanical properties than increasing the healing between roads.

#### ASPECT RATIO

Before being able to conclude that the RVE model is also validated for different aspect ratios (up to this point only the results of aspect ratio 0.5 are discussed), more experimental data needs to be gathered on the different aspect ratios. Still, for the 0.5 aspect ratio the research question 4 has been properly addressed.

8

### 8.1.5. CONSTITUTIVE MODELLING OF THERMOPLASTIC AMORPHOUS POLYMERS (RESEARCH QUESTION 5)

Amorphous thermoplastic polymers have complex nonlinear behaviour. However, the models considered herein have been able to satisfactorily predict it. A stress based yield criterion implemented for epoxies combined with a strain based failure criterion (Johnson-Cook variation) provided satisfactory results for temperature independent, quasi-static loading. Note that despite thermoplastics and epoxies having different molecular structures (e.g. cross links for epoxy), the continuum models seem to appropriately capture both their behaviors. The implemented hardening curve from the filament represented the polymer behaviour in tension (for a strain lower than 5%) to a satisfactory degree.

Damage evolution was disregarded, as it seemed only significant in thermoplastics at higher strains.

### 8.1.6. ADDITIONAL THEORY FOR THE PREDICTION OF MECHANICAL BEHAVIOUR OF FFF PARTS (RESEARCH QUESTION 6)

The Rule of Mixtures has been applied in chapter 6 with the Voigt model in the 1 direction, which predicts the elasticity and fracture stress with a error margin of about 10%. The Reuss model was applied in the 2 and 3 direction, but it is not accurate due to the inconsistent cross section. Additionally, Linear Elastic Fracture Mechanics (LEFM) has been applied to predict the fracture stress of different aspect ratios. The cavity has been simplified as a crack in LEFM, and the general trend (qualitatively) agreed with the high-fidelity finite element analyses of the RVEs, although LEFM could not be used for quantitative predictions.

## 8.2. RECOMMENDATIONS

- Simulated RVE results are generated for different aspect ratios, these simulations should be validated with empirical tests of the respective aspect ratios (besides 0.5)).
- The simulated RVE results give a representation of fully healed polymers, respective empirical tests should be conducted with fully healed samples. Conversely, if the samples are not fully healed, then the cohesive behavior between roads needs to be characterized and appropriately modeled by cohesive elements.
- The effect of adequate hardware, microtome and filament clamps, should be compared with the methods and results used in this thesis.
- Different lay-up of layers and orientations should be considered to find the best combination that improves the mechanical behaviour for a given application.
- Damage could be implemented based on the craze criterion presented in this thesis.

# REFERENCES

- [1] Wohlers Associates, *Wohlers Report 2017 3D Printing and Additive Manufacturing State of the Industry*, Tech. Rep. (2017).
- [2] M. Bastiaans, I. Blankers, P. V. Scheepstal, and R. Veraar, *De impact van 3D-printen op Defensie*, (2015).
- [3] NATO, *Perspectives on the Use of Additive Manufacturing in NATO Operations*, Tech. Rep.
- [4] J. Joyce, M. J. Louis, and T. Seymour, *Deloitte University Press*, Tech. Rep. (2014).
- [5] M. Kamran and A. Saxena, *A Comprehensive Study on 3D Printing Technology*, *MIT International Journal of Mechanical Engineering* **6**, 63 (2016).
- [6] Ultimaker, *Ultimaker S5 Specification sheet*, (2019).
- [7] B. N. Turner, R. Strong, and S. A. Gold, *A review of melt extrusion additive manufacturing processes : I. Process design and modeling*, **3**, 192 (2014).
- [8] C. McIlroy and P. D. Olmsted, *Disentanglement effects on welding behaviour of polymer melts during the fused-filament-fabrication method for additive manufacturing*, *Polymer* **123**, 376 (2017).
- [9] TNO, *Procesbegeleiding productie d.m.v. 3D-printen: Lessons learned*, (2017).
- [10] A. Bellini and S. Güceri, *Mechanical characterization of parts fabricated using fused deposition modeling*, *Rapid Prototyping Journal* **9**, 252 (2003).
- [11] C. McIlroy and P. D. Olmsted, *Deformation of an amorphous polymer during the fused-filament-fabrication method for additive manufacturing*, *Journal of Rheology* **61**, 379 (2017).
- [12] J. P. Thomas and J. F. Rodriguez, *Modeling the Fracture Strength Between Fused-Deposition Extruded Roads*, *Solid Freeform Fabrication Proceedings* , 17 (2000).
- [13] C. Bellehumeur, L. Li, Q. Sun, and P. Gu, *Modeling of bond formation between polymer filaments in the fused deposition modeling process*, *Journal of Manufacturing Processes* **6**, 170 (2004).
- [14] Q. Sun, G. M. Rizvi, C. T. Bellehumeur, and P. Gu, *Effect of processing conditions on the bonding quality of FDM polymer filaments*, *Rapid Prototyping Journal* (2008), [10.1108/13552540810862028](https://doi.org/10.1108/13552540810862028).

- [15] J. E. Seppala, S. Hoon Han, K. E. Hillgartner, C. S. Davis, and K. B. Migler, *Weld formation during material extrusion additive manufacturing*, *Soft Matter* **13**, 6761 (2017).
- [16] Xstream, *Digimat-AM*, .
- [17] R. P. Wool, *Strength of Polymer Interfaces*, .
- [18] M. Somireddy and A. Czekanski, *Mechanical Characterization of Additively Manufactured Parts by FE Modeling of Mesostructure*, *Journal of Manufacturing and Materials Processing* **1**, 18 (2017).
- [19] M. Somireddy, A. Czekanski, and C. V. Singh, *Development of constitutive material model of 3D printed structure via FDM*, *Materials Today Communications* **15**, 143 (2018).
- [20] L. Li, Q. Sun, C. Bellehumeur, and P. Gu, *Composite modeling and analysis for fabrication of FDM prototypes with locally controlled properties*, *Journal of Manufacturing Processes* **4**, 129 (2002).
- [21] J. F. Rodríguez, J. P. Thomas, and J. E. Renaud, *Mechanical behavior of acrylonitrile butadiene styrene (ABS) fused deposition materials. Experimental investigation*, *Rapid Prototyping Journal* **7**, 148 (2001).
- [22] J. F. Rodríguez, J. P. Thomas, and J. E. Renaud, *Mechanical behavior of acrylonitrile butadiene styrene fused deposition materials modeling*, *Rapid Prototyping Journal* **9**, 219 (2003).
- [23] L. G. Blok, M. L. Longana, H. Yu, and B. K. Woods, *An investigation into 3D printing offibre reinforced thermoplastic composites*, *Additive Manufacturing* **22**, 176 (2018).
- [24] K. R. Hart, R. M. Dunn, J. M. Sietins, C. M. Hofmeister Mock, M. E. Mackay, and E. D. Wetzel, *Increased fracture toughness of additively manufactured amorphous thermoplastics via thermal annealing*, *Polymer* **144**, 192 (2018).
- [25] J. Bartolai, T. W. Simpson, and R. Xie, *Predicting Strength of Thermoplastic Polymer Parts Produced Using Additive Manufacturing*, in *Solid Freeform Fabrication 2016: Proceedings of the 26th Annual International* (2016) pp. 951–963.
- [26] A. M. Peterson, *Review of acrylonitrile butadiene styrene in fused filament fabrication: A plastics engineering-focused perspective*, *Additive Manufacturing* **27**, 363 (2019).
- [27] D. v. Veen, *Enhancing the mechanical properties of fused filament fabricated parts by elevating the print room temperature*, Ph.D. thesis (2019).
- [28] 3D Hubs, *introduction FFF 3d printing*, .
- [29] all3dp, *all3dp*, [Https://all3dp.com/](https://all3dp.com/).
- [30] Simplefy3D, *Print Quality Troubleshooting Guide*, .

- [31] H. Li, T. Wang, J. Sun, and Z. Yu, *The effect of process parameters in fused deposition modelling on bonding degree and mechanical properties*, *Rapid Prototyping Journal* **24**, 80 (2017).
- [32] S. H. Ahn, M. Montero, D. Odell, S. Roundy, and P. K. Wright, *Anisotropic material properties of fused deposition modeling ABS*, *Rapid Prototyping Journal* **8**, 248 (2002).
- [33] O. A. Mohamed, S. H. Masood, J. L. Bhowmik, M. Nikzad, and J. Azadmanjiri, *Effect of Process Parameters on Dynamic Mechanical Performance of FDM PC/ABS Printed Parts Through Design of Experiment*, *Journal of Materials Engineering and Performance* (2016), [10.1007/s11665-016-2157-6](https://doi.org/10.1007/s11665-016-2157-6).
- [34] V. E. Kuznetsov, A. N. Solonin, O. D. Urzhumtsev, R. Schilling, and A. G. Tavitov, *Strength of PLA components fabricated with fused deposition technology using a desktop 3D printer as a function of geometrical parameters of the process*, *Polymers* **10** (2018), [10.3390/polym10030313](https://doi.org/10.3390/polym10030313).
- [35] Gary Hodgson, *Slic3r Manual – Flow Math*, .
- [36] E. Cuan-Urquiza, E. Barocio, V. Tejada-Ortigoza, R. Pipes, C. Rodriguez, and A. Roman-Flores, *Characterization of the Mechanical Properties of FFF Structures and Materials: A Review on the Experimental, Computational and Theoretical Approaches*, *Materials* **12**, 895 (2019).
- [37] M. Montero, S. Roundy, and D. Odell, *Material characterization of fused deposition modeling (FDM) ABS by designed experiments*, *Proceedings of Rapid Prototyping and Manufacturing Conference*, 1 (2001).
- [38] M. Dawoud, I. Taha, and S. J. Ebeid, *Mechanical behaviour of ABS: An experimental study using FDM and injection moulding techniques*, *Journal of Manufacturing Processes* **21**, 39 (2016).
- [39] A. W. Gebisa and H. G. Lemu, *Investigating effects of Fused-deposition modeling (FDM) processing parameters on flexural properties of ULTEM 9085 using designed experiment*, *Materials* **11** (2018), [10.3390/ma11040500](https://doi.org/10.3390/ma11040500).
- [40] M. S. Hossain, J. Ramos, D. Espalin, M. Perez, R. Wicker, and W. M. Keck, *Improving Tensile Mechanical Properties of FDM-Manufactured Specimens via Modifying Build Parameters*, Tech. Rep.
- [41] H. S. Patanwala, D. Hong, S. R. Vora, B. Bognet, and A. W. Ma, *The microstructure and mechanical properties of 3D printed carbon nanotube-polylactic acid composites*, *Polymer Composites* **39**, E1060 (2018).
- [42] Ultimaker, *Speed*, .
- [43] Daniel, *Engineering Mechanics of Composite Materials* (Oxford university press, Oxford, 2006) pp. 1–157.

- [44] A. Rodríguez-Panes, J. Claver, and A. Camacho, *The Influence of Manufacturing Parameters on the Mechanical Behaviour of PLA and ABS Pieces Manufactured by FDM: A Comparative Analysis*, *Materials* **11**, 1333 (2018).
- [45] K. Balani, V. Verma, A. Agarwal, and R. Narayan, *Physical, Thermal, and Mechanical Properties of Polymers*, *Biosurfaces* , 329 (2015).
- [46] A. Van\_der\_Vegt, *DUP Blue Print* (2001).
- [47] J. L. Halary, *Wiley* (2011).
- [48] Ptoline, *Polymers, Injection molding of amorphous and crystalline* , .
- [49] D. Popescu, A. Zapciu, C. Amza, F. Baciu, and R. Marinescu, *FDM process parameters influence over the mechanical properties of polymer specimens: A review*, *Polymer Testing* **69**, 157 (2018).
- [50] O. A. Mohamed, S. H. Masood, and J. L. Bhowmik, *Optimization of fused deposition modeling process parameters: a review of current research and future prospects*, *Advances in Manufacturing* **3**, 42 (2015).
- [51] Granta Design Limited, *CES edupack*, (2018).
- [52] P. Appelsved, *Investigation of Mechanical Properties of Thermoplastics with Implementations of LS-DYNA Material Models*, Degree project in Solid Mechanics , 48 (2012).
- [53] T. N. O. Afd and R. I. S. A. Wullms, *NEN-EN-ISO 527-2*, (2016).
- [54] R. Christensen, *The Thoery of Materials failure*, , 298 (2013).
- [55] R. Janssen, I. Blankers, E. Moolenburgh, and B. Posthumus, *Tno: The impact of 3-d printing on supply chain management*, The Hague, Netherlands: TNO (2014).
- [56] S. Lin, Y. Xia, C. H. Lin, J. Wang, and G. Gu, *Stress state dependent failure loci of a talc-filled polypropylene material under static loading and dynamic loading*, 13th International Conference on Fracture 2013, ICF 2013 **2**, 865 (2013).
- [57] H. G. H. V. Melick, *Deformation and failure of polymer glasses*, *Ph.D. thesis*, Technische Universiteit Eindhoven (2002).
- [58] A. R. Melro, P. P. Camanho, F. M. Andrade Pires, and S. T. Pinho, *Micromechanical analysis of polymer composites reinforced by unidirectional fibres: Part I-Constitutive modelling*, *International Journal of Solids and Structures* **50**, 1897 (2013).
- [59] P. A. Du Bois, S. Kolling, A. Haufe, and M. Feucht, *A semianalytical model for the simulation of polymers*, Proceedings of the 2006 Korea LS-DYNA Conference, Seoul, Korea, published by Korean Simulation Technologies, KOSTECH **1**, 1 (2006).
- [60] ABAQUS, *Material Damage and Failure*, ABAQUS , 1 (2006).

- [61] P. a. D. Bois, S. Kolling, M. Feucht, and a. Haufe, *A COMPARATIVE REVIEW OF DAMAGE AND FAILURE MODELS AND A TABULATED GENERALIZATION AUTHORS : ABSTRACT : Keywords* ; , 75.
- [62] M. Gao, R. Krishnamurthy, S. Tandon, and U. Arumugam, *Critical strain based ductile damage criterion and its application to mechanical damage in pipelines*, 13th International Conference on Fracture 2013, ICF 2013 **5**, 3723 (2013).
- [63] G. Gu, Y. Xia, C. H. Lin, S. Lin, Y. Meng, and Q. Zhou, *Experimental study on characterizing damage behavior of thermoplastics*, *Materials and Design* (2013), [10.1016/j.matdes.2012.07.062](https://doi.org/10.1016/j.matdes.2012.07.062).
- [64] P. Mallick, *Fiber-Reinforced Composites* (2007).
- [65] A. E. Oskui, N. Choupani, and E. Haddadi, *Experimental and numerical investigation of fracture of ABS polymeric material for different sample's thickness using a new loading device*, *Polymer Engineering & Science* **54**, 2086 (2014).
- [66] Ultimaker, *Technical data sheet ABS*, Tech. Rep. (2018).
- [67] N. G. Tanikella, B. Wittbrodt, and J. M. Pearce, *Tensile strength of commercial polymer materials for fused filament fabrication 3D printing*, *Additive Manufacturing* **15**, 40 (2017).
- [68] A. M. Forster, *NIST Materials Testing Standards for Additive Manufacturing of Polymer Materials : state of the Art and Standars Applicability*, **1**, 9 (2015).
- [69] P. Materials and E. I. Materials, *ASTM D638 Standard Test Method for Tensile Properties of Plastics 1 D638-14*, , 1 (2015).
- [70] G. Alaimo, S. Marconi, L. Costato, and F. Auricchio, *Influence of meso-structure and chemical composition on FDM 3D-printed parts*, *Composites Part B: Engineering* **113**, 371 (2017).
- [71] M. Bertoldi, M. a. Yardimci, C. M. Pistor, S. I. Guceri, and G. Sala, *Mechanical characterization of parts processed via fused deposition*, Solid Freeform Fabrication Proceedings , 557 (1998).
- [72] T. N. O. Afd and R. I. S. A. Wullms, *NEN-EN-ISO 179-1*, (2014).
- [73] ASTM International and ISO, *ISO / ASTM Additive manufacturing 52900 — General principles — Requirements for purchased AM parts*, **2016** (2017).
- [74] *NEN-EN-ISO / ASTM 52901 General principles - Requirements for purchased AM parts*, (2019).
- [75] NEN-EN-ISO, *NEN-EN-ISO 17296-3 3D-printen - Algemene beginselen - Deel 3: Belangrijkste eigenschappen en bijbehorende testmethoden*, **3** (2019).
- [76] *ASTM F2971 Standard Practice for Reporting Data for Test Specimens Prepared by Additive Manufacturing*, *ASTM Standards* **i**, 3 (2013).

- 8
- [77] C. K. Chua, Chee How Wong, and Way Yee Yeong, *Standard, Quality Control, and Measurements Sciences in 3D printing and Additive Manufacturing* (Matthew Deans).
  - [78] Essentium, *Technical Data Sheet High Performance PLA*, Tech. Rep.
  - [79] A. Garg and A. Bhattacharya, *An insight to the failure of FDM parts under tensile loading: finite element analysis and experimental study*, *International Journal of Mechanical Sciences* **120**, 225 (2017).
  - [80] J. F Rodriguez, J. P. Thomas, and J. E. Renaud, *Design of Fused-Deposition ABS Components for Stiffness and Strength*, *Journal of Mechanical Design* **125**, 545 (2003).
  - [81] M. Somireddy, D. A. D. Moraes, and A. Czekanski, *Flexural Behavior of Fdm Parts: Experimental, Analytical and Numerical Study*, Solid Freeform Fabrication Symposium , 992 (2017).
  - [82] C. Casavola, A. Cazzato, V. Moramarco, and C. Pappalettere, *Orthotropic mechanical properties of fused deposition modelling parts described by classical laminate theory*, *Materials & Design* **90**, 453 (2016).
  - [83] F. Górski, W. Kuczko, R. Wichniarek, and A. Hamrol, *Computation of Mechanical Properties of Parts Manufactured by Fused Deposition Modeling Using Finite Element Method*, (Springer, Cham, 2015) pp. 403–413.
  - [84] A. R. Melro, P. P. Camanho, and S. T. Pinho, *Influence of geometrical parameters on the elastic response of unidirectional composite materials*, *Composite Structures* **94**, 3223 (2012).
  - [85] S. Sheth and R. M. Taylor, *Numerical Investigation of Stiffness Properties of FDM Parts as a Function of Raster Orientation*, , 1112 (2017).
  - [86] X. Liu and V. Shapiro, *Homogenization of material properties in additively manufactured structures*, *Computer-Aided Design* **78**, 71 (2016).
  - [87] S. A. Tronvoll, T. Welo, and C. W. Elverum, *The effects of voids on structural properties of fused deposition modelled parts: a probabilistic approach*, [10.1007/s00170-018-2148-x](https://doi.org/10.1007/s00170-018-2148-x).
  - [88] K. B. V. De, *NEN-EN-ISO 527-4*, (2013).
  - [89] ASTM, *Standard Test Method for Tensile Properties of Polymer Matrix Composite Materials*, *ASTM D 3039*, Tech. Rep. (2008).
  - [90] H. Fahrenholz, *The 2012 version of ISO 527 Plastics : Determination of tensile properties* Zwick/Roell, (2018).
  - [91] A. Melro and P.P. Camanho, *Micromechanical analysis of polymer composites reinforced by unidirectional fibres: Part II-Micromechanical analyses*, *International Journal of Solids and Structures* **50**, 1906 (2013).

- [92] A. Harish, *Implicit vs Explicit FEM: What is the Difference? | Finite Element Method*, (2019).
- [93] Simulia, *Writing a UMAT or VUMAT in Abaqus*, .
- [94] H. Wang, Y. Zhang, Z. Huang, H. Gao, Y. Zhang, X. Gao, and H. Zhou, *Experimental and modeling study of the compressive behavior of PC/ABS at low, moderate and high strain rates*, *Polymer Testing* **56**, 115 (2016).